TECHNISCHE UNIVERSITÄT MÜNCHEN

Lehrstuhl für Aerodynamik und Strömungsmechanik

Numerical Simulation of Fuel Injection and Turbulent Mixing Under High-Pressure Conditions

Jan Matheis

Vollständiger Abdruck der von der Fakultät für Maschinenwesen der Technischen Universität München zur Erlangung des akademischen Grades eines

Doktor-Ingenieurs

genehmigten Dissertation.

Vorsitzender:		Prof. Dr.-Ing. Oskar J. Haidn
Prüfer der Dissertation:	1.	Prof. Dr.-Ing. Nikolaus A. Adams
	2.	Prof. Dr.-Ing. Stefan Hickel

Die Dissertation wurde am 26.06.2017 bei der Technischen Universität München eingereicht und durch die Fakultät für Maschinenwesen am 21.12.2017 angenommen.

Jan Matheis
Schyrenstraße 11
81543 München
Germany

jan.matheis@gmail.com

Released 04.08.2018
Typesetting LaTeX

Abstract

This thesis presents a numerical framework for the Eulerian Large-Eddy Simulation (LES) of liquid-fuel injection and turbulent mixing under high-pressure conditions. Typical application examples are liquid rocket engines, modern diesel engines and gas turbines. The operating pressure and temperature in these devices is often well above the critical pressure and temperature of the pure injectants. Prior to injection, however, the propellants/fuels are in a compressed liquid state at low subcritical temperatures. A physical meaningful representation of such operating conditions demands for complex thermodynamic models, and a robust numerical framework, which is developed in this work. The presented thermodynamic model is based on a cubic equation of state, thermodynamic stability analysis, and vapor-liquid equilibrium (VLE) calculations. It can represent the coexistence of supercritical states and multi-component subcritical two-phase states by means of a homogeneous mixture approach. Primary atomization is represented in an Eulerian framework. Well-resolved LES results are presented for two test cases. First, the shear coaxial injection of liquid nitrogen and gaseous hydrogen at supercritical pressures (with respect to the pure components) is studied. Emphasis is placed on both a quantitative and qualitative comparison between experimental and numerical data, and the assessment of uncertainties related to both of them. It is found that the nitrogen inflow temperature has a first-order influence on computational results, and that thermodynamic unstable states can locally exist within the turbulent mixing layer. Because state-of-the-art for LES of high-pressure flows is the use of thermodynamic closures that assume fuel- and mixture-supercriticality in the entire flow field, a comparison between the two-phase and assumed single-phase closure is presented. As second application example, the injection of a liquid hydrocarbon into a high-pressure, high-temperature atmosphere is studied. The test case is known as Spray A of the Engine Combustion Network (ECN) and the operating conditions resemble that of a modern diesel engine. Numerical results for the baseline case Spray A and three additional operating points demonstrate the excellent predictive performance of two-phase VLE-based approach. Well-known numerical challenges of trans- and supercritical fluid mixing are addressed by comparing a fully conservative formulation to a quasi-conservative formulation of the governing equations. Results prove physical and numerical consistency of both methods on fine grids, and demonstrate the effects of energy conservation errors associated with the quasi-conservative formulation on typical LES grids.

Zusammenfassung

In dieser Arbeit werden Methoden zur Grobstruktursimulation (Large-eddy simulation, LES) von Einspritzvorgängen in Umgebungen bei hohem Druck und hoher Temperatur entwickelt. Typische Anwendungsbereiche sind Flüssigtreibstoffraketen, moderne Dieselmotoren und Gasturbinen. Brennkammerdrücke und -temperaturen in diesen Anwendungen überschreiten hier oftmals deutlich die kritischen Bedingungen der verwendeten Kraftstoffe. Vor der Eindüsung in die Brennkammer hingegen liegt der Kraftstoff als komprimierte Flüssigkeit bei niedrigen, unterkritischen Temperaturen vor. Um die bei diesen Bedingungen auftretenden thermodynamischen Zustände möglichst realitätsnah beschreiben zu können bedarf es komplexer thermodynamischer Modelle, deren Entwicklung im Kontext der numerischen Strömungssimulation Gegenstand dieser Arbeit ist. Das hier beschriebene Modell basiert auf kubischen Zustandsgleichungen, thermodynamischer Stabilitätsanalyse und Dampf-Flüssigkeit-Gleichgewichtsberechnungen (vapor-liquid equilibrium, VLE). Es erlaubt die Abbildung thermodynamisch überkritischer wie auch unterkritischer Zustände. Dampf- und Flüssigphasen in Mehrkomponenten Systemen werden über den homogenen Mischungsansatz berechnet. Darüber hinaus wird der Strahlzerfall in der Eulerschen Betrachtungsweise beschrieben. Numerische Untersuchungen werden für zwei verschiedene Testfälle vorgestellt. Im ersten Testfall, relevant im Kontext von Flüssigtreibstoffraketen, wird die koaxiale Einspritzung von flüssigem Stickstoff und gasförmigem Wasserstoff bei überkritischen Drücken (im Bezug auf den kritischen Punkt der Reinstoffe) betrachtet. Numerische Ergebnisse werden anhand experimenteller Messdaten bewertet. Der Fokus liegt auf der Diskussion von Einflussgrößen und Unsicherheiten sowohl in der Simulation wie auch im Experiment. So zeigt sich beispielsweise, dass die Stickstofftemperatur einen erheblichen Einfluss auf den thermodynamischen Zustand der Mischungsschicht hat - was Fragen im Bezug auf die thermodynamische Modellierung in der LES aber auch auf die Vergleichbarkeit zum Experiment aufwirft. Als weiterer Testfall, relevant für Verbrennungsmotoren, werden numerische Ergebnisse für das sogenannte Spray A des Engine Combustion Network (ECN) diskutiert. Eine sehr gute Übereinstimmung zwischen LES und experimentellen Daten kann hier erzielt werden. Des Weiteren zeigt sich, dass die Berücksichtigung von Dampf- und Flüssigphasen zwingend erforderlich ist, um die physikalischen Prozesse, welche bei der Einspritzung von Kohlenwasserstoffen in Hochtemperatur- und Hochdruck-Umgebungen auftreten, korrekt abzubilden.

Danksagung

Die vorliegende Dissertation entstand während meiner Zeit als wissenschaftlicher Mitarbeiter am Lehrstuhl für Aerodynamik und Strömungsmechanik der Technischen Universität München. An dieser Stelle möchte ich mich bei all den Menschen bedanken, ohne die diese Arbeit so nicht möglich gewesen wäre.

Zuerst möchte ich mich bei Prof. Nikolaus A. Adams bedanken. Ganz herzlichen Dank, dass Sie mir die Möglichkeit der Promotion an Ihrem Institut gegeben haben. Sie haben mir jede nur erdenkliche Freiheit gelassen und mich vor allem bei jedem meiner Vorhaben unterstützt, nicht zuletzt bei dem Abschluss dieser Promotion. Ganz herzlichen Dank dafür!

Stefan, dir gebührt ein besonders großes Dankeschön. Du hast mich über die Jahre sowohl fachlich als auch persönlich immer sehr gefördert. Das ist nicht selbstverständlich und dafür bin ich dir sehr dankbar. Ohne deine Impulse wäre es wohl auch nicht zu dem gemeinsamen Aufenthalt am CTR oder der ein oder anderen Konferenz gekommen. Und wenn ich so zurückblicke, dann waren es genau diese Ereignisse, die letztlich die großen inhaltlichen Fortschritte hervorgebracht haben. Deshalb vielen Dank für die intensive Zusammenarbeit und nicht zuletzt dein Vertrauen in mich.

Vito und Bernd, auch bei euch beiden möchte ich mich bedanken. Schon während unserer Diplomarbeit waren wir ein tolles Team - und ich hätte mir keine besseren Weggefährten für die Höhen und Tiefen der Promotion vorstellen können. Ob es Skipte waren oder einfach nur eine intensive Beratung welche Linienfarbe oder Colormap wohl die schönste ist - ohne euren Input wäre diese Arbeit so nicht möglich gewesen. Ich bin wirklich glücklich, euch als sehr gute Freunde zu wissen.

Auch will ich mich bei allen Freunden und Kollegen am Lehrstuhl für die schöne Zeit bedanken. Allen voran Felix, Felix, Padde, Marcus, Volker, Theresa und Bruno: Dank euch bin ich immer gerne an die Uni rausgefahren und dank euch wird mir die Zeit am Lehrstuhl auch positiv in Erinnerung bleiben.

Hagen, ich hätte es mit dir als Kooperationspartner nicht besser treffen können. Vielen Dank für all deine riesige Unterstützung und all die Diskussionen über die Jahre hinweg. Wer hätte gedacht, dass dieses eine Treffen auf der Dachterasse der TU München der Auftakt zu einem Projekt ist, dass uns letztlich unsere gesamte PhD Zeit - und darüber hinaus - begleitet. Ganz herzlich möchte ich mich auch bei

Prof. Pfitzner bedanken. Sie waren immer sehr engagiert und gerade im Hinblick auf die Thermodynamik eine große Unterstützung. Mir hat die Zusammenarbeit mit Ihnen große Freude bereitet.

Der weitaus wichtigste Dank gebührt meiner Familie, ohne deren Unterstützung ich niemals so weit gekommen wäre: Mama und Papa, ich weiß, dass ihr euch immer viele Sorgen gemacht habt über den Ausgang dieses Projekts. Jetzt könnt ihr endlich durchatmen. Ich danke euch von ganzem Herzen für eure uneingeschränkte Unterstützung, für all das Nachfragen und Verstehen-Wollen meines PhD Themas, für das gute Zureden und Mut Machen. Ihr seid toll!

Zuletzt möchte ich mich bei der Person bedanken, die wirklich am meisten hat ertragen müssen. Vielen Dank Kathi für die unzähligen Stunden in denen du mit mir gegrübelt, abgeleitet und gerechnet hast. Vielen Dank für all die unterstützenden Worte und deine Nachsicht in den Momenten in denen die Uni einen zu großen Platz eingenommen hat.

List of Publications

During this PhD project, several journal publications and conference contributions have been published. This work is partly based on these contributions and text sections have been reproduced in this thesis under the permission of the corresponding publisher.

Peer–Reviewed Journal Papers

1. **J. Matheis** and S. Hickel (2018) Multi-component vapor-liquid equilibrium model for LES of high-pressure fuel injection and application to ECN Spray A. *International Journal of Multiphase Flow*, **99**, 294–311.

2. **J. Matheis**, H. Müller, S. Hickel and M. Pfitzner. Large-eddy simulation of cryogenic jet injection at supercritical pressures. In J. Bellan (Eds.) *High Pressure Flows for Propulsion Applications*, Progress in Astronautics and Aeronautics, AIAA. **(under review)**

3. **J. Matheis**, H. Müller, C. Lenz, M. Pfitzner and S. Hickel (2016) Volume translation methods for real-gas computational fluid dynamics simulations. *Journal of Supercritical Fluids*, **107**, 422–432.

4. H. Müller, C. A. Niedermeier, **J. Matheis**, M. Pfitzner and S. Hickel (2016) Large-eddy simulation of nitrogen injection at trans- and supercritical conditions. *Physics of Fluids*, **28**, 015102.

5. H. Müller, M. Pfitzner, **J. Matheis** and S. Hickel (2015) Large-eddy simulation of coaxial LN2/GH2 injection at trans- and supercritical conditions. *Journal of Propulsion and Power*, **32**(1), 46–56.

6. **J. Matheis** and S. Hickel (2015) On the transition between regular and irregular shock patterns of shock-wave/boundary-layer interactions. *Journal of Fluid Mechanics*, **776**, 200–234. (The content of this publication is not covered in this thesis.)

Conference Proceedings

1. C. Traxinger, H. Müller, M. Pfitzner, S. Baab, G. Lamanna, B. Weigand, **J. Matheis**, C. Stemmer, N. A. Adams and S. Hickel (2017) Experimental and numerical investigation of phase separation due to multi-component mixing at high-pressure conditions. In *28th Conference on Liquid Atomization and Spray Systems (ILASS–Europe 2017)*, Valencia, Spain.
2. S. Hickel and **J. Matheis** (2017) Mixing and phase separation at supercritical and transcritical pressures. In *Ninth International Symposium on Turbulence and Shear Flow Phenomena (TSFP-9)*, Chicago, USA.
3. **J. Matheis** and S. Hickel (2016) Multi-component vapor-liquid equilibrium model for LES and application to ECN Spray A. In *Proceedings of the CTR Summer Program*, Stanford University, USA.
4. **J. Matheis**, H. Müller, M. Pfitzner and S. Hickel (2015) Large-eddy simulation of cryogenic coaxial LN2/GH2 injection under supercritical pressures. In *Ninth International Symposium on Turbulence and Shear Flow Phenomena (TSFP-9)*, Melbourne, Australia.
5. **J. Matheis**, B. Budich and S. Hickel (2013) Large Eddy Simulation of the Transition Process from Regular to Irregular Shock-Wave/Boundary-Layer Interaction. In *Eighth International Symposium on Turbulence and Shear Flow Phenomena (TSFP-8)*, Poitiers, France.

Peer–Reviewed Technical Reports

1. **J. Matheis**, H. Müller, S. Hickel and M. Pfitzner (2016) Large-eddy simulation of cryogenic jet injection at supercritical pressures. In *Annual Report 2016 of the Sonderforschungsbereich/Transregio 40*.
2. **J. Matheis**, H. Müller, M. Pfitzner and S. Hickel (2014) Modeling of real fluid effects. In *Annual Report 2014 of the Sonderforschungsbereich/Transregio 40*.

List of Figures

List of Tables

Table of Contents

Chapter 1

Introduction

This thesis summarizes my work of the past five years at the Chair of Aerodynamics and Fluid Mechanics of the Technical University of Munich. The project I was working on was – and still is – part of the collaborative research center *SFB TRR40*[1] with its aim being the *'development of future space-transportation-system components under high thermal and mechanical loads'*. A typical application example is the European space launcher Ariane 5 and successor Ariane 6. The specific topic of the sub-project was the *'modeling of injection and mixing processes under real-gas conditions'* in the context of computational fluid dynamics (CFD) simulations. Therefore, the main application example during the initial phase of the project was the combustion chamber of a liquid rocket engine (LRE) such as the Vulcain 2 engine. Here, the properties of the propellants during injection significantly deviate from those of an ideal gas due to the high operating pressure and (partially) cryogenic injection temperatures. Furthermore, mixing under high pressure conditions may not follow the classical pattern of two-phase sprays and a dense fluid mixing with diminishing surface tension forces may be

[1] `http://www.sfbtr40.de/`

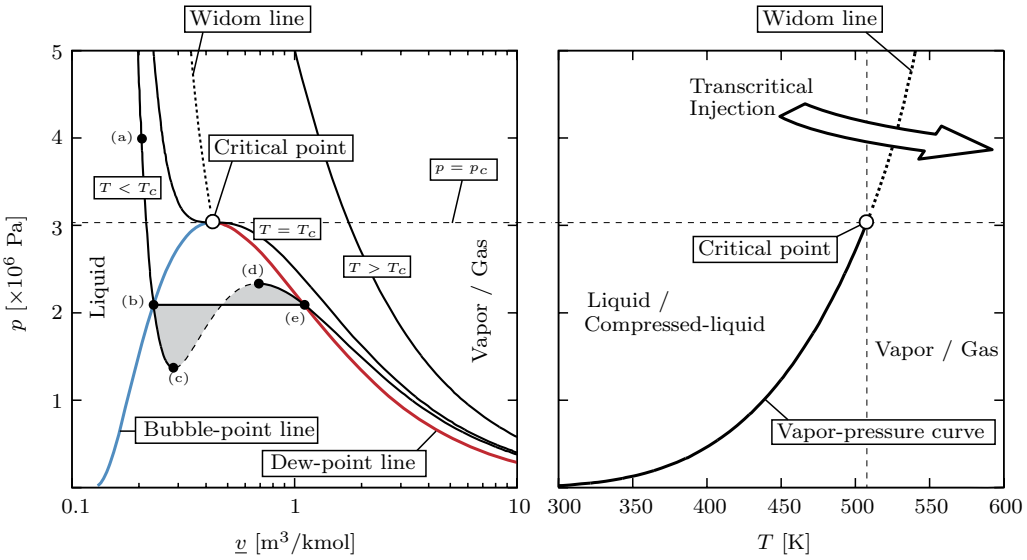

Figure 1.1: Pressure-volume diagram (left) and pressure-temperature diagram (right) for pure n-hexane calculated with the Peng-Robinson EOS.

observed. Such operating conditions demand for more complex equation of state (EOS) models and a robust numerical framework which is developed in this work. More recently, it has been suggested that the aforementioned flow phenomena that are known from LREs may also be found in modern diesel engines given the very high injection pressures and temperatures. Therefore, the second application example in this thesis is a high-pressure liquid-fuel injection test case relevant for internal combustion engines.

1.1 Introductory Thermodynamics

Single-Component Systems

Let us first be clear about the terminology used in this work. In Fig. 1.1 (left) we show a pressure-volume diagram for pure n-hexane (C_6H_{14}) with a supercritical ($T > T_c$), critical ($T = T_c$), and subcritcal ($T < T_c$) isotherm. T_c denotes the critical temperature and p_c denotes the critical pressure. In thermodynamic textbooks, a fluid at point (a) with $T < T_c$ is typically referred to as *compressed liquid* (Firoozabadi, 1999). Here, the pressure is above the saturation pressure and it may also be above the critical pressure p_c. All examples of high-pressure fuel

injection presented in this work will correspond to such a situation, in which the pure injectant is initially in a compressed liquid state at supercritical pressure. In the case of an isothermal expansion process starting from point (a), the pressure decreases towards the bubble-point line. At point (b) the fluid is in a saturated state. A further increase in volume will lead to one of two paths: in thermodynamic equilibrium the change in state, namely the evaporation, follows the solid line (b) - (e) and the pressure of the system remains constant until all liquid has become vapor at the dew-point line. Alternatively, the fluid might follow the path (b) - (c) where it is in a metastable state (known as superheated liquid). Thermodynamic states between (c) and (d) have no physical meaning (here pressure increases with volume because $\partial p/\partial v|_T > 0$). Metastable states become important for flash-boiling or cavitation processes, where a compressed liquid is subject to a strong rarefaction/expansion wave, see, e.g., Saurel et al. (2008). In this thesis, the final pressure of the expanded state (i.e. the pressure at the nozzle exit) will be above the critical pressure p_c of the pure injectant. Therefore, no metastable states nor two-phase phenomena in the **pure substance** will occur.

Figure 1.1 (right) shows the corresponding pressure-temperature diagram for pure n-hexane. In a pT-diagram bubble-point and dew-point line collapse because both pressure and temperature remain constant during phase transition. The resulting curve is called vapor-pressure curve or saturation-curve. Two phases can only coexist in equilibrium along the vapor-pressure curve. The critical point marks its upper end where liquid and vapor phase become indistinguishable. Furthermore, surface tension forces and the heat of evaporation decrease to zero. Beyond the critical point only a single fluid phase is typically defined and its fluid properties are subject to strong changes in the area above the critical point. For example, the heat capacity at constant pressure has a distinctive maximum along supercritical isobars and temperatures $T > T_c$ defining a line emanating from the critical point. This line is named *Widom line* and more recently Gorelli et al. (2006) and Simeoni et al. (2010) demonstrated experimentally (see the aforementioned Refs. for details) that it divides the supercritical region into two regions with *liquid-like* and *gas-like* properties. The temperature along the Widom line is commonly referred to as pseudo-boiling temperature T_{pb} (Oschwald et al., 2006; Chehroudi, 2012). Now to be more specific on the definitions: A fluid on the left-hand side of the Widom line and vapor-pressure curve will be termed compressed liquid. A fluid on the right-hand side of the two curves will be termed vapor or gas. The injection of a propellant that is initially in a compressed liquid state under supercritical pressures into an environment on the right-hand side of the Widom line is typically referred to as *transcritical injection*. For pure fluids, the trajectory in the thermodynamic space does not cross the vapor-pressure curve. This type of jet

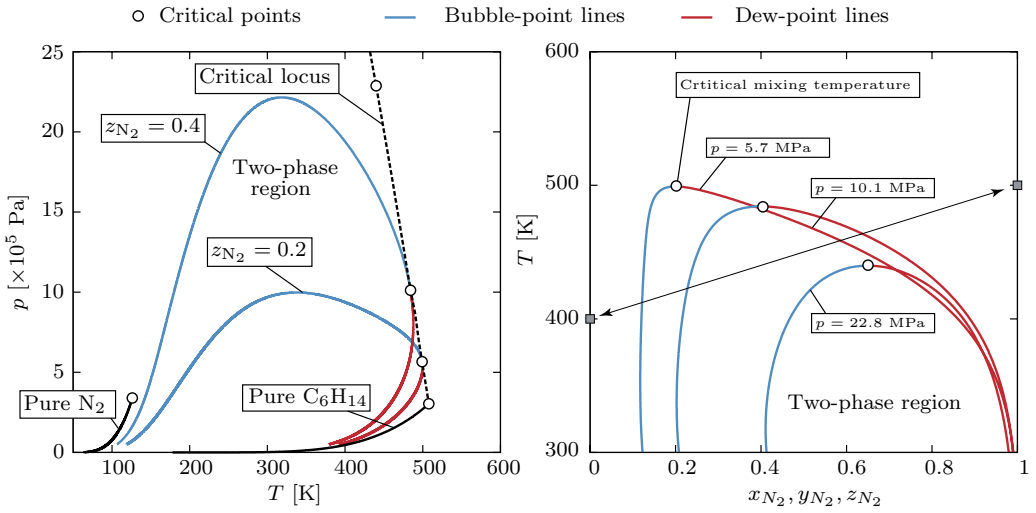

Figure 1.2: Pressure-temperature diagram (left) and temperature-composition diagram (right) for a binary nitrogen-hexane mixture calculated with the Peng-Robinson EOS (personal communication with the Bundeswehr University Munich, Christoph Traxinger).

disintegration is often described as dense fluid mixing with diminishing surface tension. A corresponding literature review will be given in Sec. 1.2.

Multi-Component Systems

The single-component case, however, is typically not found in practical applications. In internal combustion engines and gas turbines, complex multi-component hydrocarbons are injected into compressed air. In LREs mixtures of hydrogen and oxygen (e.g., Vulcain engine of Ariane 5 or Space Shuttle Main Engine) or RP-1 and oxygen (e.g., Sojus with RD-107/108 engine or Falcon 9 with Merlin engine) must be considered. A more representative (but often still simplified) system is the binary system. Figure 1.2 (left) shows the temperature-pressure diagram for a binary nitrogen-hexane mixture calculated with the Peng-Robinson (PR) EOS (Peng and Robinson, 1976). Details on the computation of phase envelopes can be found in Chapter 2 and thermodynamic textbooks, see, e.g., Michelsen and Mollerup (2007) and Firoozabadi (1999). The two black solid lines correspond to the vapor-pressure curves of pure n-hexane and nitrogen N_2. The phase envelope for a mixture (shown for a molar composition of $z_{N_2} = 0.2$ and $z_{N_2} = 0.4$) of the two components looks quite different. Dew- and bubble-point line do not col-

lapse in the pT-diagram but enclose a two-phase region. Both curves meet at the mixtures' critical points. In contrast to pure-component systems, a single critical point does not exist in multicomponent systems. Instead, critical loci define the mixtures' thermodynamic state.[2] Note that the critical locus is also referred to as critical mixing temperature, see, e.g., Chehroudi et al. (2002) and Oschwald et al. (2006). It becomes also apparent that the critical pressure of the mixture exceeds many times the critical pressure of the pure components. Figure 1.2 (right) shows a temperature-composition diagram with the more volatile component nitrogen on the x-axis. Dew- and bubble-point lines enclose the two-phase region and are shown for three different pressure levels. Let us assume that liquid n-hexane ($z_{N_2} = 0$) at 400 K is injected into a quiescent nitrogen atmosphere ($z_{N_2} = 1$) at 500 K under quasi-isobaric conditions. Without making any assumptions on the path/trajectory throughout the mixture space we may state that even though all pressures are well above the critical pressure of pure nitrogen ($p_c = 3.3958$ MPa) and pure n-hexane (3.0340 MPa) two-phase phenomena may be present under all pressures that are indicated in Fig. 1.2 (right).

It becomes apparent that local conditions are extremely important and because the mixtures' critical loci are a complex function of temperature, pressure, and composition, the expression subcritical and supercritical is only used with reference to pure substances – unless otherwise made clear.

1.2 Experimental Observations

Single-Component Systems

Research in recent years has lead to an improved understanding of the processes in cryogenic rocket engine combustion chambers. Especially cold flow studies of both pure component and multicomponent systems contributed to a clearer picture without introducing the complexities of combustion (Oschwald et al., 2006). With a single and well defined critical point at which jet disintegration transitions from subcritical to supercritical behavior, the experimental investigation of

[2] Alkane-nitrogen mixtures often exhibit Type III phase behavior according to the work of Konynenburg and Scott (1980). The critical locus line is two-branched. The branch that starts at the critical point of the pure alkane diverges towards infinite pressure. The other critical locus line starts from the critical point of nitrogen and ends at a three-phase coexistence line. For a complete discussion the interested reader is referred to Konynenburg and Scott (1980) and Rowlinson and Swinton (2013)

cryogenic nitrogen injected into a warm nitrogen atmosphere became probably the most popular and fundamental of all cases (Oschwald et al., 2006; Mayer and Branam, 2004). In the early experimental works, shadowgraphy techniques where often used to characterize jet disintegration. Mayer et al. (1996) were among the first who investigated the injection of liquid nitrogen (LN2) into a gaseous nitrogen (GN2) atmosphere under thermodynamic subcritical, near-critical and supercritical pressures. Under subcritical conditions, Mayer et al. (1996) reported only small-amplitude disturbances on the liquid surface as discussed in several studies of low-speed jets, see, e.g., the review article of Lin and Reitz (1998). Approaching the critical pressure, a change in break-up phenomenology towards spray atomization with ligaments and drops was observed. For supercritical chamber pressures, drops were no longer detected and a *'streaky interface and mixing like a gaseous jet'* was reported by the authors. This behavior was attributed to a reduction of surface tension, which vanishes for a pure substance at and beyond the critical point. In the experimental campaigns of Chehroudi et al. (2002) and Tani et al. (2015) a similar change in the interfacial structure was observed between sub- and supercritical conditions. In an attempt to provide more quantitative data, the LN2/GN2 system was also studied by Raman spectroscopy, see, e.g., Decker et al. (1998), Oschwald and Schik (1999), Chehroudi et al. (2000), Branam and Mayer (2003) and Mayer et al. (2003). In these studies, focus was put on supercritical chamber pressures - with expception of the experimental campaign of Chehroudi et al. (2000)[3] - and a smooth transition across the LN2/GN2 interface was measured, thus, confirming the dense fluid mixing behaviour that was recorded previously by shadowgraphy.

Multi-Component Systems

Newman and Brzustowski (1971) were among the first who conducted a systematic study of liquid carbon-dioxide (CO2) injection into pure GN2 and mixtures of GN2 and gaseous CO2 (GCO2) at various compositions, chamber pressures and temperatures. Even though the chamber pressure was supercritical with respect to the critical pressure of the injectant liquid CO2 ($T_c = 304.18$ K, $p_c = 7.38$ MPa), the authors observed under isothermal conditions (injection temperature = chamber gas temperature) a break-up process much the same as under subcritical operating conditions. Only with increasing ambient temperature (surpassing the critical

[3]Sharp phase interfaces as present under subcritical conditions complicate the Raman signal quantification because the laser beam/sheet can scatter strongly in an elastic way. Furthermore, local focusing at interfaces can cause laser-induced optical breakdown (plasma formation), see, e.g., Decker et al. (1998) for more details.

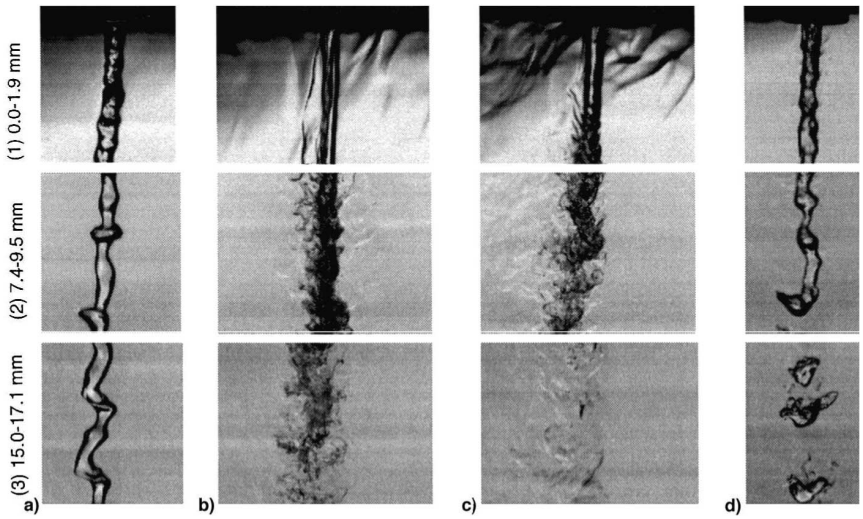

Figure 1.3: Injection of LN2 at 90 K into (a) GN2 at a subcritical pressure of 2.8 MPa (b) GN2 at a near-critical pressure of 3.5 MPa (c) GN2 at supercritical pressure of 6.9 MPa (d) a GN2/GHe mixture (ratio 3.9 by mass) at 6.9 MPa. The gaseous atmosphere was at a temperature of about 250 K. Injection velocity is 1.3 m/s. Reprinted with permission from W. Mayer, A. Schik, B. Vieille, C. Chaveau, I. Gökalp, D. Talley, and R. Woodward, Fig. 9, J. Propul. Power **14**, 835 (1998). Copyright 1998, American Institute of Aeronautics and Astronautics.

temperature of CO2), a finer spray with smaller droplets was reported. This first experimental campaign of Newman and Brzustowski (1971) demonstrated that in the case of multicomponent systems the definition of a point above which jet breakup transitions from subcritical to supercritical behavior is more difficult. Here, the consideration of multicomponent phase-equilibria information as presented in Sec. 1.1 is necessary to interpret experimental findings. Figure 1.3, which was originally published in Woodward and Talley (1996), illustrates this fact very impressively: The first three columns depict the injection of LN2 at about 90 K into a pure GN2 atmosphere under subcritical (2.8 MPa), near-critical (3.5 MPa) and supercritical pressures (6.9 MPa). As described previously, major changes occur in the break-up regime and interface structure from sub- to supercritical pressures. Column (d) depicts a LN2 jet that is injected into a mixture of GN2 and gaseous helium (GHe). The pressure in the chamber is the same as in column (c), i.e., twice the critical pressure of pure nitrogen. A liquid surface can be identified that eventually breaks up into irregularly shaped fluid pockets. It becomes apparent that the mixtures' critical properties must be very different to the critical

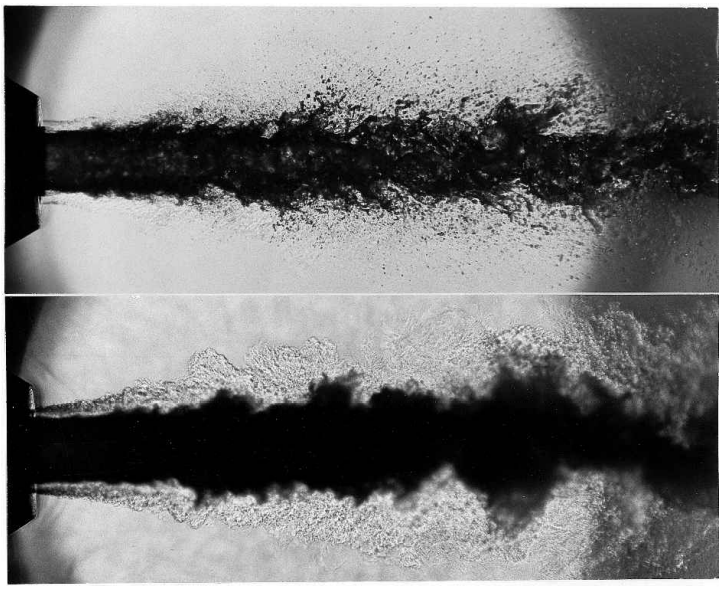

Figure 1.4: LN2 at 97 K with a co-flow of GHe at 280 K is injected into GHe at 300 K under a pressure of 1 MPa (top frame) and 6 MPa (bottom frame). Reprinted with permission from W. Mayer, A. Schik, B. Vieille, C. Chaveau, I. Gökalp, D. Talley, and R. Woodward, Fig. 7, J. Propul. Power **14**, 835 (1998). Copyright 1998, American Institute of Aeronautics and Astronautics.

points of the pure components.

Figure 1.4 shows another famous experimental shadowgraphy image, which is published in Mayer et al. (1998) and many other publications authored by researchers from the *Deutsches Zentrum für Luft- und Raumfahrt* (DLR): LN2 at 97 K with a co-flow of GHe at 280 K is injected into GHe at 300 K (or GN2 at 300 K according to Telaar et al. (2000)). While droplets and ligaments are clearly observable at a chamber pressure of 1 MPa, no droplets are found within the resolution of the shadowgraphs at 6 MPa and *'mixing appears more like that between a dense and a light fluid in a turbulent shear layer'* (Mayer et al., 1998). Later, Mayer and Smith (2004) noted that the critical mixing temperature of the N2/He system is about 125.7 K at this pressure. Since LN2 is injected with about 97 K, mixture states across the shear layer may locally enter a two-phase region. As pointed out by Segal and Polikhov (2008) and Lamanna et al. (2012), the interpretation of shadowgraphy images under high-pressure conditions is not always straightforward: **1.** Because shadowgraphy is integrative along the line of sight, the image represents an average throughout the jet. **2.** Because shadowgraphy measures the

second derivative of density, low density but highly turbulent regions can saturate the image and hide a potential liquid core. **3.** Standard optical techniques may not have sufficient spatial resolution to resolve all details in the fully atomized flow regime. Another interesting aspect was put forward by Bellan (2000), who noted that there is no inconsistency between the observation of drops and ligaments and the fluids (and mixtures) being in a supercritical state due to large density gradients during the initial stage of mixing – which are of course optically identifiable. To provide more quantitative data, Oschwald et al. (1999) performed a series of Raman measurements of the coaxial injection of LN2 with a co-flow of gaseous hydrogen (GH2) into a GN2 atmosphere. The chamber pressure was 4 MPa, thus, supercritical with respect to the critical pressures of the pure components. Similar to the example given in Fig. 1.4, it remains unclear for some operating conditions whether jet disintegration resembled that of a spray or that of diffusive mixing with supercriticality across the entire mixing layer. A more thorough analysis of this setup is presented in Chapter 3.

Due to its spectroscopic properties favorable for Planar Laser Induced Fluorescence (PLIF) and its low critical point, a number of studies focused on the binary component system fluoroketone ($T_c = 441$ K, $p_c = 1.86$ MPa) and nitrogen. Roy et al. (2013) investigated the injection of fluoroketone initially in a supercritical state into a cold nitrogen atmosphere using PLIF. The pressure was always kept above the critical pressure of the injectant fluoroketone, yet, their experiments showed the formation of droplets at the jet interface. Intuitively, this process may be termed condensation. Recently, Muthukumaran and Vaidyanathan (2014, 2015) studied elliptical jets of fluoroketone into its own vapor, GN2 and GHe atmospheres using either Planar Laser Induced Fluorescence (PLIF) or diffused back illumination (DBI). Elliptical jets exhibit an axis switching phenomenon caused by an imbalance between inertial and surface tension forces. This phenomenon can therefore be used to identify surface tension forces – which the authors report for all binary component systems under supercritical conditions (with respect to the pure injectant fluoroketone).

The development of modern internal combustion engines and gas turbines strives for higher efficiency through increasing combustion pressures and temperatures. As a consequence, liquid hydrocarbon fuels are often injected into atmospheres that are supercritical with reference to the critical point of the pure fuel. Especially the operating conditions of diesel engines are expected to promote fuel (and mixture) supercriticality. In this context, the so-called *Spray A* operating condition, which was defined by the *Engine Combustion Network* (ECN, `http://www.sandia.gov/ecn/`), have received considerable attention in the community. Experimental and theoretical findings, see, e.g., Dahms et al. (2013) and Dahms

and Oefelein (2013), questioned the established paradigm of classical spray atomization (primary and secondary breakup, evaporation of droplets) under typical engine conditions: above certain pressures and temperatures a dense fluid mixing with diminishing surface tension was observed in the near-field of n-dodecane sprays after the end of injection (EOI), see, e.g., Manin et al. (2014). With improved optical diagnostics, Crua et al. (2015) and Manin et al. (2015) pushed recently the boundaries above which this transition takes place towards higher pressures and temperatures. Moreover, their measurements showed that the fluid does not reach the dense-fluid mixing state instantaneously and classical evaporation does occur for some time. The aforementioned observations were made after EOI where it was possible to track individual clusters of droplets/dense fluid. Recently, Falgout et al. (2016) focused on the outer periphery of the jet and applied ballistic imaging and ultrafast shadow imaging during the steady-state phase of injection. The authors investigated three pure hydrocarbons and a commercially available diesel fuel. Their results indicated that only the pure fuels tend to undergo changes in the surface morphology with increasing pressure and temperature, while the standard diesel fuel was not affected.

Comprehensive reviews with a special emphasis on cryogenic experiments in the context of LREs including many illustrating experimental images can be found in Mayer and Smith (2004), Oschwald et al. (2006) and Chehroudi (2012). An extensive and very thorough review article is also given by Bellan (2000) with a focus on both experimental results and modeling aspects.

1.3 Numerical Studies

Similar to the previous section, focus is set on non-reacting numerical studies in the context of high-pressure mixing. Pioneering work in this field was done by the group of Josette Bellan. In several studies, see, e.g., Miller et al. (2001), Okong'o and Bellan (2002a, 2003) and Bellan (2006), temporal non-reacting mixing layers were studied by means of Direct Numerical Simulation (DNS). Being aware of the fact that simple binary mixtures have a critical locus (rather than a single critical point), temperature and pressure in their studies were chosen such that only a single phase can exist. The authors demonstrated that supercritical mixing in the presence of high density-gradient regions is a highly anisotropic process. Furthermore, Soret effects (transport of species due to temperature gradients) and Dufour effects (transport of heat due to species gradients) may also become important for modeling of supercritical flows – at least in the context of DNS.

Given the considerable differences that exist between atmospheric-pressure and high-pressure flows, Bellan and co-workers also address the validity of assumptions that are made in the derivation of the large-eddy simulation (LES) equations, see, e.g., Selle et al. (2007) and Taşkinoğlu and Bellan (2010, 2011). For example, due to the nonlinearity of the EOS, additional subgrid-scale (SGS) terms appear in the LES framework.

Several numerical studies have been conducted to understand the physics involved in fuel injection under high-pressure conditions. Early work in the context of LES were conducted by the group of Vigor Yang at the Pennsylvania State University. Given its relevance in rocket engines, some of these early studies focused on mixing and combustion in a shear-coaxial configuration to understand flame anchoring and stabilization, see, e.g., Oefelein and Yang (1998) and Yang (2000). A comprehensive numerical model for general fluid thermodynamics was later developed by Meng and Yang (2003). In their paper, many helpful thermodynamic relations in the context of CFD can be found. The same group was then among the first who employed (two-dimensional) LES to investigate the injection of cryogenic nitrogen under non-reacting supercritical conditions (Zong et al., 2004). Similar to the results of Bellan and co-workers, it was found that density stratification damps velocity fluctuations normal to the jet surface.

Due to the availability of quantitative density measurements (and its single component nature), many groups validated their CFD codes – in a first place – by reproducing part of the measurement series of Mayer et al. (2003) and Branam and Mayer (2003). Following the Eulerian approach for numerical simulations of high-pressure flows, Schmitt et al. (2010) and Selle and Schmitt (2010) included a real-gas thermodynamic framework based on cubic EOS into the LES solver AVBP (`http://www.cerfacs.fr/avbp7x/`). Inspired by the work of Meng and Yang (2003), their framework was later rephrased by Ruiz (2012) in order to calculate thermodynamic partial derivatives as a direct function of transported variables more efficiently. Results for LES of the transcritical LN2 injection case (a.k.a. Mayer's case 3) are in good quantitative agreement with experimental data (Schmitt et al., 2010). Different cubic EOS models and SGS models have been tested for Mayer's case 3 and case 4 by Petit et al. (2013) using their in-house code SiTCom-B (`https://www.coria-cfd.fr/`). More recently, Müller et al. (2016) performed LES of Mayer's experiments using both a pressure-based version of OpenFOAM (`http://www.openfoam.com/`) and the density-based solver solver INCA (`http://www.inca-cfd.com/`). The authors studied different turbulence models, flux limiters, volume-translated cubic EOS, as well as the influence of the inflow boundary condition. It was demonstrated that for this specific test case, details of discretization and SGS modeling have a subordinate effect on the

first order statistical moments compared to the modeling accuracy of the EOS. Other groups who studied Mayer's test cases with their individual LES codes are Terashima and Koshi (2013), Seidl et al. (2017) and most recent Gnanaskandan and Bellan (2017) and Ma et al. (2017).

In the context of LREs, a number of studies that employ frameworks based on real-gas EOS focus on coaxial injectors. Given its technical relevance there is more data available for chemical reacting configurations than it is for inert configurations, see, for instance, Zong and Yang (2007), Schmitt et al. (2011), Masquelet et al. (2012), Hickey and Ihme (2014), Müller and Pfitzner (2015), Wang and Yang (2016), Gaillard et al. (2016b) and Urbano et al. (2016). A noteworthy and comprehensive work in the field of real-gas CFD in application to reacting and non-reacting shear coaxial injectors was conducted by Masquelet (2013) (at that time in the group of Suresh Menon, Georgia Tech). The author comments on many aspects that are crucial for the development of a real-gas framework into an existing compressible LES solver. Furthermore, many thermodynamic derivatives in the context of cubic EOS in CFD applications are provided. Non-reacting coaxial injector configurations using cubic real-gas EOS have been presented by Masquelet et al. (2012), Schmitt et al. (2012), Terashima and Koshi (2014), Matheis et al. (2015) and Müller et al. (2015).

The aforementioned LES studies are mostly related to LREs. Furthermore, Eulerian LES (or DNS) in conjunction with cubic real-gas EOS and standard mixing rules is employed to represent injection and mixing under high-pressure conditions. In case of multi-component systems, temperature and pressure are hence implicitly assumed to support fuel- and mixture supercriticality in the entire flow field. Whether or not this assumption is justified in the context of LREs, or more specifically in the context of cold-flow experiments relevant to LREs, is subject of this work, see Chapter 3. As discussed previously, under diesel engine conditions the established paradigm was or is different. The injection process of a compressed liquid hydrocarbon is expected to follow the pattern of classical spray atomization with primary and secondary breakup and evaporation of droplets. This is the reason why previous numerical simulations in the context of diesel injection – such as the ECN Spray A – have modeled the spray with Lagrangian particle tracking (LPT) methods. A classical two-phase spray is assumed with sharp gas-liquid interfaces evolving according to models for first- and secondary breakup and evaporation. LPT methods have been applied with Reynolds-Average Navier-Stokes (RANS) formulations, e.g., Pei et al. (2015a), or with LES formulations, e.g., Wehrfritz et al. (2013), Xue et al. (2013), Senecal and Pomraning (2014), Pei et al. (2015b) and Jangi et al. (2015). While LPT methods yield impressive results for dilute two-phase flows, i.e., for flows where droplet interactions are rare

and the droplet volume fraction is very small, they can have shortcomings when applied to very dense flow regimes near the nozzle, where the liquid fuel disintegrates into ligaments and further into droplets. Here, semi-empirical Lagrangian primary-breakup models or assumptions on initial droplet size distributions are used, which then render LPT methods sensitive to calibration parameters. Note that quantitative experimental droplet size measurements are usually not available for high-pressure high-temperature sprays. Intuitively, it appears to be easier to represent primary atomization in an Eulerian framework. Very high injection pressures and injection velocities also suggest that compressibility effects should be taken into account. Numerical simulations of Spray A that take advantage of such a fully compressible Eulerian framework for primary atomization have recently been presented by Lacaze et al. (2015) and Hakim et al. (2016), using the PR EOS in an assumed single-phase dense-gas approach. Their results underline the importance of real-gas effects, e.g., speed of sound or specific heat peculiarities, in high-pressure fuel injection systems. The single-phase dense-gas approach, however, does not include the effect of phase separation. This may lead to unphysical or ill-defined states, caused by the cubic EOS and mixing rule framework, if part of the flow is governed by classical two-phase theory. More recently, Knudsen et al. (2016) reproduced nozzle mass and momentum fluxes for Spray A by using also a fully compressible Eulerian PR EOS based approach for the LES of internal nozzle flow and downstream reservoir in a single domain. As noted by the authors, a thermodynamically consistent description of mixture thermodynamics adds significant cost to the overall solver. Therefore, to keep computational costs tractable they rely on the dense-fluid mixing concept but apply a novel and simplified approach for describing the saturation line in a pressure-volume diagram.

Another noteworthy and for this thesis particular relevant study was conducted by Qiu (2014) (at that time in the group of Rolf Reitz, University of Wisconsin). To allow for a physical meaningful simulation of condensation processes that have been reported in the experimental campaign of Roy et al. (2013), Qiu and Reitz (2014) developed a thermodynamic model based on cubic EOS that can represent both sub- and supercritical mixture states in an Eulerian framework. The thermodynamic solver was thoroughly validated, see Qiu et al. (2014a,b), and implemented into the open-source CFD code KIVA-3V. In addition to Roys' experiment, the authors presented RANS simulations of the ECN Spray A case in Qiu and Reitz (2015) for which they concluded that due to fuel vaporization a local cooling occurs such that two-phase fuel/air mixtures are present.

Despite thermodynamic modeling issues, LES of high-pressure fuel injection is also very challenging with respect to numerical stability. The reasons are manifold:
1. Physical properties are strong nonlinear functions of the local pressure and tem-

perature. **2.** Contact interfaces with density ratios in the order of $\mathcal{O}(10) - \mathcal{O}(100)$ can be present between the liquid injectant and gaseous atmosphere. **3.** Depending on the injection velocity, severe hydrodynamic pressure fluctuations and locally supersonic flow may occur. Moreover, it is known that a fully conservative (FC) formulation of the governing equations together with a nonlinear real-gas EOS may lead to spurious pressure oscillations in the flow field, which can deteriorated computational stability, see, e.g., Terashima and Koshi (2012) and Kawai et al. (2015). Abgrall and Karni (2001) describe a similar problem well-known in compressible ideal gas multi-component flows. Several attempts have been made by researchers in order to improve on this issue which arises in the context of FC LES with nonlinear EOS. In order to stabilize their LES, Schmitt et al. (2010) applied the concept of artificial viscosity. They realized that the artificial dissipation must be applied consistently on all transported variables to not generate spurious pressure oscillations. Based on a local sensor, the authors employed a correction to the total energy equation to minimize spurious pressure oscillations (while giving up energy conservation). Terashima and Koshi (2012, 2015) presented a numerical approach for which the total energy conservation equation is replaced by a pressure-evolution equation. This leads to a quasi-conservative (QC) formulation, where energy is not exactly conserved. Most recent, Ma et al. (2017) extended the so-called double-flux method, originally developed for calorically perfect gases by Abgrall and Karni (2001), to general real-gas EOS. Together with an entropy-stable flux, which ensures positivity of the mass fraction, the authors report an improved performance of their method with respect to unphysical pressure oscillations. It is important to note that all aforementioned methods have in common that energy conservation is sacrificed in one way or the other.

1.4 Objectives and Accomplishments

As seen in the previous section, numerical modeling of multi-component flows under both thermodynamic sub- and supercritical conditions is challenging. Not only because thermodynamic aspects must be handled in a consistent way but also turbulence and physical transport properties must be accurately described. In addition, numerical stability and computational efficiency are of great importance to allow for the simulation of relevant flows and realistic geometries. Starting from an existing – and for ideal gases well validated – compressible LES solver, the main objective of this work is to develop a numerical framework suitable for LES of injection processes into high-pressure atmospheres. Physical processes represented by the modeling approach are supercritical mixing as well as phase transition

phenomena such as evaporation or condensation in high-pressure multi-component environments. The solver is validated with the help of reference experiments, which are relevant to liquid rocket engines and internal combustion engines.

The main achievements in the course of this work are:

- Development and implementation of
  - a real-gas framework valid for multi-component single-phase flows based on the generalized cubic EOS (Sec. 2.2).
  - an Eulerian two-phase model based on cubic EOS, thermodynamic stability analysis, vapor-liquid-equilibrium calculations and the homogeneous mixture approach (Sec. 2.3).
  - a framework which allows the use of volume-translation methods for cubic EOS in the context of CFD. This content is not covered here, but can be found in Matheis et al. (2016).
- Implementation of the pressure evolution equation (Terashima and Koshi, 2012) in order to study the effect of energy non-conservative methods in application to a realistic three-dimensional setup.
- Numerical simulation of a single-component test case: the coaxial injection of liquid nitrogen with a co-flow of gaseous nitrogen into a high-pressure nitrogen atmosphere (Tani's case). In this study, focus is set on the evaluation of different EOS models, in particular volume-translation methods. This content is not covered here, but can be found in Matheis et al. (2016).
- Numerical simulation of a binary mixing case: the coaxial injection of liquid nitrogen and gaseous hydrogen into a high-pressure nitrogen atmosphere (Oschwald's case, Chapter 3). In this study, focus is set on local phase separation phenomena and the discussion of uncertainties related to both experiment and simulation.
- Numerical simulation of ECN Spray A (Chapter 4). In this study, the application of the Eulerian two-phase model is mandatory to allow for a physical meaningful representation of the injection process. Focus is set on the quantitative comparison to experimental data.
- Numerical simulation of liquid and gaseous n-hexane into a gaseous nitrogen atmosphere under high-pressure conditions (ITLR case, Appendix A). This test case demonstrates the excellent performance of the Eulerian two-phase model for LES of dense sprays and condensation phenomena.

All methods described in this work are implemented into the in-house code INCA (`http://www.inca-cfd.com/`). All simulations were conducted on the SuperMUC supercomputer at the Leibniz Rechenzentrum München (LRZ).

In parallel to my PhD project, I also continued the work of my diploma thesis where I studied the transition process from regular to Mach reflection in supersonic flow. In this context, Vito Pasquariello and I together with the group of Shashi B. Verma designed an experimental campaign which was conducted at the National Aerospace Laboratories (NAL) in Bangalore, India. The interested reader may find details on the experimental setup in Verma and Chidambaranathan (2015). My work in the field of supersonic aerodynamics is not covered in this thesis but can be found in Matheis and Hickel (2015).

1.5 Outline

This thesis is divided into five chapters. In the first chapter focus was put on an introduction on high-pressure fuel injection systems with an emphasis on fuel supercriticality. Chapter 2 details the governing equations and the numerical model used for LES. The main focus is on the real-gas thermodynamic framework. Practical implementation guidelines will be given and thermodynamic aspects are discussed by taking the example of a binary nitrogen-hydrogen system. A brief introduction to Implicit LES (ILES) is given at the end of Chapter 2 together with the modifications of the numerical method which are necessary to ensure computational stability for LES of real-gas flows. In Chapter 3, LES results for a selected operating point of a series of experiments of Oschwald et al. (1999) are presented. Finally, numerical simulation results for the ECN Spray A case are provided in Chapter 4. The work is concluded in Chapter 5, where the main findings are summarized and an outlook for future work is given. The ITLR case is provided as Appendix A chapter because this project is currently in a work in progress state. A collection of MATLAB scripts that can be used to compute and plot some of the figures presented in this thesis is described in Appendix B.

Chapter 2

Physical and Numerical Model

This chapter summarizes the governing physical equations for the description of a fluid, i.e., the three-dimensional compressible multi-component Navier-Stokes equations, together with the thermodynamic closures. In this work, thermodynamic closures are formulated for single- and two-phase flows by means of a single-fluid approach. Focus is put on a comprehensive description of the thermodynamic models together with detailed implementation strategies. Finally, a brief introduction to the numerical method is given.

> This section has partially been published in Matheis et al. (2016) [Volume translation methods for real-gas computational fluid dynamics simulations. *Journal of Supercritical Fluids*, **107**, 422–432.], Matheis and Hickel (2016) [Multi-component vapor-liquid equilibrium model for LES and application to ECN Spray A. In *Proceedings of the CTR Summer Program*, Stanford University, USA.] and Matheis and Hickel (2018) [Multi-component vapor-liquid equilibrium model for LES of high-pressure fuel injection

> and application to ECN Spray A. *International Journal of Multiphase Flow*, **99**, 294–311].

2.1 Governing Equations

We solve the three-dimensional compressible multi-component Navier-Stokes equations either in a fully conservative (FC) formulation,

$$\partial_t \rho + \boldsymbol{\nabla} \cdot (\rho \mathbf{u}) = 0 \tag{2.1}$$

$$\partial_t \rho Y_i + \boldsymbol{\nabla} \cdot (\rho Y_i \mathbf{u}) = \boldsymbol{\nabla} \cdot \mathbf{J}_i \tag{2.2}$$

$$\partial_t \rho \mathbf{u} + \boldsymbol{\nabla} \cdot (\rho \mathbf{u}\mathbf{u} + \mathbf{I}p) = \boldsymbol{\nabla} \cdot \boldsymbol{\tau} \tag{2.3}$$

$$\partial_t E + \boldsymbol{\nabla} \cdot [(E + p)\mathbf{u}] = \boldsymbol{\nabla} \cdot (\mathbf{u} \cdot \boldsymbol{\tau} - \mathbf{q}) \,, \tag{2.4}$$

or in a quasi-conservative (QC) formulation for which the total energy conservation, Eq. (2.4), is replaced by the pressure-evolution equation

$$\begin{aligned} \partial_t p + \boldsymbol{\nabla} \cdot (p\mathbf{u}) = (p - \rho c^2) \boldsymbol{\nabla} \cdot \mathbf{u} \ldots \\ + \frac{1}{\rho} \cdot \frac{\alpha_p}{c_v \beta_T} \left[\boldsymbol{\nabla} \cdot (\boldsymbol{\tau} \cdot \mathbf{u} - \mathbf{q}) - \mathbf{u} \cdot (\boldsymbol{\nabla} \cdot \boldsymbol{\tau}) \right] \ldots \\ + \sum_{i=1}^{N_c} \frac{1}{\rho} \frac{\partial p}{\partial Y_i}\bigg|_{\rho, e, Y_{j \neq i}} \boldsymbol{\nabla} \cdot \mathbf{J}_i \,. \end{aligned} \tag{2.5}$$

The state vector consists of mass density ρ, partial densities ρY_i of species $i = \{1 \ldots N_c\}$, linear momentum $\rho \mathbf{u}$, and total energy density $E = \rho e + \frac{1}{2}\rho \mathbf{u} \cdot \mathbf{u}$ (FC) or the pressure p (QC). $\mathbf{u} = [u_1, u_2, u_3]^T$ is the velocity vector in a Cartesian frame of reference, c denotes the speed of sound, c_v is the heat capacity at constant volume, and α_p and β_T are the thermal expansion and isothermal compressibility coefficient. To allow for a meaningful comparison between FC and QC simulations, we also included the effect of the diffusion induced pressure variation, the last term on the right-hand side of Eq. (2.5), which was neglected in Terashima and Koshi (2012). The thermodynamic derivative is calculated as

$$\frac{\partial p}{\partial Y_i}\bigg|_{e, \rho, Y_{j \neq i}} = - \frac{\partial p}{\partial e}\bigg|_{\rho} \cdot \frac{\partial e}{\partial Y_i}\bigg|_{p, \rho, Y_{j \neq i}} \tag{2.6}$$

with

$$\left.\frac{\partial e}{\partial Y_i}\right|_{p,\rho,Y_{j\neq i}} = h_i - \frac{c_p}{v\ \alpha_p} v_i, \tag{2.7}$$

cf., Okong'o and Bellan (2002b), where $Y_{j\neq i}$ denotes that all Y_j are held constant except Y_i. The two terms on the right-hand side of Eq. (2.7), h_i and v_i, are known as partial enthalpy and partial volume (on a mass basis) of species i. For a more detailed discussion on Eq. (2.5) it is referred to the original work of Terashima and Koshi (2012, 2015).

According to the Stokes hypothesis for a Newtonian fluid, the viscous stress tensor is

$$\boldsymbol{\tau} = \mu \left(\boldsymbol{\nabla}\mathbf{u} + (\boldsymbol{\nabla}\mathbf{u})^T - 2/3\, \mathbf{I}\ \boldsymbol{\nabla}\cdot\mathbf{u} \right) , \tag{2.8}$$

with μ being the dynamic viscosity and $\mathbf{I}$ the unit tensor. The diffusional fluxes are calculated via Fick's law

$$\mathbf{J}_i = \rho D_i \boldsymbol{\nabla} Y_i - Y_i \sum_{j=1}^{N_c} \rho D_j \boldsymbol{\nabla} Y_j \ , \tag{2.9}$$

where

$$D_i = \frac{(1 - z_i)}{\sum_{j\neq i}^{N_c} \frac{z_j}{D_{ij}}} \tag{2.10}$$

is an effective binary diffusion coefficient for the diffusion of species i into the rest of the mixture, and z_i denotes the overall mole fraction of species i. The physical binary mass diffusion coefficients D_{ij} are modeled according to Chapman and Enskog theory, see, e.g., Prausnitz et al. (1998). The vector

$$\mathbf{q} = -\kappa \boldsymbol{\nabla} T\ - \sum_{i=1}^{N_c} h_i \mathbf{J}_i \tag{2.11}$$

consists of heat conduction and the enthalpy flux by species diffusion, where κ is the thermal conductivity, T is the temperature, and h_i is the partial enthalpy of species i on a mass basis. Viscosity and thermal conductivity are modeled with correlations given by Chung et al. (1988).

Table 2.1: Critical temperature and pressure and acentric factor of nitrogen, hydrogen, n-dodecane and n-hexane.

Species	T_c [K]	p_c [Pa]	ω [-]
N_2	126.192	3.3958×10^6	0.0372
H_2	33.145	1.2964×10^6	−0.2160
$C_{12}H_{26}$	658.000	1.8200×10^6	0.5764
C_6H_{14}	507.820	3.0340×10^6	0.2990

The FC and QC equations are closed by a thermodynamic model that relates pressure, temperature and density.

2.2 Single-Phase Thermodynamics

The equations presented in this section are valid for a single homogeneous fluid phase composed of an arbitrary number of components $N_c \geq 1$.

2.2.1 Cubic Multi-Component Equation of State

Cubic EOS are widely used due to their simplicity and overall good accuracy for pure substances and mixtures. Especially in computational intensive calculations such as real-gas CFD simulations, a trade-off between accuracy and efficiency must be found. Here, cubic EOS allow for a rapid calculation of thermodynamic properties while accounting for the full non-linear pressure-volume-temperature (PVT) behavior of the fluid/mixture. Furthermore, liquid and vapor phase properties can be modeled with a single EOS and so there is no need for dedicated phase-specific EOS. In this thesis, single- and two-phase models are therefore formulated for cubic EOS, which can be expressed in a generalized pressure explicit form as

$$p(\underline{v}, T, \mathbf{z}) = \frac{\mathcal{R}T}{\underline{v} - b} - \frac{a\alpha(T)}{\underline{v}^2 + u\,b\,\underline{v} + w\,b^2}, \tag{2.12}$$

where the pressure p is a function of the molar volume $\underline{v}$, temperature T and if $N_c > 1$ the molar composition $\mathbf{z} = \{z_1 \dots z_{N_c}\}$. Here and in the following, all intensive thermodynamic properties are expressed as molar quantities, denoted by $\underline{\star}$.

$\mathcal{R}$ is the universal gas constant. Introducing the non-dimensional compressibility factor

$$Z = \frac{p\underline{v}}{\mathcal{R}T} \tag{2.13}$$

together with dimensionless forms of the EOS parameters $A = a\alpha p/(\mathcal{R}T)^2$ and $B = bp/(\mathcal{R}T)$, Eq. (2.12) can also be expressed as

$$Z = \frac{1}{1 - B/Z} - \frac{A}{B}\frac{B/Z}{1 + u\,B/Z + w\,(B/Z)^2} \tag{2.14}$$

which can further be rearranged in a cubic polynomial in Z, see Sec. 2.2.2.

In all subsequent simulations, we use the Peng-Robinson (PR) (Peng and Robinson, 1976) EOS for which $u = 2$ and $w = -1$.[1] The function

$$\alpha = \left[1 + c_0(1 - \sqrt{T/T_c})\right]^2 \tag{2.15}$$

accounts for the polarity of a fluid and is a correlation of temperature T, critical temperature T_c and acentric factor ω via

$$c_0 = 0.37464 + 1.54226\omega - 0.2699\omega^2. \tag{2.16}$$

The parameter

$$a = 0.45724\left(\mathcal{R}^2 T_c^2/p_c\right) \tag{2.17}$$

represents attractive forces between molecules and the effective molecular volume is represented by

$$b = 0.0778\left(\mathcal{R}T_c/p_c\right). \tag{2.18}$$

The critical properties and the acentric factor of nitrogen, hydrogen, n-dodecane and n-hexane are given in Tab. 2.1.

We use conventional mixing rules to extend the PR EOS to a mixture composed

[1] The Soave-Redlich-Kwong (SRK) (Soave, 1972) EOS is obtained with $u = 1$ and $w = 0$ and the corresponding definitions for $a\alpha(T)$ and b, see, e.g., Poling et al. (2000).

of N_c components. The parameters required in the EOS are calculated from

$$a\alpha = \sum_{i}^{N_c}\sum_{j}^{N_c} z_i z_j a_{ij}\alpha_{ij} \qquad \text{and} \qquad b = \sum_{i}^{N_c} z_i b_i, \tag{2.19}$$

with z_i being the mole fraction of component i. The coefficients a_{ij} and α_{ij} are calculated with combination rules. There are two common used combination rules for calculating the coefficient $a_{ij}\alpha_{ij}$:

Combination rule 1: A direct adjustment of the cross-parameter

$$a_{ij}\alpha_{ij} = \sqrt{a_i\alpha_i a_j\alpha_j}(1 - k_{ij}) \tag{2.20}$$

where k_{ij} is the binary interaction parameter.

Combination rule 2 (or the pseudo-critical method): Adjustment of pseudo-critical properties. Off-diagonal elements are calculated using the same expression as for the diagonals, i.e., Eq. (2.15)-(2.17) for the PR EOS, and

$$a_{ij}\alpha_{ij} = f(T_{c,ij}, p_{c,ij}, \omega_{ij}) \tag{2.21}$$

with the pseudo-critical parameters

$$T_{c,ij} = \sqrt{T_{c,i}T_{c,j}}(1 - k'_{ij}), \quad p_{c,ij} = Z_{c,ij}(\mathcal{R}T_{c,ij}/v_{c,ij}), \quad v_{c,ij} = \frac{1}{8}\left[v_{c,i}^{1/3} + v_{c,j}^{1/3}\right]^3,$$
$$\omega_{ij} = 0.5\left(\omega_i + \omega_j\right), \quad Z_{c,ij} = 0.5\left(Z_i + Z_j\right). \tag{2.22}$$

Here, k'_{ij} is the binary interaction parameter. Note that k'_{ij} and k_{ij} are numerically not the same. The binary interaction parameter affects the PVT properties of the mixture and the accuracy of vapor-liquid equilibria (VLE). As pointed out by Reid et al. (1987), it is important to realize that mixing- and combining rules are essentially empirical[2]. Only a comparison against experimental data can give confidence that the employed mixture model is appropriate for the calculation of volumetric mixture properties. Typically, the binary interaction parameters in Eq. (2.20) and (2.22) are regressed using available experimental VLE or PVT data. In the present work, the pseudo-critical method is used with $k'_{12} = 0$. As it will be discussed in more detail in Sec. 3.4.2 and Sec. 4.2, a reasonably good agreement is obtained to experimental VLE data at relevant pressures and temperatures. Also note that binary interaction parameters are assumed independent of temperature,

[2]With one exception being the truncated virial equation of state, for which an exact relation is known for mixture coefficients, see Reid et al. (1987) Chapter 4.

pressure and composition.

Departure Function Formalism

In addition to the thermal EOS, expressions for caloric properties that account for their pressure dependence are needed. The departure function formalism provides such expressions and only requires relationships provided by the EOS. The departure function, e.g., for the internal energy, can be written as

$$\underline{e}(T, \underline{v}, \mathbf{z}) = \underline{e}^{\mathrm{ig}}(T, \mathbf{z}) + \int_{\infty}^{\underline{v}} \left[T \left. \frac{\partial p}{\partial T} \right|_{\underline{v}} - p \right] d\underline{v}. \tag{2.23}$$

Using the generalized cubic EOS (Eq. 2.12), the solution of the integral reads

$$\left(\underline{e} - \underline{e}^{\mathrm{ig}}\right) = \left[a\alpha - T \frac{\partial a\alpha}{\partial T} \right] K \tag{2.24}$$

with

$$K = \frac{1}{b\sqrt{u^2 - 4w}} \ln \left[\frac{2\underline{v} + b(u - \sqrt{u^2 - 4w})}{2\underline{v} + b(u + \sqrt{u^2 - 4w})} \right] = \frac{1}{b\sqrt{u^2 - 4w}} \ln \left[\frac{\Lambda^-}{\Lambda^+} \right] \tag{2.25}$$

and the shortcuts $\Lambda^- = 2\underline{v} + b(u - \sqrt{u^2 - 4w})$ and $\Lambda^+ = 2\underline{v} + b(u + \sqrt{u^2 - 4w})$. The ideal reference state denoted as $^{\mathrm{ig}}$ is evaluated using the 9-coefficient NASA polynomials (Goos et al., 2009). There are a number of thermodynamic derivatives needed and the most important ones will be given in the following. Helpful details, derivations and analytical solutions to caloric and derived properties not listed below are available in literature, see, e.g., Firoozabadi (1999), Poling et al. (2000), and Elliott and Lira (2012).

The enthalpy $\underline{h}$ is obtained from

$$\left(\underline{h} - \underline{h}^{\mathrm{ig}}\right) = \left(\underline{e} - \underline{e}^{\mathrm{ig}}\right) + p\underline{v} - \mathcal{R}T. \tag{2.26}$$

The entropy departure function $\underline{s}$ is defined as

$$\underline{s}(T, \underline{v}, \mathbf{z}) = \underline{s}^{\mathrm{ig}}(T, \mathbf{z}) + \int_{\infty}^{\underline{v}} \left[\left. \frac{\partial p}{\partial T} \right|_{\underline{v}} - \frac{\mathcal{R}}{\underline{v}} \right] d\underline{v} + \mathcal{R} \log Z \tag{2.27}$$

and the solution to the integral reads

$$\underline{s}(T, \underline{v}, \mathbf{z}) - \underline{s}^{\mathrm{ig}}(T, \mathbf{z}) = -\frac{\partial a\alpha}{\partial T} K + \mathcal{R} \log\left[1 - \frac{b}{\underline{v}}\right]. \tag{2.28}$$

A general expression for the Gibbs energy $\underline{g}$ can be written by combining the enthalpy and entropy departures, i.e.,

$$\left(\underline{g} - \underline{g}^{\mathrm{ig}}\right) = \left(\underline{h} - \underline{h}^{\mathrm{ig}}\right) - T\left(\underline{s} - \underline{s}^{\mathrm{ig}}\right) \tag{2.29}$$

$$= a\alpha K + p\underline{v} - \mathcal{R}T - \mathcal{R}T \log\left[1 - \frac{b}{\underline{v}}\right]. \tag{2.30}$$

For pure substances, the Gibbs energy is needed to determine the most stable root when three volume (or equivalently compressibility factor) roots are found as solution to Eq. (2.12) for given temperature and pressure, see Sec. 2.2.2. By differentiating Eq. (2.24) with respect to the temperature, we obtain an expression for the heat capacity at constant volume

$$\left(\underline{c}_v - \underline{c}_v^{\mathrm{ig}}\right) = -T\frac{\partial^2 a\alpha}{\partial T^2} K. \tag{2.31}$$

The heat capacity at constant pressure

$$\underline{c}_p = \underline{c}_v - T\left(\left.\frac{\partial p}{\partial T}\right|_{\underline{v}}\right)^2 \Big/ \left.\frac{\partial p}{\partial \underline{v}}\right|_T \tag{2.32}$$

$$\tag{2.33}$$

with

$$\left.\frac{\partial p}{\partial T}\right|_{\underline{v}} = \frac{\mathcal{R}}{\underline{v} - b} - \frac{\partial a\alpha}{\partial T}\frac{1}{\underline{v}^2 + u\,b\,\underline{v} + w\,b^2} \tag{2.34}$$

and

$$\left.\frac{\partial p}{\partial \underline{v}}\right|_T = \frac{(2\underline{v} + u\,b)a\alpha}{(\underline{v}^2 + u\,b\,\underline{v} + w\,b^2)^2} - \frac{\mathcal{R}T}{(\underline{v} - b)^2}. \tag{2.35}$$

The coefficient of thermal expansion α_p (also known as expansivity) and isothermal

compressibility β_T are defined as

$$\alpha_p = \frac{1}{\underline{v}} \left. \frac{\partial \underline{v}}{\partial T} \right|_p = -\frac{1}{\underline{v}} \frac{\partial p / \partial T|_{\underline{v}}}{\partial p / \partial \underline{v}|_T} \tag{2.36}$$

and

$$\beta_T = \frac{1}{\underline{v}} \left. \frac{\partial \underline{v}}{\partial p} \right|_T = -\frac{1}{\underline{v}} \frac{1}{\partial p / \partial \underline{v}|_T}, \tag{2.37}$$

respectively. The isentropic or thermodynamic speed of sound c is defined as

$$c = \sqrt{\left. \frac{\partial p}{\partial \rho} \right|_s} \tag{2.38}$$

which can be recast into

$$c = \sqrt{\frac{\underline{c}_p}{\underline{c}_v} \left. \frac{\partial p}{\partial \underline{v}} \right|_T \frac{\underline{v}^2}{M}} \tag{2.39}$$

with M being the molar mass of the pure substance or mixture.

Partial Molar Properties

In order to calculate the interdiffusional enthalpy flux in Eq. (2.11), the partial enthalpy on a mass basis h_i is required. In the following, a brief introduction in the concept of partial properties is given. Let F be any extensive property (e.g. volume V, enthalpy H or Gibbs free energy G) of a homogeneous phase. F can be expressed as a function of the two independent intensive properties temperature and pressure and the size of the system $\mathbf{n} = \{n_1, \ldots, n_{N_c}\}$ where n_i denotes the number of moles of each component:

$$F = F(T, p, \mathbf{n}). \tag{2.40}$$

The molar specific property $\underline{f}$ is defined by

$$\underline{f}(T, p, \mathbf{z}) = \frac{F}{n} \tag{2.41}$$

and because $\underline{f}$ is an intensive property it is a function of only the intensive properties temperature T, pressure p and mole fractions $\mathbf{z} = \{z_1, \ldots, z_{N_c}\}$. Per definition,

the derivative

$$\underline{f}_i(T,p,\mathbf{z}) = \left.\frac{\partial F(T,p,\mathbf{n})}{\partial n_i}\right|_{T,p,n_{j\neq i}} = \left.\frac{\partial n\underline{f}(T,p,\mathbf{z})}{n_i}\right|_{T,p,n_{j\neq i}} \tag{2.42}$$

at constant temperature, pressure and mole number $n_{j\neq i}$ is called the partial molar property of F. A partial property tells us how an extensive property of the mixture changes with an infinitesimal change in the number of moles of species i at constant temperature, pressure and mole number $n_{j\neq i}$ (Elliott and Lira, 2012). Partial properties are intensive properties. They are a function of temperature, pressure and composition, and the relation between a partial mass property f_i and a partial molar property $\underline{f}_i$ is the molecular weight M_i of the component i

$$\underline{f}_i = M_i f_i. \tag{2.43}$$

It can further be shown that

$$F(T,p,\mathbf{n}) = \sum_{i=1}^{N_c} n_i \left.\frac{\partial F(T,p,\mathbf{n})}{\partial n_i}\right|_{T,p,n_{j\neq i}} = \sum_{i=1}^{N_c} n_i \underline{f}_i(T,p,\mathbf{z}) \tag{2.44}$$

and

$$\underline{f}(T,p,\mathbf{z}) = \sum_{i=1}^{N_c} z_i \left.\frac{\partial n\underline{f}(T,p,\mathbf{z})}{\partial n_i}\right|_{T,p,n_{j\neq i}} = \sum_{i=1}^{N_c} z_i \underline{f}_i(T,p,\mathbf{z}). \tag{2.45}$$

Using the generalized cubic EOS the partial molar volume $\underline{v}_i$ and enthalpy $\underline{h}_i$ yield

$$\underline{v}_i = \left.\frac{\partial V}{\partial n_i}\right|_{T,p,n_{j\neq i}} = -\left.\frac{\partial \underline{v}}{\partial p}\right|_T \left[\frac{\mathcal{R}T}{(v-b)} + \frac{b_i\mathcal{R}T}{(v-b)^2}\cdots \right.$$
$$\left. -\frac{2\sum_{k=1}^{N_c} z_k a_{ik}\alpha_{ik}}{\underline{v}^2 + ub\underline{v} + wb^2} + \frac{a\alpha(uv+2wb)b_i}{(\underline{v}^2 + ub\underline{v} + wb^2)^2}\right] \tag{2.46}$$

and

$$\underline{h}_i = \left.\frac{\partial H}{\partial n_i}\right|_{T,p,n_{j\neq i}} = \underline{h}_i^{\mathrm{ig}} + p\underline{v}_i - \mathcal{R}T + \left(a\alpha - T\frac{\partial a\alpha}{\partial T}\right)\left(\frac{\underline{v}_i - \underline{v}b_i/b}{\underline{v}^2 + ub\underline{v} + wb^2}\right)\ldots + K\left[2\sum_{k=1}^{N_c} z_k a_{ik}\alpha_{ik} - 2T\sum_{k=1}^{N_c} z_k \frac{\partial a_{ik}\alpha_{ik}}{\partial T} - \left(a\alpha - T\frac{\partial a\alpha}{\partial T}\right)\frac{b_i}{b}\right], \tag{2.47}$$

respectively.

The partial molar Gibbs energy, commonly referred to as *chemical potential* $\underline{\mu}_i$, is calculated as

$$\underline{\mu}_i = \left.\frac{\partial G}{\partial n_i}\right|_{T,p,n_{j\neq i}} = \underline{\mu}_i^{\mathrm{ig}} + \frac{b_i}{b}(p\underline{v} - \mathcal{R}T) - \mathcal{R}T\log\left[Z\left(1 - \frac{b}{\underline{v}}\right)\right] + \ldots a\alpha K\left(\frac{2\sum_{k=1}^{N_c} z_k a_{ik}\alpha_{ik}}{a\alpha} - \frac{b_i}{b}\right). \tag{2.48}$$

As it will be discussed in Sec. 2.3.1, the chemical potential is needed in phase equilibria calculations.

Note that the EOS parameters u and w and the binary interaction parameter k'_{ij} are assumed to be no function of the composition. Very helpful details on the calculation of partial molar properties can be found in Masquelet (2013) and Elliott and Lira (2012). For a more detailed theoretical background it is referred to Michelsen and Mollerup (2007) or Shavit and Gutfinger (2008).

2.2.2 Primitive to Conservative Variables

There are a number of situations in which it is necessary to calculate the volume and caloric properties, such as internal energy for a given temperature T, pressure p and composition on a mass basis $\mathbf{Y} = \{Y_1, \ldots Y_{N_c}\}$. For example, during initialization, the density ρ and internal energy e (as part of the total energy E) as they appear in the governing equations need to be calculated from $(T, p, \mathbf{Y})$. It may also be more convenient to specify boundary conditions, such as isothermal walls or inflow boundary, via a prescription of $(p, T, \mathbf{Y})$. Solving the cubic EOS also plays an important role for the calculation of vapor-liquid equilibria at given

$(T, p, \mathbf{z})$, see Sec. 2.3.3. In the following, details are given on the root-finding algorithm that was used in all single- and two-phase simulations. The calculation of imaginary roots is omitted since we are dealing with physical quantities. Parts of the algorithm, which is detailed in the following, can be found in Press et al. (2002) and Elliott and Lira (2012).

Equation (2.14) can be rearranged to a cubic polynomial in Z

$$Z^3 + a_2\, Z^2 + a_1\, Z + a_0 = 0 \tag{2.49}$$

with the coefficients

$$a_2 = B(u-1) - 1, \tag{2.50}$$

$$a_1 = A + wB^2 - uB(B+1) \tag{2.51}$$

$$a_0 = -B(wB^2 + wB + A). \tag{2.52}$$

First, we compute

$$Q = \frac{a_2^2 - 3a_1}{9} \quad \text{and} \quad R = \frac{2a_2^3 - 9a_2a_1 + 27a_0}{54}. \tag{2.53}$$

If $R^2 < Q^3$, then the EOS has three real roots $\mathbf{Z} = \{Z_1, Z_2, Z_3\}$:

$$\mathbf{Z} = \left\{ -2\sqrt{Q}\cos\left(\frac{\phi}{3}\right), -2\sqrt{Q}\cos\left(\frac{\phi + 2\pi}{3}\right), -2\sqrt{Q}\cos\left(\frac{\phi - 2\pi}{3}\right) \right\} - \frac{a_2}{3} \tag{2.54}$$

with

$$\phi = \arccos\left(R/\sqrt{Q^3}\right). \tag{2.55}$$

If $R^2 \geq Q^3$, then the cubic EOS has only a single real root

$$Z = C_1 + C_2 - \frac{a_2}{3} \tag{2.56}$$

with

$$C_1 = -\text{sign}(R)\left(|R| + \sqrt{R^2 - Q^3}\right)^{1/3} \quad \text{and} \quad C_2 = \begin{cases} 0 & \text{if } C_1 = 0 \\ Q/C_1 & \text{otherwise .} \end{cases} \tag{2.57}$$

If we obtain three real roots, the center root Z_2 is always thermodynamically unstable and has no physical meaning. The smallest root usually corresponds to a liquid state, i.e., $Z_l = \min(\mathbf{Z})$, and the largest root usually corresponds to the vapor state, i.e. $Z_v = \max(\mathbf{Z})$.[3] For **pure** substances, the most stable root out of two physical roots is quickly identified as the root with the lower Gibbs energy. We can calculate

$$d\underline{g} = \frac{\underline{g}_v - \underline{g}_l}{\mathcal{R}T} = \log\left[\frac{Z_l - B}{Z_v - B}\right] + \frac{A}{B\sqrt{u^2 - 4w}} \log\left[\frac{\Lambda_l^+ \Lambda_v^-}{\Lambda_l^- \Lambda_v^+}\right] - (Z_l - Z_v) \tag{2.58}$$

and if $d\underline{g} < 0$, the vapor state with Z_v is stable. If $d\underline{g} > 0$, the liquid state with Z_l is stable. And only at phase equilibrium $d\underline{g}$ is equal to null. Again, it is important

[3] This may not be true if the smallest volume root is smaller than the co-volume, i.e., $\min(\mathbf{Z}) < B$. Then, the smallest root is unphysical and the largest root may also corresponds to a liquid state.

Algorithm 1 Calculate compressibility factor Z from generalized cubic EOS. See Appendix B for corresponding MATLAB source code.

```
function solveCEOS(u, w, aα, b, root)
    Calculate A, B, a2, a1, a0, R, Q
    if three real roots exist then
        Calculate three real roots Z = {Z1, Z2, Z3} with Eq. (2.54)
        if min(Z) ≤ B then
            // The volume cannot be smaller than the co-volume and only the largest
            // root is physical meaningful
            Z ← max(Z)
        else
            Zl ← min(Z); Zv ← max(Z) // Center root is thermodynamically unstable
            if root = gibbs then
                Calculate dg with Eq. (2.58)
                if dg < 0 then Z ← Zv else Z ← Zl end if
            else if root = liquid then
                Z ← Zl
            else if root = vapor then
                Z ← Zv
            end if
        end if
    else
        Calculate single real root Z with Eq. (2.56)
    end if
    return Z
end function
```

Algorithm 2 Update temperature and pressure for single-phase thermodynamics for fully conservative formulation of the governing equations.

```
function solveSinglephaseFC(z*, v*, e*, T, p)
    if e* > 1 then e_norm = e* else e_norm = 1 end if
    for i ← 1 to iter_max do
        Calculate e with Eq. (2.24) and c_v with Eq. (2.31)
        de ← e* − e
        if |de/e_norm| < ϵ then // We used ϵ = 1 × 10^−6
            Calculate pressure p with Eq. (2.12)
            break
        else
            dT ← de/c_v
            T ← T + dT/(1 + |dT · α|) // We used α = 0.1
        end if
    end for
    return {T, p}
end function
```

to realize that these statements are true only for pure substances.

The algorithm that was used in this work is given in Algorithm 1. Once the compressibility factor is known the volume and all other thermodynamic properties such as internal energy, specific heats or partial properties are calculated in a straight-forward manner.

2.2.3 Conservative to Primitive Variables

Fully Conservative (FC) Method

For the FC formulation of the governing equations the dependent variables are density ρ, internal energy e (as part of the total energy E) and partial densities ρY_i. From these conserved variables, the primitive variables temperature and pressure need to be calculated. For real fluids, this is only possible by an iterative algorithm since there is no explicit expression for $T = f(\rho, e, \rho Y_i)$. Having an explicit expression for the internal energy $\underline{e}$ as function of temperature, volume and composition available, see Eq. (2.24), it is possible to compute the temperature T iteratively by minimizing the objective function

$$F^{FC} = \frac{\underline{e}^\star - \underline{e}_F(T, \underline{v}^\star, \mathbf{z}^\star)}{\underline{e}_{norm}} \tag{2.59}$$

with $\underline{e}^\star = \underline{e}_{LES}$, $\underline{v}^\star = \underline{v}_{LES}$ and $\mathbf{z}^\star = \mathbf{z}_{LES}$ being the molar internal energy, molar volume and overall molar composition that come from the flow solver (after

conversion to molar quantities). To avoid division by zero the normalization reads $\underline{e}_{norm} = \underline{e}^\star$ if $|\underline{e}^\star| > 1$, else $\underline{e}_{norm} = 1$. The algorithm to compute the temperature iteratively is largely inspired from Masquelet (2013) and Hickey et al. (2013) and detailed in Algorithm 2. If the Newton method diverges we resort to the Trust-Region algorithm that is implemented in Intel's MKL library. The initial guess for (p, T) is taken from the previous time step, or the previous Runge-Kutta step. In case an expression for $\underline{e}$ explicit in $(\underline{v}, T, \mathbf{z})$ is not available, as for example for some volume translated EOS, see Matheis et al. (2016) for details, it may also be necessary to simultaneously iterate temperature and pressure. Such an algorithm can be found in Okong'o et al. (2001). Once the temperature is available, the pressure and all other thermodynamic properties and derivatives, e.g., specific heats, speed of sound, partial properties, can be calculated in a straightforward manner. Note that the pressure and temperature resulting from this single-phase model may correspond to unstable thermodynamic states.

Quasi Conservative (QC) Method

For the QC formulation of the governing equations the dependent variables are density ρ, pressure p and partial densities ρY_i. The unknown temperature T can be calculated iteratively by minimizing the objective function

$$F^{QC} = \frac{p^\star - p(T, \underline{v}^\star, \mathbf{z}^\star)}{p^\star} \tag{2.60}$$

with $\underline{v}^\star = \underline{v}_{LES}$, $p^\star = p_{LES}$,and $\mathbf{z}^\star = \mathbf{z}_{LES}$ being the molar volume, pressure, and overall molar composition that come – after conversion to a molar basis – from the flow solver. A similar algorithm as for the FC method is used, see Algorithm 3. Note that the solution to Eq. (2.60) does not involve any caloric properties. Similar to the FC method all other thermodynamic properties and derivatives can be calculated in a straightforward manner once the temperature is available. Again, pressure and temperature resulting from this approach may correspond to unstable thermodynamic states.

2.3 Two-Phase Thermodynamics

In the following paragraph, the two-phase model based on cubic EOS, thermodynamic stability analysis, and VLE calculations is introduced.

Algorithm 3 Update single-phase thermodynamics for QC formulation of the governing equations.

function solveSinglephaseQC$(\mathbf{z}, \underline{v}^\star, p^\star, T)$
  for $i \leftarrow 1$ **to** *iter_max* **do**
    With ($\underline{v}^\star$,T) calculate p, Eq. (2.12), and $\partial p/\partial T|_v$ with Eq. (2.34)
    $dp \leftarrow \underline{p}^\star - p$
    if $|dp/\underline{p}^\star| < \epsilon$ **then** // We used $\epsilon = 1 \times 10^{-6}$
      break
    else
      $dT \leftarrow dp/(\partial p/\partial T|_v)$
      $T \leftarrow T + dT/(1 + |dT \cdot \alpha|)$ // We used $\alpha = 0.1$
    end if
  end for
  return $\{T\}$
end function

2.3.1 Introduction

The equations and procedures introduced in Sec. 2.2 always assume a single homogeneous fluid phase composed of an arbitrary number of components $N_c \geq 1$. We will now focus on multi-component systems, in which two phases can co-exist even though the operating pressure is above the critical pressure p_c of the pure components. In the following, the basic thermodynamic equilibrium equations and the concept of phase stability analysis is discussed. Where appropriate, we take as an example the high-pressure mixing of nitrogen and hydrogen, for which LES results are discussed in Chapter 3.

First, let us introduce the *adiabatic mixing model*, which allows a simple representation of the binary mixture in mixture space[4]: The pure substances nitrogen and hydrogen are initially at a certain temperature T_{N_2} and T_{H_2}, respectively, and the same pressure p. We assume an isobaric and adiabatic hence isenthalpic mixing process between the two pure substances. The enthalpy in the considered systems is

$$\underline{h}\left(T, p, z_1, ..., z_{N_c}\right) = \sum_{i=1}^{N_c} z_i \underline{h}_i\left(T_i, p\right). \tag{2.61}$$

The term on the right-hand side represents the sum of the enthalpies (on a molar basis) of the pure components before mixing, thus, a linear distribution in mixture space. The term on the left-hand side represents the enthalpy of the mixture. If

[4] In Chapter 3 & 4 and Appendix A it is demonstrated that thermodynamic phenomena that take place during the high-pressure injection process can be explained very well with the help of the adiabatic mixing model.

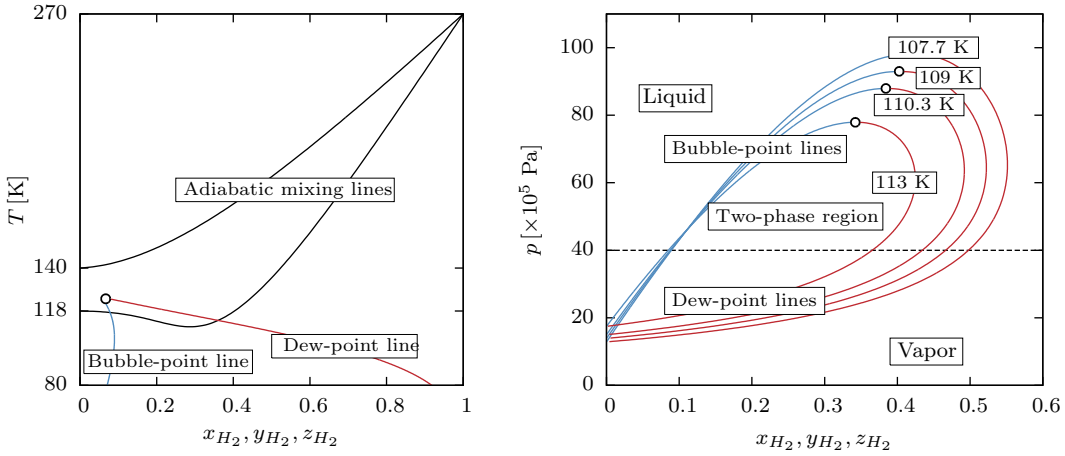

(a) Temperature-composition phase diagram at 4 MPa with (frozen) adiabatic mixture lines.

(b) Pressure-composition phase diagram for several isotherms.

Figure 2.1: Temperature- and pressure-composition phase diagram for a binary hydrogen-nitrogen mixture calculated with the PR EOS and $k'_{12} = 0$. Critical points are indicated by a $\circ$.

we assume that the resulting mixture can exist as a single homogeneous phase, the mixing rules given in Sec. 2.2.1 apply for the mixture enthalpy $\underline{h}\,(T, p, z_1, ..., z_{N_c})$ and the only unknown in Eq. (2.61) is the temperature T after mixing which can be calculated iteratively. Figure 2.1a shows the solution to Eq. (2.61) for ($T_{N_2} = 118$ K, $T_{H_2} = 270$ K, $p = 4$ MPa) and ($T_{N_2} = 140$ K, $T_{H_2} = 270$ K, $p = 4$ MPa) in a temperature-composition phase diagram. On the left-hand side there is pure nitrogen, i.e., $z_{H_2} = 0$, and on the right-hand side there is pure hydrogen at 270 K. Following the notation of Qiu and Reitz (2015), we will call the temperature for which a single homogeneous phase is assumed the frozen adiabatic mixing temperature T_F.

Let us next calculate phase diagrams for **binary mixtures** in order to address the question whether or not the nitrogen-hydrogen mixture can be treated as a single homogeneous phase. In the following, we will assume a binary mixture, that is $N_c = 2$, and that the number of phases is two. We will further restrict ourselves to the discussion of vapor-liquid equilibria. For a thorough discussion of systems with more than two phases or multi-component phase diagrams with $N_c > 2$, the interested reader is referred to Michelsen and Mollerup (2007).

A necessary condition for equilibrium is that the chemical potential (which is the

partial molar Gibbs energy) for each component i is the same in liquid and vapor phases

$$\underline{\mu}_{i,v}(T,p,\mathbf{y}) = \underline{\mu}_{i,l}(T,p,\mathbf{x}) \quad \text{for} \quad i=1,2. \tag{2.62}$$

Here and in the following we denote liquid phase mole fractions by $\mathbf{x}=\{x_1,x_2\}$ and vapor phase mole fractions by $\mathbf{y}=\{y_1,y_2\}$. Even through the chemical potential condition is sufficient to solve VLE problems, an alternative formulation via *component fugacities*[5] has been established historically. The fugacity of a component i in a mixture is defined as

$$\mathcal{R}T d\log f_i = d\underline{\mu}_i. \tag{2.63}$$

The integration of Eq. (2.63) as a function of composition from a state of pure component i (denoted by the superscript 0) to a mixed stated at constant temperature yields

$$\mathcal{R}T \log \frac{f_i(T,p,\mathbf{z})}{f_i^0(T,p)} = \underline{\mu}_i(T,p,\mathbf{z}) - \underline{\mu}_i^0(T,p). \tag{2.64}$$

where the superscript ^{0} refers to the pure fluid state[6]. Plugging Eq. (2.64) into Eq. (2.62) we obtain with $\mathbf{z}=\mathbf{y}$ for the vapor phase and $\mathbf{z}=\mathbf{x}$ for the liquid phase at equilibrium

$$\mathcal{R}T \log \frac{f_{i,v}(T,p,\mathbf{y})}{f_{i,l}(T,p,\mathbf{x})} = \underline{\mu}_{i,v}(T,p,\mathbf{y}) - \underline{\mu}_{i,l}(T,p,\mathbf{x}) = 0 \quad \text{for} \quad i=1,2. \tag{2.65}$$

Thus,

$$f_{i,v}(T,p,\mathbf{y}) = f_{i,l}(T,p,\mathbf{x}) \quad \text{for} \quad i=1,2. \tag{2.66}$$

Introducing the so-called *fugacity coefficient*

$$\varphi_{i,v} = \frac{f_{i,v}}{y_i\, p} \quad \text{and} \quad \varphi_{i,l} = \frac{f_{i,l}}{x_i\, p} \tag{2.67}$$

[5] Fugacity can be interpreted as 'escaping tendency'. For an ideal gas, the component fugacity is the partial pressure. A very comprehensive introduction on the concept of component fugacities can be found in Elliott and Lira (2012), Chapter 10.

[6] Note that $\underline{\mu}_i^0(T,p)$ is simply $\underline{\mu}_i(T,p,\mathbf{z}=\{z_i=1,z_{j\neq i}=0\})$, cf. also Eq. (2.78).

we may rearrange Eq. (2.66) to

$$\log \varphi_{i,v}(T, p, \mathbf{y}) - \log \varphi_{i,l}(T, p, \mathbf{x}) + \log K_i = 0 \quad \text{for} \quad i = 1, 2. \tag{2.68}$$

The ratio of vapor mole fraction to liquid mole fraction is also known as K-factor (or K-ratio or equilibrium factor)

$$K_i = \frac{y_i}{x_i} = \frac{\varphi_{i,l}}{\varphi_{i,v}}. \tag{2.69}$$

The logarithm of the fugacity coefficient φ_i of component i can be calculated from the chemical potential, cf. Eq. (2.48),

$$\log \varphi_i(T, p, \mathbf{z}) = \log \left(\frac{f_i}{z_i\, p} \right) = \frac{\underline{\mu}_i - \underline{\mu}_i^{\mathrm{ig}}}{\mathcal{R}T} \tag{2.70}$$

with $\mathbf{z} = \mathbf{y}$ for the vapor phase and $\mathbf{z} = \mathbf{x}$ for the liquid phase. Note that the superscript $^{\mathrm{ig}}$ refers to the ideal reference state and not the pure fluid. Equation 2.68 together with the condition that the mole fractions in the liquid and vapor phase must sum to unity, i.e.,

$$x_1 + x_2 = 1 \quad \text{and} \quad y_1 + y_2 = 1, \tag{2.71}$$

yield 4 equations relating the 6 variables T, p, x_1, x_2, y_1 and y_2. With a specification of pressure p and temperature T, bubble-point and dew-point lines can be solved iteratively in a straight-forward manner for the unknown vapor mole fractions $\mathbf{y}$ and liquid mole fractions $\mathbf{x}$.

Figure 2.1a depicts the bubble- and dew-point line in a temperature-composition phase diagram (also known as Txy-diagram) at a fixed pressure of 4 MPa. For the sake of completeness, we show the solution to Eq. (2.68) also in a pressure-composition phase digram (or pxy-diagram) for several isotherms. Both diagrams are encountered frequently in thermodynamics textbooks. Experimental VLE data are often composed in a pxy-diagram. The Txy-diagram at fixed pressure, however, is more intuitive to read for isobaric injection or mixing processes. Also note that for $N_c > 2$ a two-dimensional representation of dew- and bubble-point lines in mixture space is not possible. We can now see that for $T_{N_2} = 118$ K some states along the adiabatic mixing line lie well within the two-phase region. Here, the assumption of a single homogeneous phase does not hold. As pointed out by Qiu and Reitz (2015) the mixture enthalpy $\underline{h}\,(T, p, z_1, ..., z_{N_c})$ in Eq. (2.61) is not only a function of the temperature but also a function of the number of phases and their identities. For the higher initial nitrogen temperature $T_{N_2} = 140$ K, the mixture

line does not enter the two-phase region and the single-phase EOS as introduced in Sec. 2.2 is sufficient to describe the PVT behavior of the mixture.

In the following, a brief introduction in phase-stability analysis is given, which will allow us to identify thermodynamically unstable states in the LES. Once identified, we will then apply the *homogeneous mixture* approach in order to represent both liquid and vapor phases in a computational cell.

2.3.2 Thermodynamic Stability Analysis

A mixture is considered stable at the current temperature and pressure if and only if the total Gibbs energy is at its global minimum (Michelsen and Mollerup, 2007). Whether a split into two phases yields a decrease in the Gibbs energy, or, in other words, whether the fluid state within a computational cell lies within the two-phase region or not is determined by the Tangent Plane Distance (TPD) function (Michelsen, 1982b). Consider a N_c-component mixture with $N_c \geq 2$ of composition $\mathbf{z}$ at a given temperature T and pressure p. For a trial phase composition $\mathbf{w} = \{w_1, \ldots, w_{N_c}\}$, the TPD is expressed by

$$TPD(\mathbf{w}) = \sum_{i=1}^{N_c} w_i[\underline{\mu}_i(\mathbf{w}) - \underline{\mu}_i(\mathbf{z})] \tag{2.72}$$

with $\underline{\mu}_i$ being the chemical potential of component i. Introducing the fugacity coefficient φ_i, Eq. (2.72) is commonly expressed in a dimensionless form

$$tpd = \frac{TPD}{\mathcal{R}T} = \sum_{i=1}^{N_c} w_i(\ln \varphi_i(\mathbf{w}) + \ln w_i - d_i(\mathbf{z})) \tag{2.73}$$

with

$$d_i(\mathbf{z}) = \ln \varphi_i(\mathbf{z}) + \ln z_i. \tag{2.74}$$

The phase of composition $\mathbf{z}$ is considered stable at the specified temperature T and pressure p if and only if

$$tpd(\mathbf{w}) \geq 0 \quad \forall \quad w_i \geq 0 \quad \text{such that} \quad \sum_{i=1}^{N_c} w_i = 1. \tag{2.75}$$

A widely used approach to solve Eq. (2.75) is to calculate the stationary points of the *tpd* function, i.e., points where the derivative with respect to all independent variables is equal to zero (Michelsen, 1982b). Then, non-negativity at all stationary points proves that the mixture is stable. For comprehensive reviews, alternative formulations and solution methods the interested reader is referred to Michelsen (1982b), Firoozabadi (1999), Hoteit and Firoozabadi (2006) and Michelsen and Mollerup (2007). For the present work, we followed the recommendation of Qiu et al. (2014a) and implemented the BFGS-quasi-Newton algorithm. Detailed pseudocode is not presented in this work but can be found in Hoteit and Firoozabadi (2006). A MATLAB code for the *TPD* test can also be found in the library described in Appendix B.

Recall our example of the binary nitrogen-hydrogen mixture. Figure 2.2a depicts a zoomed view of the temperature-composition diagram introduced in Sec. 2.3.1 together with the frozen adiabatic mixing temperature T_F. The crosses labeled (1), (2) and (3) in Fig. 2.2a represent characteristic points along T_F. Point (1) is located outside, point (2) and (3) are located well within the two-phase region. Figures 2.2b-2.2d (bottom) depict the Gibbs energy of mixing

$$\frac{\Delta g}{\mathcal{R}T} = z_{H_2}\left(\frac{\underline{\mu}_{H_2}(T,p,\mathbf{z}) - \underline{\mu}^0_{H_2}(T,p)}{\mathcal{R}T}\right) + z_{N_2}\left(\frac{\underline{\mu}_{N_2}(T,p,\mathbf{z}) - \underline{\mu}^0_{N_2}(T,p)}{\mathcal{R}T}\right) \quad (2.76)$$

plotted as function of the hydrogen mole fraction z_{H_2} at the corresponding temperatures $T_{(1)} = 114.11$ K, $T_{(2)} = 111.62$ K and $T_{(3)} = 112.30$ K and a pressure of 4 MPa. In Eq. (2.76), $\underline{\mu}_i$ is the chemical potential of component i

$$\frac{\underline{\mu}_i(T,p,\mathbf{z}) - \underline{\mu}^0_i(T,p)}{\mathcal{R}T} = \log\left(\frac{f_i}{f^0_i}\right) = \log\varphi_i(T,p,\mathbf{z}) + \log(z_i) - \log\varphi^0_i(T,p) \quad (2.77)$$

and the superscript ^{0} refers to the pure component value, e.g.,

$$\varphi^0_{H_2}(T,p) = \varphi_{H_2}(T,p,\mathbf{z} = \{z_{H_2} = 1, z_{N_2} = 0\}), \quad (2.78)$$

and not to the ideal reference state (which is denoted by the superscript $^{\mathrm{ig}}$). For binary mixtures, a graphical interpretation of the *tpd* function and stability conditions is illustrative. Geometrically, the *tpd* function represents – for a binary mixture – the distance from the tangent line to the Gibbs energy curve at $\mathbf{z}$ to the Gibbs energy curve at $\mathbf{w}$. Recall Fig. 2.2b showing the molar Gibbs energy of mixing $\Delta g/(\mathcal{R}T)$ at $T_{(1)} = 114.11$ K together with the *tpd* function evaluated at $z_{H_2} = 0.37$. The dashed line represents the tangent line to the Gibbs energy curve at $z_{H_2} = 0.37$. The *tpd* for all $\mathbf{w}$ is always positive and the trivial solution $\mathbf{w} = \mathbf{z}$

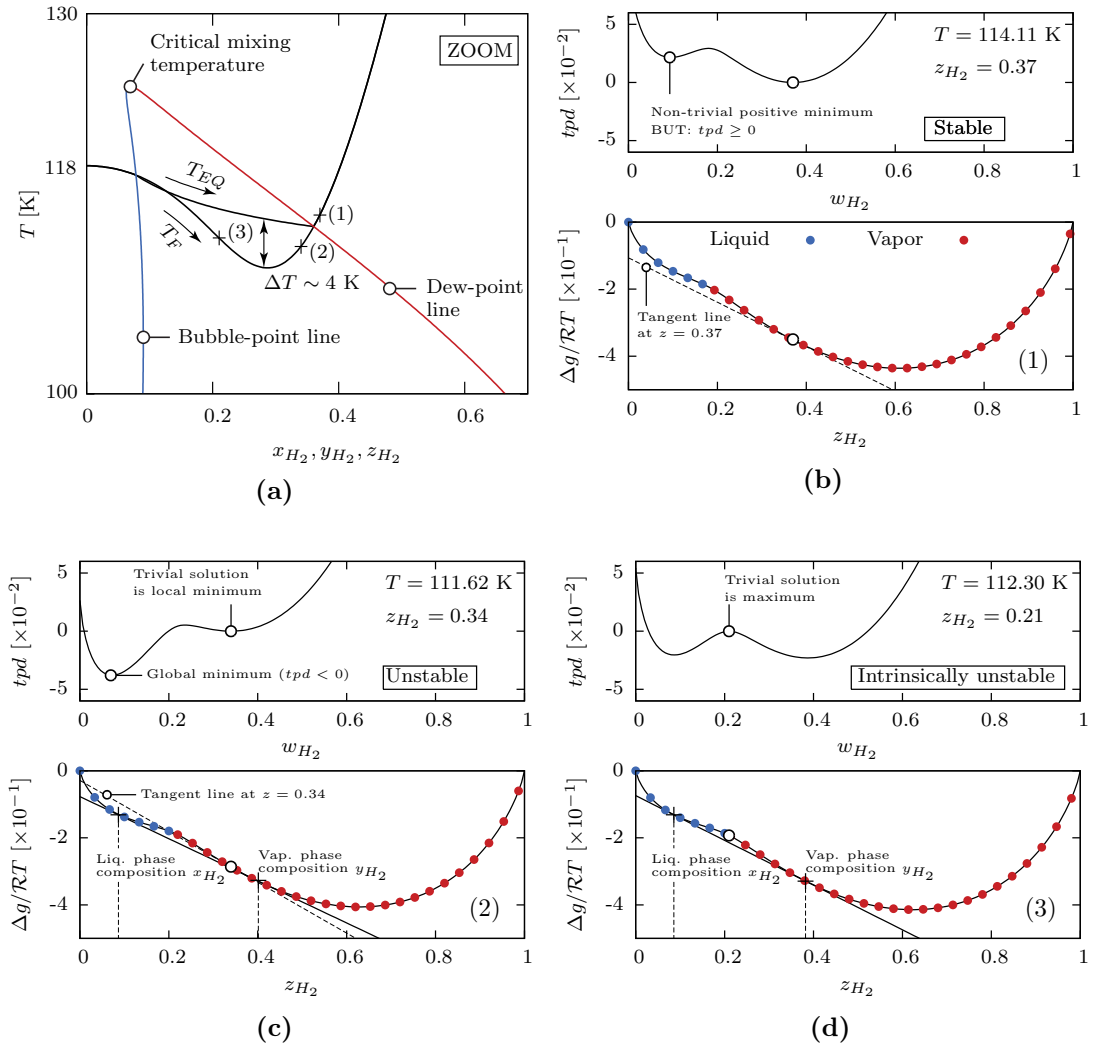

Figure 2.2: (a) Enlarged view of the binary phase diagram of Fig. 2.1. The crosses labeled (1), (2) and (3) represent characteristic points along the frozen adiabatic mixing temperature line T_F. T_{EQ} refers to the equilibrium adiabatic mixing temperature, see Sec. 2.3.5. (b)-(d) Gibbs energy of mixing $\Delta g/(\mathcal{R}T)$ together with the *tpd* function, Eq. (2.73), plotted as function of the hydrogen mole fraction at the temperatures (b) $T_{(1)} = 114.11$ K, (c) $T_{(2)} = 111.62$ K and (d) $T_{(3)} = 112.30$ K and a pressure of 4 MPa. A MATLAB source code (`main_N2_H2.m`) which produces similar figures is provided as supplementary material, see Appendix B.

constitutes a global minimum of the *tpd* function. The mixture is therefore stable and exists as single phase. Figure 2.2c shows the corresponding plots for point (2), which is located within the two-phase region. Note that the solid line does not represent the tangent line to the Gibbs energy curve at $z_{H_2} = 0.34$ but the common tangent to the Gibbs energy curve at compositions x_{H_2} (liquid) and y_{H_2} (vapor). For $T_{(2)} = 111.62$ K, overall compositions in the range $x_{H_2} < z_{H_2} < y_{H_2}$ are not stable and split into two equilibrium phases. With *tpd* being negative at a non-zero distance from $\mathbf{z}$, the mixture with $z_{H_2} = 0.34$ is in a metastable state. Point (3), Fig. 2.2d, shows the case for which a mixture is called intrinsically unstable. The trivial solution $\mathbf{w} = \mathbf{z}$ of the *tpd* constitutes a local maximum. In such a situation the mixture is located within the spinodal curve (Michelsen and Mollerup, 2007). Other illustrative examples for the *tpd* function and its graphical interpretation can also be found in Michelsen and Mollerup (2007).

2.3.3 The Isothermal Two-Phase Flash

The equilibrium calculation at specified temperature T, pressure p and overall composition $\mathbf{z}$ is known as isothermal flash calculation or as TP$\mathbf{n}$ flash. Robust solution algorithms are available in literature. Here, we follow the implementation strategy described by Michelsen (1982a) and Michelsen and Mollerup (2007) (Chapter 10), which is often referred to as *successive substitution method* (or direct substitution method). Other flash calculations, for example at specified internal energy, volume and overall composition (see Sec. 2.3.4) or at specified enthalpy, pressure and overall composition (see Sec. 2.3.5) are then solved by a nested-loop approach using an isothermal flash in the innermost loop combined with an outer loop for the temperature/pressure adjustment.

Let us consider a mixture with the overall composition $\mathbf{z}$. Again, the maximum number of phases is two. Under isothermal and isobaric conditions, the necessary condition of thermodynamic equilibrium is that the fugacity f_i of each component i is the same in both phases, i.e.,

$$f_{i,v}(T, p, \mathbf{y}) = f_{i,l}(T, p, \mathbf{x}) \quad \text{for} \quad i = 1, 2 \ldots N_c \tag{2.79}$$

or, equivalently, in terms of the fugacity coefficient φ_i and K-factor

$$F_i = \log[\varphi_{i,v}(T, p, \mathbf{y})] - \log[\varphi_{i,l}(T, p, \mathbf{x})] + \log(K_i) = 0 \quad \text{for} \quad i = 1, \ldots, N_c. \tag{2.80}$$

The material balance for each component,

$$\underline{\alpha}_v y_i + (1 - \underline{\alpha}_v) x_i = z_i, \tag{2.81}$$

with $\underline{\alpha}_v$ being the overall molar vapor fraction, and the requirement that mole fractions in the liquid and vapor phase must sum to unity, or equivalently

$$\sum_{i=1}^{N_c} (y_i - x_i) = 0, \tag{2.82}$$

yield $(2N_c + 1)$ equations, which can be solved for the unknown compositions $\mathbf{x} = \{x_1, \ldots, x_{N_c}\}$ and $\mathbf{y} = \{y_1, \ldots, y_{N_c}\}$ of liquid and vapor phases, and the molar vapor fraction $\underline{\alpha}_v$. An alternative formulation of Eqs. (2.79)-(2.82) can be achieved by substituting the equilibrium factors $\mathbf{K} = \{K_1, \ldots, K_{N_c}\}$ into the material balance, Eq. (2.81), which yields

$$x_i = \frac{z_i}{1 - \underline{\alpha}_v + \underline{\alpha}_v K_i} \qquad \text{and} \qquad y_i = \frac{K_i z_i}{1 - \underline{\alpha}_v + \underline{\alpha}_v K_i}. \tag{2.83}$$

Equation (2.82) together with Eq. (2.83) can be recast in

$$\sum_{i=1}^{N_c} (y_i - x_i) = \sum_{i=1}^{N_c} \frac{z_i (K_i - 1)}{1 - \underline{\alpha}_v + \underline{\alpha}_v K_i} = 0, \tag{2.84}$$

which is known as *Rachford-Rice* equation. Equation (2.84) is a monotonically decreasing function and a solution $0 < \underline{\alpha}_v < 1$ exists provided $\sum_{i=1}^{N_c} K_i z_i > 1$ and $\sum_{i=1}^{N_c} z_i / K_i > 1$. For an assumed set of K-factors (a.k.a. initial guess) the Rachford-Rice equation can be solved for the vapor fraction $\underline{\alpha}_v$ (see Michelsen and Mollerup (2007) for comprehensive pseudocode). Having the vapor fraction $\underline{\alpha}_v$ available allows the calculation of liquid phase compositions $\mathbf{x}$ and vapor phase compositions $\mathbf{y}$ via Eq. (2.83). Next we can calculate the fugacity coefficients φ_i, see Eq. (2.70), and check convergence of the objective function in Eq. (2.80). If not converged, a new set of K-factors is readily available from the fugacity coefficients (which represent our thermodynamic model) because $K_i = \varphi_{i,l}(T, p, \mathbf{x}) / \varphi_{i,v}(T, p, \mathbf{y})$. The algorithm that was used in this work is detailed in Algortihm 4 and available as MATLAB source code, see Appendix B.[7] Following the recommendation of

[7] We also included a Newton method for the isothermal flash, which may be faster but not as fail-safe as the successive substitution method. The Newton method with analytical Jacobian matrix is described in detail in Michelsen and Mollerup (2007), Chapter 10.

Algorithm 4 Equilibrium calculation at specified temperature T, pressure p and overall composition $\mathbf{z}$ (successive substitution method). See Appendix B for corresponding MATLAB source code.

```
function solveTPn(z, T, p, K)
  if not present K then initialize K-factors K with Wilson correlation end if
  for n ← 1 to iter_max do
    if Σ_{i=1}^{Nc} K_i z_i > 1 and Σ_{i=1}^{Nc} z_i/K_i > 1 then // Criterion that solution exists
      Solve Rachford-Rice equation for the vapor fraction α_v
      // See Michelsen and Mollerup (2007), pp. 252-254 for detailed pseudocode
    else if Σ_{i=1}^{Nc} z/K ≤ 1 then
      α_v ← 1; x_i ← z_i/K_i; y_i ← z_i; Normalize x // Eqs. (7)-(8) in Michelsen (1982a)
    else if Σ_{i=1}^{Nc} K_i z_i ≤ 1 then
      α_v ← 0; x_i ← z_i; y_i ← K_i · z_i; Normalize y
    end if
    Calculate liq. and vap. phase compositions x and y with α_v and K, see Eq. (2.83)
    Calculate EOS parameters for liquid and vapor phase compositions, see Eq. (2.19)
    Calculate liquid volume v_l and vapor volume v_v from EOS, see Algorithm 1
    Calculate logarithm of fugacity coefficients for both phases with equation Eq. (2.70)
    Calculate objective function, Eq. (2.80)
    if |F| ≤ ε_o then // We used ε_o = 1 × 10^{-8}
      break
    else
      K_i ← exp(ln φ_{i,l} − ln φ_{i,v}) // Successive substitution: update K-factors
    end if
  end for
  return {x, y, α_v}
end function
```

Michelsen and Mollerup (2007) we use Wilson's correlation

$$\ln K_i = \ln\left(\frac{p_{c,i}}{p}\right) + 5.373\,(1+\omega_i)\left(1-\frac{T_{c,i}}{T}\right) \tag{2.85}$$

to generate an initial set of K-factors – provided neither time history nor an initial guess via the *TPD* stability test is available.

2.3.4 The Isoenergetic-Isochoric Flash

In the following we describe the algorithm that is used to update temperature and pressure in a computational cell. For the FC formulation of the governing equations, the dependent variables are density ρ, internal energy e (as part of the total energy E) and partial densities ρY_i. Let us assume that the thermodynamic state of the mixture (single-phase or two-phase) is unknown. Then, we calculate

(T, p) with the single-phase EOS model, see Sec. 2.2.3 and Algorithm 2. Whether temperature and pressure (T, p) resulting from this single-phase model correspond to unstable thermodynamic states or not can be determined with the *TPD* analysis, see Sec. 2.3.2. If the result of the *TPD* test tells us that the single-phase mixture is stable we are good. If it turns out that the mixture is unstable, which means that the fluid would prefer to exist as two phases, then we solve the so-called *isoenergetic-isochoric flash* problem, i.e., thermodynamic equilibrium calculations at specified internal energy, volume and composition. This type of flash calculation is more difficult to solve than others because neither temperature nor pressure are known in advance. Here, we describe the nested-loop solution. The corresponding objective function for the isoenergetic-isochoric flash problem reads

$$\mathbf{F} = \left\{ \frac{\underline{v}^\star - \underline{v}_{EQ}(T, p, \mathbf{z}^\star)}{\underline{v}^\star}, \frac{\underline{e}^\star - \underline{e}_{EQ}(T, p, \mathbf{z}^\star)}{\underline{e}_{norm}} \right\} \tag{2.86}$$

with $\underline{e}^\star = \underline{e}_{LES}$, $\underline{v}^\star = \underline{v}_{LES}$ and $\mathbf{z}^\star = \mathbf{z}_{LES}$ being the molar internal energy, molar volume and overall molar composition that come from the flow solver (after conversion to molar quantities). To avoid division by zero the normalization reads $\underline{e}_{norm} = \underline{e}^\star$ if $|\underline{e}^\star| > 1$, else $\underline{e}_{norm} = 1$. Equilibrium volume $\underline{v}_{EQ}$ and energy $\underline{e}_{EQ}$ in Eq. (2.86) are then obtained through

$$\underline{v}_{EQ}(T, p, \mathbf{z}^\star) = \underline{\alpha}_v \underline{v}_v + (1 - \underline{\alpha}_v)\underline{v}_l \tag{2.87}$$

and

$$\underline{e}_{EQ}(T, p, \mathbf{z}^\star) = \underline{\alpha}_v \underline{e}_v + (1 - \underline{\alpha}_v)\underline{e}_l. \tag{2.88}$$

Liquid phase molar volume $\underline{v}_l(T, p, \mathbf{x})$ and energy $\underline{e}_l(T, p, \mathbf{x})$ and vapor phase molar volume $\underline{v}_v(T, p, \mathbf{y})$ and energy $\underline{e}_v(T, p, \mathbf{y})$ are available as solution to the isothermal flash (which provides liquid phase composition $\mathbf{x} = \{x_1, \ldots, x_{N_c}\}$, vapor phase composition $\mathbf{y} = \{y_1, \ldots, y_{N_c}\}$ and vapor faction $\underline{\alpha}_v$). The outer-loop iteration is done by a multi-dimensional Newton iteration in T and p with numerical approximation of the Jacobian matrix. In case of divergence we resort to the Trust-Region algorithm that is implemented in Intel's MKL library. Note that a more efficient solution for the isoenergetic-isochoric flash problem can be achieved by direct entropy maximization, see Castier (2009) and Qiu et al. (2014b,a). Very helpful information on the isoenergetic-isochoric flash problem can also be found in Saha and Carroll (1997).

The algorithm that was used in this work is given in Algorithm 5. There are a number of noteworthy aspects: **1.** History from previous time- or Runge-Kutta steps (superscript $^{n-1}$) is stored for temperature T, pressure p, K-factors K_i, and

vapor fraction $\underline{\alpha}_v$. **2.** If the previous thermodynamic state in a computational cell is unknown we must start with a single-phase assumption to obtain (p, T). In Algorithm 5, an unknown state may correspond to a situation where no history is available, e.g., during initialization, or the previous thermodynamic state was stable. **3.** If the computational cell was in a two-phase state at the previous time- or Runge-Kutta step, we do not evaluate the single-phase thermodynamic model and do not perform the *TPD* test (in the first place). Instead, we assume that the mixture is two-phase and solve the isoenergetic-isochoric flash. If the flash converges to the trivial solution[8], we evaluate the single-phase thermodynamic model and undertake the *TPD* test. If the mixture turns out to be stable, we are good. This situation represents a computational cell that transitions from a two-phase state to single-phase state. If the *TPD* test tells us that the mixture is unstable we either solve the isoenergetic-isochoric flash again with a new initial guess for K_i (which now comes from the *TPD* test and not from the previous time step) or just move on. In this work, the latter was done but it must be noted that this situation did rarely happen for the cases under consideration. **4.** If the temperature from the previous time step is above a certain threshold, we assume the mixture to be stable and solve for (p, T) under the single-phase assumption. We used in all subsequent simulations as threshold 1.2 times the critical mixing temperature (which is shown for a binary nitrogen-hydrogen mixture at $p = 4$ MPa in Fig. 2.2) at the corresponding nominal operation pressure. **5.** We assumed mixtures with any $z_i > 0.9999$ to be stable. The latter two aspects may lead to an improved performance because of a reduced usage of the *TPD* test. However, note that single-species two-phase states, as present, e.g., in cavitating nozzles of fuel injectors, are excluded by the last statement. An extension of the homogeneous mixture approach to single-component two-phase flows within the cubic EOS framework is possible, see, e.g., Star et al. (2006) and Qiu and Reitz (2014).

The single-fluid approach for modeling multi-component subcritical two-phase states is employed with the following underlying assumptions:

- The fluid is in local thermodynamic and chemical equilibrium.
- Phase interfaces are in mechanical equilibrium and surface tension effects are neglected, i.e. $p = p_l = p_v$.

[8]The so-called trivial solution to Eqs. (2.79)-(2.82) is the solution for which liquid and vapor phases have identical compositions, i.e., $\mathbf{x} = \mathbf{y}$. There are situations in which the trivial solution is the only valid solution, but it may also happen that the initial guess is not sufficiently precise and the true phase equilibrium solution is not found. We assumed solutions with $\sum_{i=1}^{N_c}(|x_i - y_i|) < 1 \times 10^{-6}$ to be trivial.

- The phase-transition (evaporation or condensation) timescale is small compared to the flow timescale.
- There is a single-valued velocity for both phases (no-slip).

The present approach yields a unified framework valid for both multi-component subcritical two-phase states but also multi-component supercritical states. A comparison with experimental results in Chapter 3 & 4 will provide a justification for applying the homogeneous mixture methodology for LES of sprays under high-pressure conditions. For reasons to be discussed in Chapter 4, we implemented the two-phase model only for the FC formulation of the governing equations. We further want to emphasize that this model is inspired by the work of Qiu and Reitz (2014, 2015), who apply a similar approach in the context of RANS simulations.

2.3.5 The Isenthalpic Flash

In Sec. 2.3.1, we introduced the adiabatic mixing model and assumed that the mixture enthalpy $\underline{h}\,(T, p, z_1, ..., z_{N_c})$ is only a function of temperature (at specified pressure and overall composition). As pointed out by Qiu and Reitz (2015) this may be a false assumption because the solution to Eq. (2.61) must ensure that the Gibbs energy of the mixture is at its global minimum. This means that $\underline{h}\,(T, p, z_1, ..., z_{N_c})$ is not only a function of temperature but also a function of the number of phases and their identities. Equilibrium calculations at specified enthalpy, pressure and overall composition are known as *isenthalpic flash* and the corresponding objective function reads

$$F_h = \frac{\underline{h}^\star - \underline{h}_{EQ}(T_{EQ}, p^\star, \mathbf{z}^\star)}{\underline{h}^\star}, \tag{2.89}$$

with $h^\star$, $p^\star$ and $\mathbf{z}^\star$ being the specified enthalpy, pressure and overall mole fraction in the analytical model, see Eq. (2.61). The equilibrium enthalpy h_{EQ} is calculated from

$$\underline{h}_{EQ}(T, p^\star, \mathbf{z}^\star) = \underline{\alpha}_v \underline{h}_v + (1 - \underline{\alpha}_v)\underline{h}_l \tag{2.90}$$

where $\underline{\alpha}_v$, $\underline{h}_v$ and $\underline{h}_l$ denote the vapor fraction on a molar basis and the molar enthalpy of the vapor and liquid phase, respectively. Vapor fraction and enthalpies of the liquid and vapor phase are calculated by solving an isothermal flash. The solution to Eq. (2.89) yields the equilibrium adiabatic mixing temperature T_{EQ}

Algorithm 5 Update temperature and pressure using the two-phase model and the fully-conservative formulation of the governing equations.

Input: Density ρ, partial densities ρY_i of species $i = \{1 \dots N_c\}$ and internal energy e; temperature T^{n-1}, pressure p^{n-1}, K-factors $\mathbf{K}^{n-1}$ and molar vapor fraction $\underline{\alpha}_v^{n-1}$ from last time- or RK-step
Output: T^n, p^n, $\mathbf{K}^n$ and $\underline{\alpha}_v^n$ at current time- or RK-step
Convert input to molar quantities and calculate overall molar composition $\mathbf{z}$
$p^n \leftarrow p^{n-1}$; $T^n \leftarrow T^{n-1}$; $\mathbf{K}^n \leftarrow \mathbf{K}^{n-1}$; $\underline{\alpha}_v^n \leftarrow \underline{\alpha}_v^{n-1}$ // Best guess for solution
if T^n is greater than a certain threshold **then**
  // Speed up your LES and do TPD/VLE only where it is necessary.
  // Threshold could be 1.2 × critical mixing temperature.
  $state^n \leftarrow$ *singlephase*; *mixture* $\leftarrow$ *stable*
else if any z_i is greater than a certain threshold **then**
  // We assumed mixtures with any z_i greater 0.9999 to be stable.
  $state^n \leftarrow$ *singlephase*; *mixture* $\leftarrow$ *stable*
else if $state^{n-1} =$ *multiphase* **then**
  // The cell was in a two-phase state last time step or Runge-Kutta step
  $state^n \leftarrow$ *multiphase*; *mixture* $\leftarrow$ **not**(*stable*)
else
  $state^n \leftarrow$ *unknown*; *mixture* $\leftarrow$ *stable*
end if
if $state^n =$ *unknown* **or** $state^n =$ *singlephase* **then**
  $\{T^n, p^n\} \leftarrow$ **SolveSinglephase**$(\mathbf{z}, \underline{v}, \underline{e}, T^n, p^n)$ // Compute single-phase solution
  if $T^n < 0.$ **or** $p^n < 0.$ **then**
    $state^n \leftarrow$ *multiphase*; *mixture* $\leftarrow$ **not**(*stable*) // There will be no TPD test
    $p^n \leftarrow p^{n-1}$; $T^n \leftarrow T^{n-1}$
    Initialize K-factors $\mathbf{K}^n$ with Wilson equation and p^{n-1} and T^{n-1}
  end if
end if
if $state^n =$ *unknown* **then**
  $\{mixture, \mathbf{K}^n\} \leftarrow$ **SolveTPD**$(\mathbf{z}, T^n, p^n)$
end if
if *mixture* = *stable* **then**
  $state^n \leftarrow$ *singlephase*
  if the mixture with volume $\underline{v}$ is a liquid **then** $\underline{\alpha}_v^n = 0$ **else** $\underline{\alpha}_v^n = 1$ **end if**
else
  $\{T^n, p^n, \mathbf{x}^n, \mathbf{y}^n, \underline{\alpha}_v^n\} \leftarrow$ **SolveIsoenergeticIsochoric**$(\mathbf{z}, \underline{e}, \underline{v}, T^n, p^n, \mathbf{K}^n, \underline{\alpha}_v^n)$
  if sum(abs(**x** - **y**)) is greater than a certain threshold **then**
    // We may have found the trivial solution $\mathbf{y}^n = \mathbf{x}^n$. We used as threshold 1×10^{-6}
    $state^n \leftarrow$ *multiphase*
    $\mathbf{K}^n \leftarrow \mathbf{y}^n / \mathbf{x}^n$ // Element wise division
  else
    $p^n \leftarrow p^{n-1}$; $T^n \leftarrow T^{n-1}$
    $\{T^n, p^n\} \leftarrow$ **SolveSinglephase**$(\mathbf{z}, \underline{v}, \underline{e}, T^n, p^n)$
    $state^n \leftarrow$ *singlephase*
    if the mixture with volume $\underline{v}$ is a liquid **then** $\underline{\alpha}_v^n = 0$ **else** $\underline{\alpha}_v^n = 1$ **end if**
    $\{mixture, \mathbf{K}^n\} \leftarrow$ **SolveTPD**$(\mathbf{z}, T^n, p^n)$
    if *mixture* is **not**(*stable*) **then**
      We did not find the solution and may call SolveIsoenergeticIsochoric again
    end if
  end if
end if

which is shown in Fig. 2.2a. Note that Eq. (2.89) is solved only within the two-phase region, which is identified with the *TPD* stability analysis. T_{EQ} and T_F collapse outside of the two-phase region.

2.4 Numerical Method

The velocity field of turbulent flows is three-dimensional, time-dependent and chaotic (Pope, 2000). The difficulty of computing and modeling turbulent flows lies in the broad range of spatial and temporal scales. The largest turbulent motions of size L depend upon geometry and boundary conditions. The smallest dissipative motions are characterized by the Kolmogorov length scale l_η. For isotropic turbulence, the ratio of both length scales L/l_η is proportional to (Reynolds number)$^{3/4}$, cf. Pope (2000), which provides a direct link to the grid resolution that is required to resolve the Kolmogorov dissipation scale. The Direct Numerical Simulations (DNS) of the governing equations, Eqs. (2.1)-(2.5), requires the resolution of all length and time scales (because no turbulence model is applied). Rough estimates suggest that turbulent flows at high Reynolds number are therefore out of reach for DNS – even with todays computational capacities.

For flows at high Reynolds numbers Large-Eddy Simulation (LES) is becoming a more widely used simulation tool – also outside the realm of academic research. In LES, the grid on which the governing equations are solved numerically is too coarse to represent the entire range of turbulent length scales.[9] As a consequence, the energy transfer between the smallest and largest scales is not resolved and a subgrid-scale (SGS) model is required to represent the influence of non-resolved turbulent scales. Following the argument of Hickel et al. (2014),e.g., only the large resolved scales provide a direct representation of the energy-containing flow structures, which in fact is adequate for most practical purposes in engineering. These energy-containing large motions are directly affected by boundary conditions and hence are not universal.

The numerical solution of the conservation equations implicitly generates a scale separation through both the use of a computational grid of finite spacing and through the numerical discretization of continuous operators. Following the approach of Leonard (1975), this implicit scale separation can also be expressed as a *convolution* of the governing equations with a homogeneous filter kernel yielding

[9] The smallest temporal scales are typically assumed to be resolved by choosing a sufficiently small time step (Adams et al., 2004)

the filtered Navier-Stokes equations, see e.g., Garnier et al. (2009) for a more detailed discussion. Filtering of nonlinear terms in the Navier-Stokes equations leads to unclosed SGS terms, which need to be modeled. There are *explicit* and *implicit* SGS models. SGS effects are modeled explicitly if the filtered governing equations are augmented by additional terms to account for SGS effects and the resulting system of equations is subsequently discretized. Standard explicit SGS models rely on the assumption that turbulence model and numerical dissipation from truncation errors do not interfere. At grid resolutions that are typically used for LES, this basic assumption is not necessarily met and the truncation error of the discretization scheme can dominate SGS-model terms, see, e.g., Adams et al. (2004) and Hickel et al. (2014), and references therein. Implicit LES (ILES) approaches, on the other hand, make use of the fact that numerical truncation errors resulting from the discretization of the unmodified governing equations can in principle act as SGS model. Here, the difficulty is to modify the truncation error in such a way that dissipation and diffusion of resolved flow scales is consistent with flow physics. In this work, the *Adaptive Local Deconvolution Method* (ALDM) is used. ALDM is a nonlinear finite-volume (FV) scheme for ILES and has been developed for incompressible (Adams et al., 2004; Hickel et al., 2006) and compressible turbulence (Hickel et al., 2014). The method operates on the discretization of the hyperbolic flux which is mainly responsible for SGS effects. Free parameters that result from the the reconstruction procedure (approximation of the unfiltered solution at cell faces) and secondary regularization within the numerical flux function are used to calibrate the spatial truncation error of the FV scheme such that a physically motivated turbulence model consistent with turbulence theory is obtained. A much more detailed description of the original ALDM framework can be found in Adams et al. (2004), Hickel et al. (2006) and Hickel et al. (2014).

Due to the large density gradients that are present in real-gas flows as considered in this work, a modification of the original ALDM scheme as documented in Hickel et al. (2014) was necessary to enhance numerical stability. At contact discontinuities, numerical oscillations were observed for the mass density ρ, partial densities ρY_i and internal energy e. When converting conservative to primitive variables in the non-linear cubic EOS framework, severe pressure and temperature oscillations occurred causing a blow-up of the numerical solution. The following modifications led to a significant improvement of the numerical stability: **1.** A second-order upwind biased numerical flux function together with the van Albada limiter (van Albada et al., 1982) for the advective transport of mass and internal energy removed all oscillations and numerically computed values of the species mass fraction Y_i from $(\rho Y_i)/\rho$ were bounded in the interval [0,1]. **2.** Any contribution of the shock sensor to the dissipation matrix, cf. Eq. (37) in Hickel et al. (2014), was

omitted since the upwinding itself introduced a sufficient amount of dissipation.

The viscous flux of the governing equations is discretized with a 2^{nd} order central difference scheme, and the 3^{rd} order explicit Runge-Kutta scheme of Gottlieb and Shu (1998) is used for time integration. The left-hand side of the pressure-evolution equation of the quasi-conservative method, Eq. (2.5), is discretized consistently with the transport of internal energy such that both discretizations are identical up to machine precision for a single-species perfect gas ($N_c = 1$, $c_v \neq f(T)$ and $p = (c_p/c_v - 1)\rho e$).

Chapter 3

LN2-GH2 Shear Coaxial Flow

In this chapter, we will study a selected operating point of a series of experiments of Oschwald et al. (1999), in which quantitative density measurements in coaxial liquid nitrogen (LN2) and gaseous hydrogen (GH2) jets at supercritical pressures (with respect to the critical pressure of pure nitrogen and pure hydrogen) were obtained. Emphasis is placed on both a quantitative and qualitative comparison between experimental and numerical data and the assessment of uncertainties related to both of them. In particular, two-phase phenomena that occur at the present operating conditions and the accuracy of the thermodynamic modeling approach will be addressed. All results presented in this chapter are simulated with the flow solver INCA and the numerical framework introduced in Chapter 2. The interested reader may find additional results for this test case obtained with other CFD codes and volume translated EOS in Müller et al. (2015), Matheis et al. (2015) and Müller (2016).

> Major parts of this chapter are based on the author's article Large-eddy simulation of cryogenic jet injection at supercritical pressures. In J. Bellan (Eds.) *High Pressure Flows for Propulsion Applications*, Progress in Astronautics and Aeronautics (under review).

3.1 Problem Description

We study the coaxial injection of hydrogen and nitrogen into a supercritical nitrogen atmosphere, which resembles conditions encountered in real rocket engines. By substituting oxygen with the inert gas nitrogen (with its fluid mechanical properties being not too different from oxygen), this setup allows for an isolated view on binary mixing processes near the injector without the influence of chemical reactions (Oschwald et al., 1999). The setup has been investigated experimentally by Oschwald et al. (1999) who performed a series of 2D-Raman density measurements with particular emphasis on atomization and mixing mechanisms. The chamber pressure is 4 MPa, thus, supercritical with respect to the critical pressures of pure nitrogen ($p_{c,N_2} = 3.34$ MPa) and pure hydrogen ($p_{c,H_2} = 1.29$ MPa). The measurement campaign covered experiments with and without the coaxial injection of hydrogen at several injection temperatures and velocities. To our knowledge, this is currently the only published experimental study on inert coaxial injection at LRE relevant conditions that obtained quantitative data with laser diagnostic methods. Data that have been obtained in a similar measurement campaign by Decker et al. (1998) have unfortunately never been published.

In the following, we will discuss LES results achieved for the operating conditions E4, which are summarized in Tab 3.1. Hydrogen (outer stream) and nitrogen (inner stream) are injected through a coaxial injector element into a cylindrical tank ($D = 10$ cm) filled with nitrogen at 4 MPa and 298.15 K. The inner and outer diameter of the hydrogen annulus are $D_{H_2,i} = 2.4$ mm and $D_{H_2,o} = 3.4$ mm, respectively; the inner nitrogen injector is $D_i = 1.9$ mm in diameter. A schematic of the experimental and optical setup is given in Fig. 3.1. The (ρ, T) diagram shown in Fig. 3.2 illustrates the nominal operating conditions for the main nitrogen injection. With a temperature of $T_{N_2} = 118$ K, nitrogen is initially in a compressed liquid state for operating point E4 ($\rho_{N_2} = 584.43$ kg/m^3). As seen from Fig. 3.2, the PR EOS, which will be used in the subsequent simulations yields a reasonably good approximation of the (pure) nitrogen inflow density with an error of about $\sim 4\%$ compared to the NIST reference data. The nominal bulk velocity of nitrogen is $\overline{u}_{N_2} = 5$ m/s and hydrogen is injected with a bulk velocity of $\overline{u}_{H_2} = 120$ m/s.

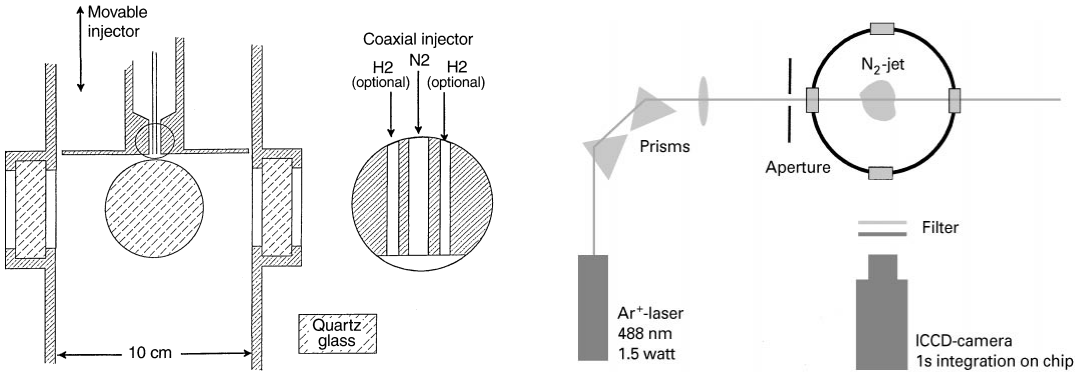

(a) Schematic of the experimental setup. **(b)** Schematic of the optical setup.

Figure 3.1: Schematic of the experimental and optical setup used in the campaign of Oschwald and Schik (1999). Reprinted with permission from Springer, Fig. 1 and Fig. 3, Copyright 2017, Springer-Verlag Berlin Heidelberg.

These velocities have been calculated from LN2 and GH2 mass flow rates, which were measured directly with a Coriolis mass flowmeter (private communication with Michael Oschwald).

Table 3.1: Test case definition. [a] Nominal experimental operating conditions according to Oschwald et al. (1999). [b] Calculated using NIST with nominal temperature and pressure. [c] Calculated using the PR EOS with nominal temperature and pressure. [d] Directly measured with a Coriolis mass flowmeter (private communication with Michael Oschwald). [e] Measured in the experiment on the jet centerline, cf. Fig. 3.5a and Fig. 12 in Oschwald et al. (1999). [f] Calculated from $\dot{m}_{N_2}$ and ρ_{N_2}. [g] Calculated from ρ_{N_2} and p using the PR EOS.

	p [MPa]	T_{N_2} [K] T_{H_2} [K]	$\overline{u}_{N_2}$ [m/s] $\overline{u}_{H_2}$ [m/s]	ρ_{N_2} [kg/m^3] ρ_{H_2} [kg/m^3]	$\dot{m}_{N_2}$ [g/s] $\dot{m}_{H_2}$ [g/s]
E4-T118	4[a]	118[a] 270[a]	5[a] 120[a]	584.43[b] / 608.78[c] 3.50[b]/ 3.55[c]	8.29[d]/8.63[c] 1.92[d]/1.94[c]
E4-T128	4[a]	128.274[c] 270[a]	7.49[f] 120[a]	390.18[e] 3.55[c]	8.29[d] 1.94[c]

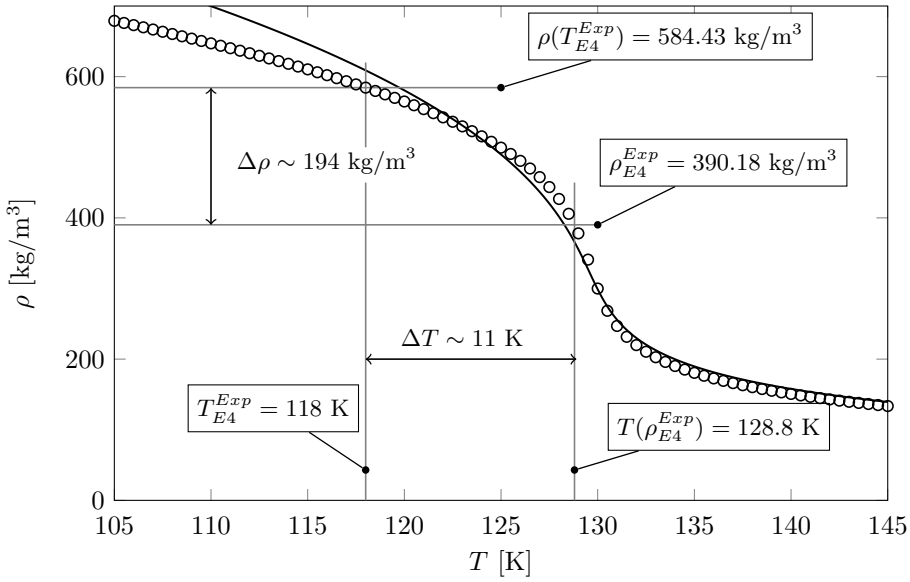

Figure 3.2: Thermodynamic conditions of the main nitrogen injection for test case E4-T118 and E4-T128 at 4 MPa. (——) PR EOS; ∘ Reference data is taken from the NIST (Lemmon et al., 2013)

3.2 Grid and Boundary Conditions

The computational domain is shown in Fig. 3.3. All simulations have been performed in a rectangular domain with the overall dimensions $L_x = 100$ mm in the streamwise and $L_y = L_z = 40$ mm in the lateral directions. Based on preliminary simulation results, a reasonably good estimate of jet break-up position and spreading angle was available to dimension the grid such that jet dynamics are not spuriously affected by the boundary conditions. An adaptive Cartesian blocking strategy with a static local refinement is used with a homogeneous grid resolution in the region of interest. The injector plane, 5 mm × 5 mm, is resolved with 16348 computational cells. Within a cone with a half opening angle of $\sim 11°$ and a length of 20 mm the grid has a homogeneous resolution in lateral and streamwise direction with $\Delta y_{min} = \Delta z_{min} = 0.0391$ mm and $\Delta x_{min} = 2\Delta y_{min}$. With increasing distance from the surface of the cone, grid coarsening in lateral and streamwise direction is applied. For the baseline grid $\mathcal{G}^2$, the total number of computational cells is about 16.9 million. Realistic turbulent inflow data for the LN2 pipe and GH2 annulus are generated through separate incompressible LES using cyclic boundary conditions in axial direction. Slices of the turbulent velocity fields are extracted from this simulation, accumulated in a database and interpolated onto the coarser

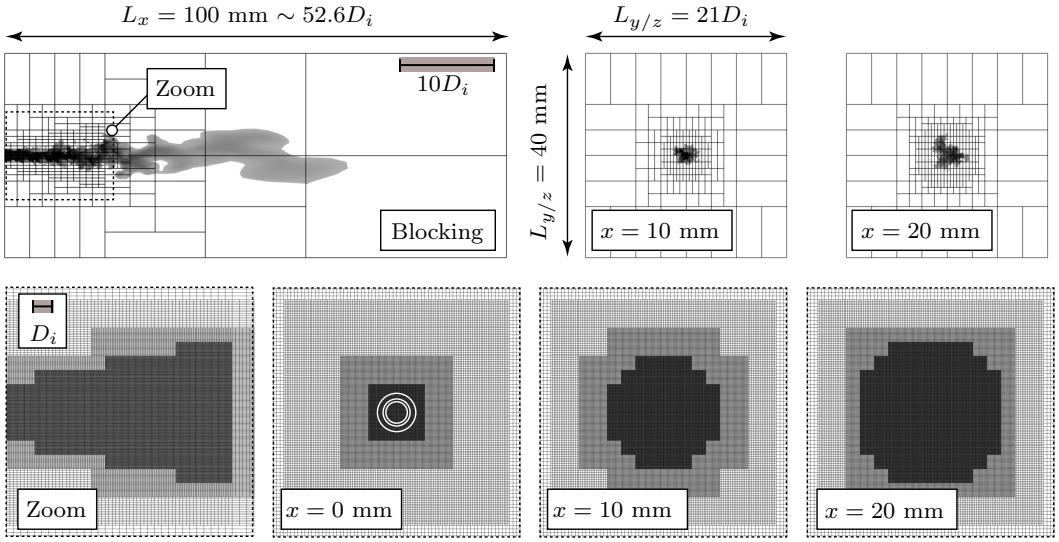

Figure 3.3: Blocking and grid resolution (baseline) of the computational domain for LES of LN2-GH2 coaxial injection.

grid of the final coaxial jet simulation. We also tested as inflow boundary condition a constant mean velocity profile with no fluctuations and with white noise with a turbulence intensity of 20%. As it turned out, jet evolution and break-up were insenstive to the level of turbulent fluctuation prescribed at the inlet. For the cases under consideration, the jet break-up is mainly controlled by shear forces induced by the annular co-flow. At the outlet, we prescribe the static pressure of 4 MPa together with a linear extrapolation procedure of all conservative flow variables. All walls are modeled as adiabatic.

3.3 LES with the Single-Phase Model

In the following section we present LES results with the assumed single-phase model which was introduced in Sec. 2.2. All simulations are performed with the fully-conservative set of governing equations, cf. Sec. 2.1, and with the baseline high-order numerical scheme, cf. Sec. 2.4.

3.3.1 Baseline Case E4-T118

Figure 3.4a depicts an instantaneous snapshot of the temperature distribution for case E4-T118 ($T_{N_2} = 118$ K). Contour levels are shown for 118 K $< T <$ 300 K, from dark to light shades, superimposed by a second group of contour levels with 110 K $< T <$ 118 K, from blue to red shades. Cryogenic nitrogen at 118 K can be identified as 'dark core', surrounded by a co-flow of warm hydrogen at 270 K. It is interesting to see that the temperature within in the mixing layer drops below its inflow value of 118 K with a minimum value of approximately 110 K. A related effect can be observed also for the hydrogen partial density ρ_{H_2}, which is depicted in Fig. 3.4b. Hydrogen is injected with a density of $\rho_{H_2} = 3.55$ kg/m^3 and reaches a much higher partial density of almost $\rho_{H_2} = 5.35$ kg/m^3 within the mixing layer.

In order to analyze changes in the thermodynamic state throughout the mixing process in greater depth, we show a scatter plot of temperature as function of hydrogen mole fraction z_{H_2} in Fig. 3.4c for the same dataset as used for Fig. 3.4a. On the left-hand side ($z_{H_2} = 0$), pure nitrogen at either 118 K (injection temperature) or 298.15 K (reservoir temperature) can be identified. On the right-hand side ($z_{H_2} = 1$), we observe pure hydrogen at 270 K. In between, either cryogenic nitrogen from the main injection (follow the line labeled 'adiabatic mixing temperature') or warm nitrogen from the reservoir (follow the straight line, top of the figure) is mixed with warm hydrogen. The line labeled 'adiabatic mixing temperature (T_F)' is calculated analytically as solution to the adiabatic mixing model, see Sec. 2.3.1 for details. This analytical model (which neglects the kinetic energy of the flow and the transport of heat and mass) shows, that the temperature decrease in the mixing layer can be attributed to real-gas mixing effects, i.e., non-linear interactions between molecules introduced via mixing rules, and not, as one could also assume, to heat transfer and diffusion mechanisms or to compressibility effects. The isobaric mixing of cryogenic nitrogen and warm hydrogen is endothermic. The scattered points in Fig. 3.4c are colored in gray-scale with the streamwise distance from the injector. We observe a fast mixing of the warm hydrogen with the warm atmospheric nitrogen such that for $x/D_i > 1.2$ no pure hydrogen ($z_{H_2} < 1$) is present in the chamber. Therefore, scatter away from the adiabatic mixing line can be attributed to mixing with the warm atmospheric nitrogen and transport phenomena (e.g., heat and mass diffusion) not covered by the model assumptions. In the scatter plot of Fig. 3.4c it is indicated that the LES data include thermodynamic mixture states that lie within the mixture two-phase region, although the operating pressure is well above the critical pressure of the pure components. This aspect is discussed separately in Sec. 3.4.

A corresponding scatter plot for the hydrogen partial density is shown in Fig. 3.4d.

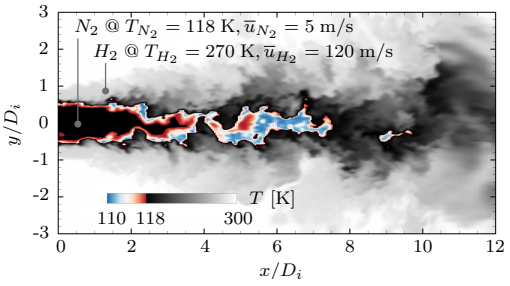

(a) Snapshot of the temperature field.

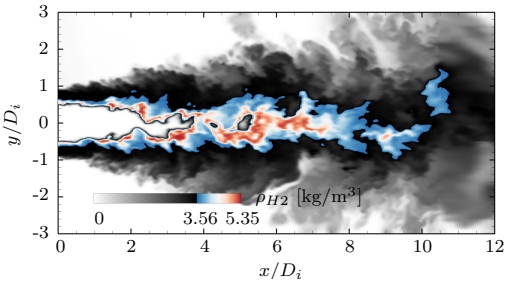

(b) Snapshot of the hydrogen partial density ($\rho_{H_2} = Y_{H_2} \cdot \rho$) field.

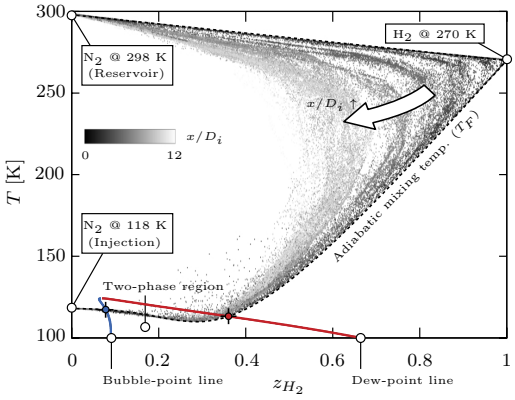

(c) Binary phase diagram together with the adiabatic mixing temperature. The scattered points, colored with the streamwise distance from the injector, depict the thermodynamic states that are obtained in the LES (instantaneous data, taken from Fig. 3.4a).

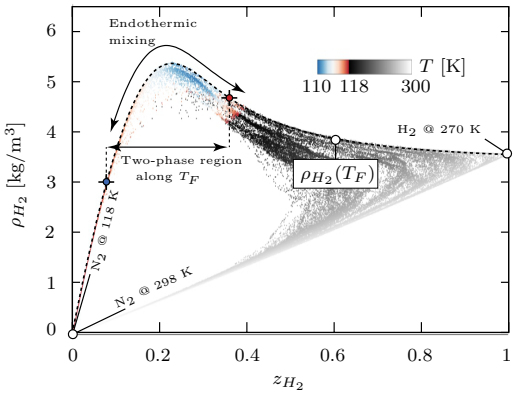

(d) Scatter plot of the hydrogen partial density ρ_{H_2}, colored with temperature T, as function of the hydrogen mole fraction z_{H_2}. The dashed line labeled $\rho_{H_2}(T_F)$ corresponds to the hydrogen partial density calculated along the adiabatic mixing line T_F.

Figure 3.4: Instantaneous contour and scatter plots for baseline case E4-T118 with the assumed single-phase model.

Again, there is pure nitrogen (meaning $\rho_{H_2} = 0$) on the left hand side and pure hydrogen at its corresponding density at injection $\rho_{H_2} = 3.55$ kg/m^3 on the right hand side. The scattered data is colored by temperature in the same way as done for Fig. 3.4a. The dashed line labeled $\rho_{H_2}(T_F)$ now corresponds to the hydrogen partial density ($\rho_{H_2} = Y_{H_2} \cdot \rho$) calculated along the adiabatic mixing line of Fig. 3.4c. The scattered data follow closely the analytical solution, and again, this result shows that, in the LES, the hydrogen partial density exceeds its pure component density due to real-fluid mixing effects. We note that the overall hydrogen partial density calculated along the adiabatic mixing line $\rho_{H_2}(T_F)$ as shown in

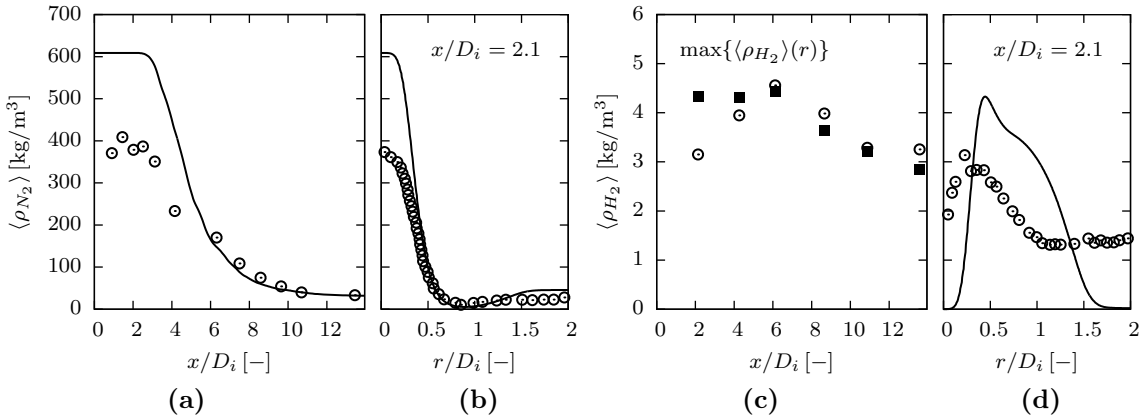

Figure 3.5: Axial (centerline) and radial nitrogen $\langle \rho_{N_2} \rangle$ and hydrogen $\langle \rho_{H_2} \rangle$ partial density profiles for test case E4-T118 with single-phase thermodynamics. (——) LES results; (⊙) experimental data of Oschwald et al. (1999). Radial profiles are extracted at 4 mm. Note that Fig. 3.5c displays the maximum values of the mean radial hydrogen density distribution $\max\{\langle \rho_{H_2} \rangle(r)\}$ as a function of the distance from the injector that have been recorded experimentally. (■) LES data at the corresponding streamwise locations.

Fig. 3.4d is not sensitive to meaningful values of the binary interaction parameter k'_{ij}.

In the following, we compare our numerical results with the experimental data of Oschwald et al. (1999). A total time interval of 20 ms has been simulated for all simulations, which corresponds to 5 flow through times (FTT) with respect to the nitrogen bulk velocity $\overline{u}_{N_2} = 5$ m/s and $L_x = 20$ mm. A fully developed flow field from coarser grids served as initial solution. Statistical properties have been obtained by averaging in circumferential direction and in time after an initial transient of 6 ms (1.5 FTT). Figures 3.5a and 3.5b depict the axial (centerline) and radial nitrogen density profiles for test case E4-T118. Radial data are extracted at $x/D_i = 2.1$. We observe significant differences in the potential core region ($x/D_i < 3$) with experimental and numerical nitrogen densities of ~ 390.18 kg/m^3 and ~ 608.78 kg/m^3, respectively. Recall Fig. 3.2: a specification of the inflow boundary condition in terms of temperature and pressure must yield a density within the potential core much higher than what is observed experimentally. With an error of about 4% when comparing the PR EOS to the NIST reference data, it becomes apparent that the observed differences in nitrogen density of approximately 200 kg/m^3 can not be attributed to an inaccurate equation of state (or the

simulation) but rather to measurement uncertainties. A more thorough discussion on this issue is given in Sec. 3.3.3.

Figures 3.5c and 3.5d show the corresponding hydrogen partial density profiles. Figure 3.5c displays the observed maximal values of the mean radial hydrogen density distribution $\max\{\langle\rho_{H_2}\rangle(r)\}$ at several stations. Oschwald et al. (1999) report an increase in hydrogen density downstream of the jet break-up that exceeds its pure-component value at injection, which is qualitatively reproduced by the numerical simulation. Quantitatively, we observe a very good agreement for $x/D_i > 6$. In the immediate vicinity of the injector, however, large deviations between measured and simulated hydrogen density are undeniably present.

3.3.2 Variation of the LN2 Temperature

Based on the observation that Oschwald et al. (1999) measured the density in the liquid core close to the injector as $\rho_{E4}^{Exp} \sim 390.18$ kg/m^3, which according to the NIST (Lemmon et al., 2013) indicates a nitrogen temperature of about 128.8 K rather then 118 K, we define a second test case E4-T128 for which we assume a correct density and mass flow rate measurement and an uncertain error of the temperature measurement. The mass flow rates of LN2 and GH2 were measured directly with a Coriolis mass flowmeter (private communication with Michael Oschwald). We thus obtain $\bar{u}_{N_2} = 7.49$ m/s for the nitrogen bulk velocity and $T_{N_2} = 128.274$ K for the inflow temperature (when using the PR EOS), see Tab. 3.1 and Fig. 3.2.

Snapshots of temperature and hydrogen partial density for test case E4-T128 are depicted in Fig. 3.6a and Fig. 3.6b, respectively. While we observe a similar effect for the temperature, i.e., a local decrease within the turbulent mixing layer, the hydrogen density does not exceed its pure component inflow value. The endothermic mixing does not necessarily imply hydrogen partial densities exceeding the inflow value. Figures 3.6c and 3.6d show the corresponding scatter plots. Again, the lines of adiabatic mixing temperature and partial density enclose the scattered data. Compared to the nominal operating conditions, thermodynamic peculiarities are less pronounced for test case E4-T128 due to the higher nitrogen temperature of $T_{N_2} = 128.274$ K.

A comparison to experimental measurements is provided in Fig. 3.7. For reference, data for case E4-T118 is also shown with gray lines and symbols. Centerline and radial nitrogen density profiles are shown in Figs. 3.7a and 3.7b. We now observe a very good agreement for the nitrogen density, the potential core length and the axial position for which a fully mixed state is obtained ($x/D_i \sim 10$). We note that

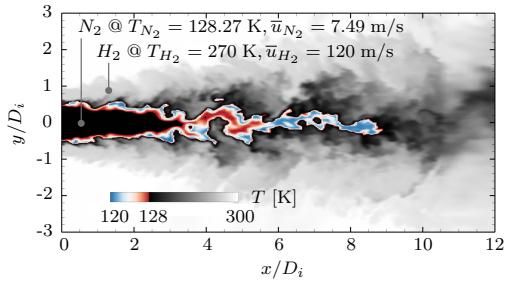

(a) Snapshot of the temperature field.

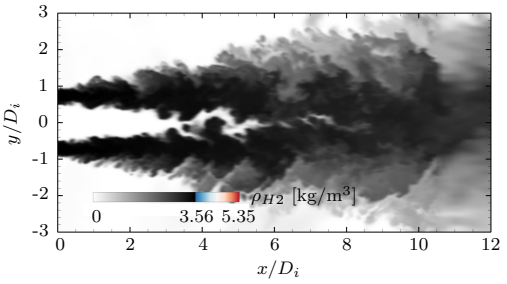

(b) Snapshot of the hydrogen partial density ($\rho_{H_2} = Y_{H_2} \cdot \rho$) field.

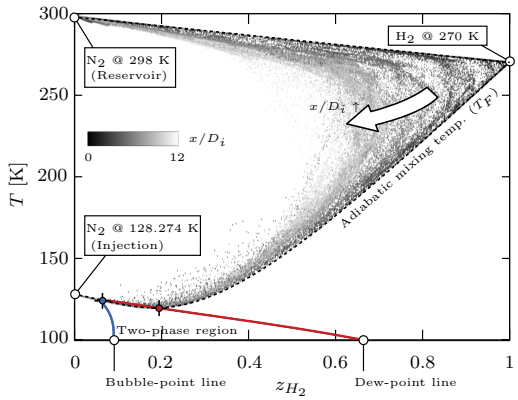

(c) Binary phase diagram together with the adiabatic mixing temperature. The scattered points, colored with the streamwise distance from the injector, depict the thermodynamic states that are obtained in the LES (instantaneous data, taken from Fig. 3.6a).

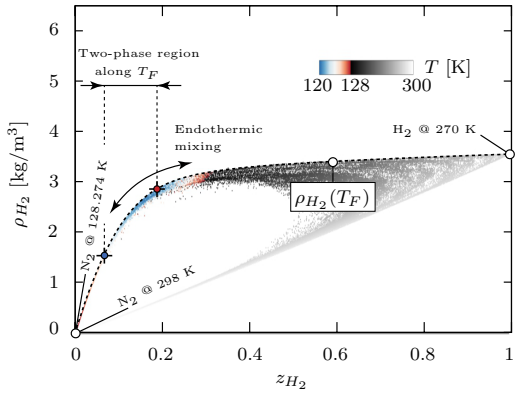

(d) Scatter plot of the hydrogen partial density ρ_{H_2}, colored with temperature T, as function of the hydrogen mole fraction z_{H_2}. The dashed line labeled $\rho_{H_2}(T_F)$ corresponds to the hydrogen partial density calculated along the adiabatic mixing line T_F.

Figure 3.6: Instantaneous contour {(a) & (b)} and scatter plots {(c) & (d)} for case E4-T128 with the assumed single-phase model.

the two latter observations may depend on the flow solver and grid resolution, see Sec. 3.3.4, whereas the value of the nitrogen density in the potential core does not. These results suggest that the nitrogen temperature at the injector exit could have been higher than the nominal value at the time of data collection. However, using the fitted boundary condition, we do not observe the characteristic increase in partial hydrogen density that was recorded experimentally, see Fig. 3.7c. As real-gas mixing effects are less pronounced at higher temperatures, this result was to be expected (cf. Figs. 3.6b and 3.6d). With respect to the hydrogen partial density, the agreement between experimental and numerical data is worse for the

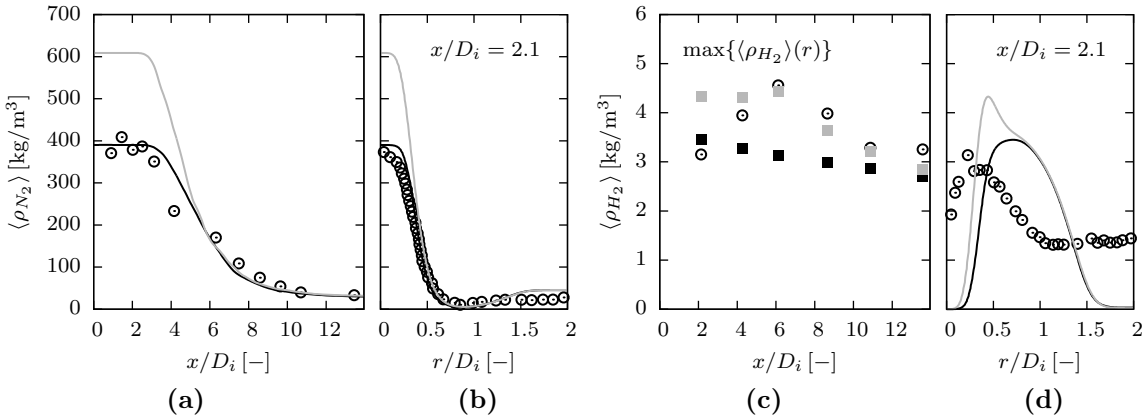

Figure 3.7: Axial (centerline) and radial nitrogen $\langle \rho_{N_2} \rangle$ and hydrogen $\langle \rho_{H_2} \rangle$ partial density profiles for test case E4-T128 with single-phase thermodynamics. (——) LES results; (⊙) experimental data of Oschwald et al. (1999). Radial profiles are extracted at 4 mm. Note that Fig. 3.7c displays the maximum values of the mean radial hydrogen density distribution $\max\{\langle \rho_{H_2} \rangle(r)\}$ as a function of the distance from the injector that have been recorded experimentally. (■) LES data at the corresponding streamwise locations. For reference, case E4-T118 is shown with gray lines and symbols, see also Fig. 3.5.

fitted boundary condition E4-T128, both quantitatively and qualitatively.

3.3.3 Assessment and Discussion

There are a number of uncertainties related to both the numerical and the experimental setup that may help to explain the observed differences: Laser diagnostics in turbulent flows in a high-pressure, low-temperature environment are very challenging. Oschwald et al. (1999) report difficulties in the quantification of the Raman signal due to refraction-index gradients and reflections at the injector face plate. These difficulties may increase the error bar especially at locations very close to the injector exit. The temperature measurement by thermocouples took place several diameters upstream of the nozzle exit. Although not explicitly mentioned in by Oschwald et al. (1999) and Oschwald and Schik (1999), we expect measurement uncertainties in the same order of magnitude as experienced in similar cryogenic nitrogen injection experiments, e.g., Mayer et al. (2003), Branam and Mayer (2003) and Davis and Chehroudi (2007). In addition, wall heat fluxes

within the injector, e.g., downstream of the temperature measurement, can lead to a non-homogeneous inflow temperature profile, which we do not account for in the LES. The important role of heat transfer in the injector prior to injection was addressed recently by Banuti and Hannemann (2016) in the context of experimental campaign of Mayer et al. (2003). For the present near critical operating conditions, the nitrogen density is very sensitive to temperature changes. Thus, uncertainties in the temperature measurement can have a significant impact on computational results when used as inflow boundary condition. The Raman signal was detected with a single-camera system. Depending on the bandpass filter that was used for the spectral separation of the Raman signals from different species, either nitrogen or hydrogen density measurements could be performed. According to Michael Oschwald, the measurements of the two species are therefore not temporally correlated and the same holds for measurements at different axial positions (private communication). We cannot exclude the possibility that the nitrogen temperature at the injector exit was approximately 128 K during nitrogen density measurements, which could explain the good agreement with respect to the nitrogen density for case E4-T128, while it had its nominal value of 118 K during hydrogen density measurements, which could explain the qualitative good agreement with respect to the exceeding hydrogen density for case E4-T118.

The last argument, however, must be handled with care. Recall Fig. 3.4c showing a temperature-composition diagram together with scattered LES data and the two-phase region (enclosed by dew-point and bubble-point line) for a binary hydrogen-nitrogen mixture at 4 MPa. We observe that some states obtained in the LES lie well within the two-phase region. Assuming the validity of classical thermodynamic fundamentals, in particular the two-phase theory with vapor-liquid equilibrium relations, the use of a single-phase model – as it was done in this paragraph – becomes questionable. Strictly speaking, there is no reason to believe that the single-phase PR EOS with the mixing- and combining rules introduced in Sec. 2.2 represents the true PVT behavior of this binary hydrogen-nitrogen mixture. This aspect will be addressed in Sec. 3.4.

3.3.4 Effect of Numerical Diffusion

In this section, we discuss results of grid convergence studies for the cases E4-T118 and E4-T128 using our baseline high-order numerical scheme as introduced in Sec. 2.4 (ALDM (Hickel et al., 2014) for velocity, pressure and kinetic energy and second-order TVD flux function for mass and internal energy advection, hereafter

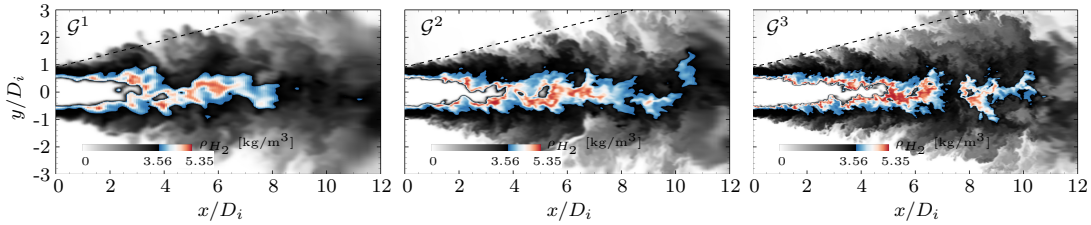

(a) Snapshots of hydrogen partial density distribution for case E4-T118.

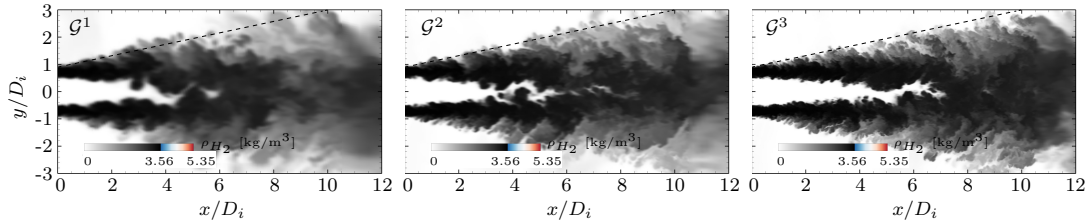

(b) Snapshots of hydrogen partial density distribution for case E4-T128.

Figure 3.8: Grid convergence study for the cases E4-T118 and E4-T128 with single-phase thermodynamics and the baseline numerical method SALD: Snapshots of hydrogen partial density distribution.

referred to as SALD) and for case E4-T118 with a more dissipative scheme (second-order upwind biased flux function for all governing equations, hereafter referred to as UW).

Grid Convergence Study with SALD

We uniformly refined ($\mathcal{G}^3$) and coarsened ($\mathcal{G}^1$) the base grid ($\mathcal{G}^2$) by a factor of 2 in all spatial directions (but only in the region of interest). For the highest ($\mathcal{G}^3$) and lowest ($\mathcal{G}^1$) grid resolution we obtain a total number of $\sim 3.8 \cdot 10^6$ and $\sim 101.5 \cdot 10^6$ computational cells, respectively. A single computation for 20 ms on the finest grid required about 3.1×10^6 CPU-hours. Figure 3.8a and 3.8b depict a contour plot of the instantaneous hydrogen partial density distribution at the different grid refinement levels for the cases E4-T118 and E4-T128, respectively. The qualitative comparison shows that with respect to thermodynamic phenomena all grid levels yield very similar results, however, we see that more fine-scale structure is added to the flow visualizations when the grid is refined and that the dense core becomes longer. A quantitative measurement of grid convergence is obtained from first order statistical moments such as mean density profiles and the integral property dark core length $L_C = x\{\langle\rho\rangle = 0.5(\rho_{in} + \rho_\infty)\}$. Figure 3.9 compares time-averaged nitrogen and hydrogen density profiles at different grid refinement levels to the ex-

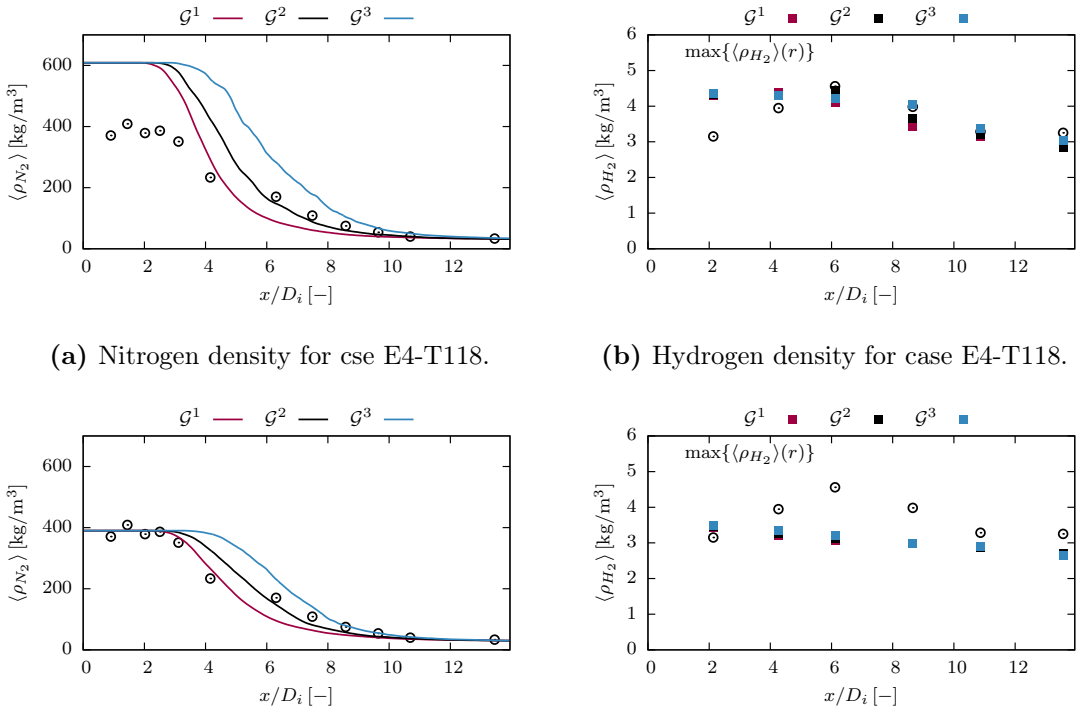

(a) Nitrogen density for cse E4-T118.

(b) Hydrogen density for case E4-T118.

(c) Nitrogen density for case E4-T128.

(d) Hydrogen density for case E4-T128.

Figure 3.9: Grid convergence study for the cases E4-T118 and E4-T128 with single-phase thermodynamics and the baseline numerical method SALD: Mean solution for nitrogen and hydrogen partial densities.

perimental data of Oschwald et al. (1999). We now see clearly with the centerline nitrogen partial density in Fig. 3.9a, case E4-T118, and 3.9c, case E4-T128, that the dense core becomes longer when the grid is refined. In addition, we cannot exclude the possibility that the location of jet break-up is pushed even further downstream on the next finer grid. We obtain $L_C = \{4D_i, 4.7D_i, 5.9D_i\}$ for case E4-T118 and $L_C = \{4.6D_i, 5.4D_i, 6.4D_i\}$ for case E4-T128. Note that the value of the nitrogen density in the dense core is of course not affected by grid resolution. Figures 3.9b and 3.9d show the corresponding hydrogen partial density plot for the cases E4-T118 and E4-T128, respectively. Again, to allow for a comparison to the data provided by the experimentalists, we must plot maximum values of the mean radial hydrogen density distribution $\max\{\rho_{H_2}(r)\}$ as a function of the distance from the injector. In this representation the hydrogen partial density is not as sensitive to the grid resolution as the nitrogen centerline density. Similar to the instantaneous snapshots we can conclude that with respect to character-

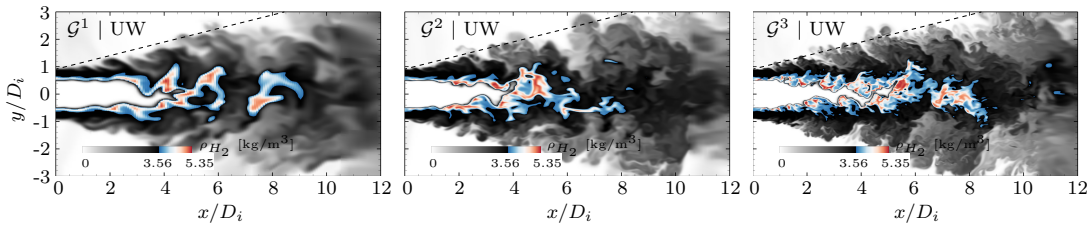

(a) Snapshots of hydrogen partial density distribution.

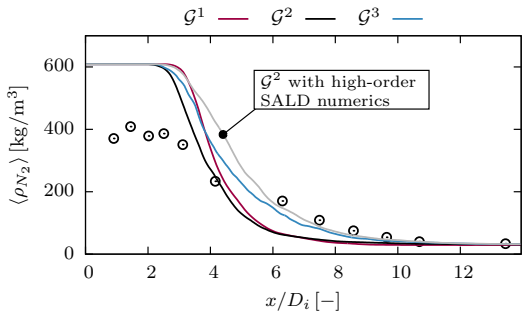

(b) Nitrogen partial density.

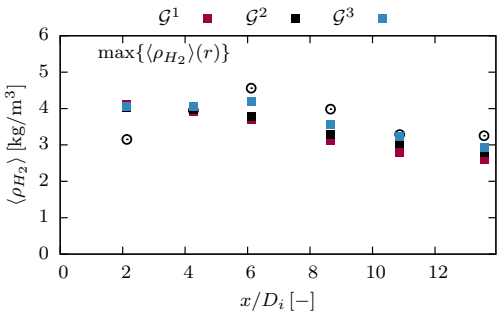

(c) Hydrogen partial density.

Figure 3.10: Grid convergence study for case E4-T118 using a more dissipative numerical scheme (second-order upwind biased flux function for all governing equations): Snapshots of hydrogen partial density distribution and mean solution for nitrogen and hydrogen partial densities.

istic thermodynamic phenomena, i.e., exceeding hydrogen density and matching nitrogen density in the dense core, all grid levels yield similar results. The overall quantitative agreement to experimental data does not get better or worse for any of the three grid resolutions. To obtain grid converged results, we tried run LES on the next finer grid $\mathcal{G}^4$, however, these LES would come at a computational expense that exceeds our current possibilities. A single computation of case E4-T118 on the next finer grid resolution with 662.9×10^6 cells would require about $\sim 38 \times 10^6$ CPUh computing time. Within the current scope of this work nothing essentially new can be learned from higher-resolution LES.

Grid Convergence Study with UW

Figure 3.10 shows results of a grid convergence study using a more dissipative scheme, i.e., second-order upwind biased flux function together with the van Albada limiter (van Albada et al., 1982) for all governing equations. As to be ex-

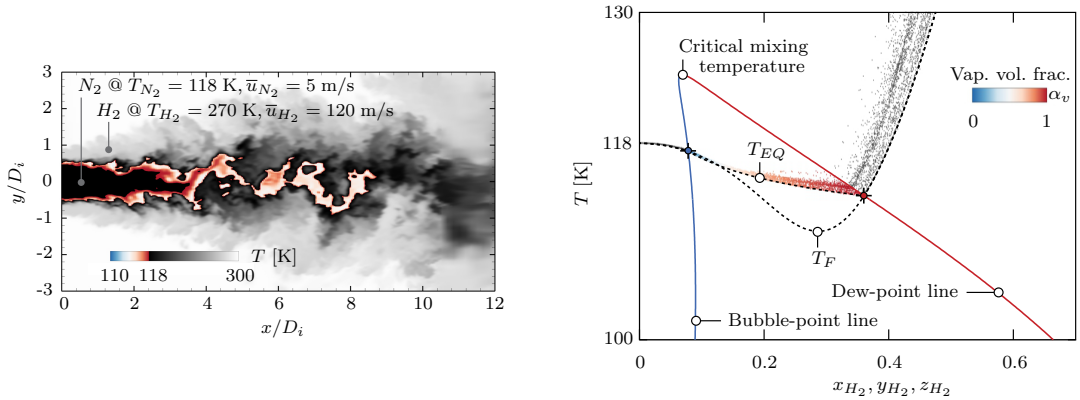

(a) Snapshot of the temperature field. Color map and range are the same as in Fig. 3.4a

(b) Binary phase diagram together with frozen T_F and equilibrium T_{EQ} adiabatic mixing temperature. Scattered points that are located within the two-phase region are colored from blue to red shades by the vapor volume fraction.

Figure 3.11: Instantaneous temperature contours (a) and scatter plot (b) for case E4-T118 with the two-phase model and SALD.

pected, the instantaneous flow fields shown in Fig. 3.10a appear more laminar-like compared the results shown in Fig. 3.8a. In Fig. 3.10b, we show time-averaged nitrogen density profiles at different grid refinement levels. Using a more dissipative scheme leads to a very different jet evolution and convergence rate. While we observed a monotonically increasing position of break-up/dark core length with increasing grid resolution for our high-order scheme SALD, the position of jet break-up is pushed upstream for $\mathcal{G}^1 \rightarrow \mathcal{G}^2$ and it is again moving downstream for $\mathcal{G}^2 \rightarrow \mathcal{G}^3$. Moreover, only for the highest grid resolution $\mathcal{G}^3$, we observe a fully mixed state at a similar axial position as with our higher-order scheme SALD, compare the gray line in Fig. 3.10b. It is noteworthy that such a non-monotonic convergence behavior can lead to a false conclusion whether or not LES results are grid converged. For this reason, results with the more dissipative scheme that have been published by our group in Müller et al. (2015) must be deemed non grid-converged. However, note that non-ideal thermodynamic phenomena like endothermic mixing or exceeding partial densities can be reproduced with any numerical scheme (and turbulence model) on any reasonably fine computational grid. Qualitative aspects discussed in Müller et al. (2015) remain therefore valid. Only when it comes to quantitative comparisons, e.g. jet break-up position, jet spreading angle or even higher order statistics such as velocity fluctuations, care needs to be taken.

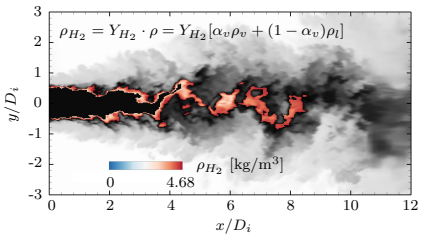

(a) Overall hydrogen partial density.

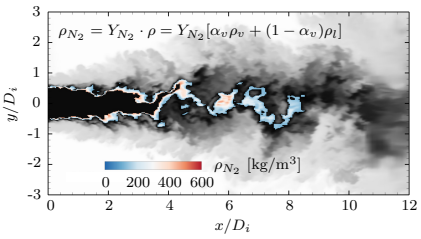

(b) Overall nitrogen partial density.

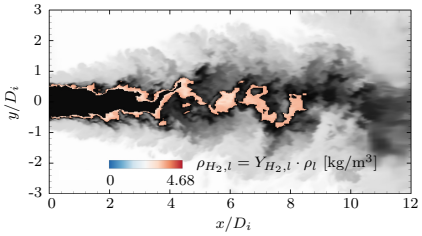

(c) Hydrogen partial density in the liquid phase.

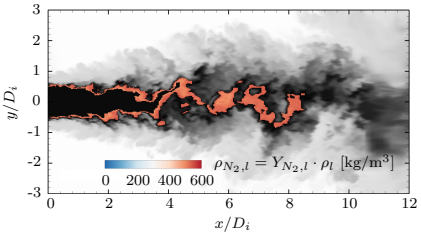

(d) Nitrogen partial density in the liquid phase.

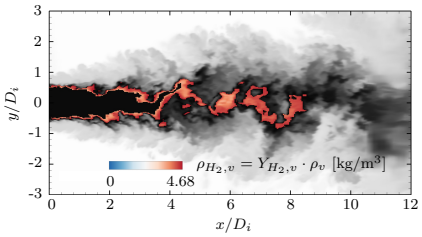

(e) Hydrogen partial density in the vapor phase.

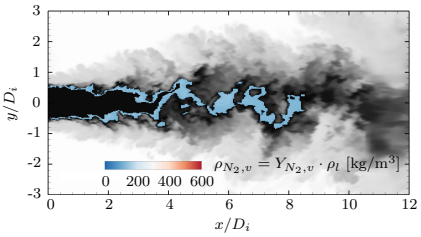

(f) Nitrogen partial density in the vapor phase.

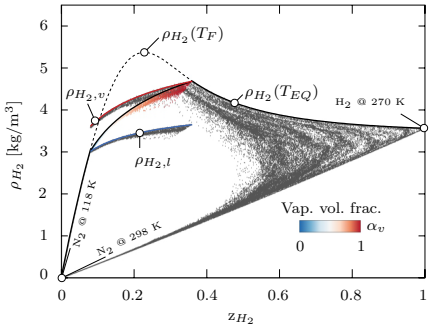

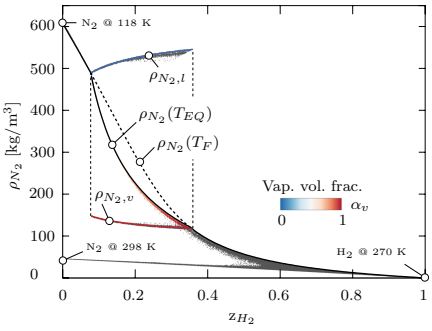

(g) Scatter plots of the hydrogen (left) and nitrogen (right) partial density as function of the hydrogen mole fraction. Scattered data located within the two-phase region are colored from blue to red shades with the vapor volume fraction. The black line labeled $\rho_i(T_{EQ})$ corresponds to the partial overall density of component i calculated along T_{EQ}, compare Fig. 3.11b. Solid red and blue lines represent vapor $\rho_{i,v}$ and liquid $\rho_{i,l}$ partial densities of component i.

Figure 3.12: Instantaneous contours in (a) - (f) and scatter plots (g) for case E4-T118 with the two-phase model and SALD.

3.4 LES with the Two-Phase Model

In the following section, we present results for LES of the nominal operating point E4-T118 using the two-phase model introduced in Sec. 2.3. LES is performed with the fully-conservative set of governing equations, cf. Sec. 2.1 and with the baseline high-order numerical scheme, see Sec. 2.4.

3.4.1 Flow Visualizations and Mean Flow

Figure 3.11a depicts a snapshot of the temperature field; color map and range are the same as in Fig. 3.4a. Taking phase separation into account leads to a less pronounced temperature decrease within the turbulent mixing layer yet the mixing process is still endothermic and the temperature drops by about 5 K. Figure 3.11b depicts the mixing process in mixture space. We also show bubble-point and dew-point line, which were calculated with the PR EOS for the nominal operating pressure of 4 MPa, see Sec. 2.3.1 for details. Again, scattered data depict the thermodynamic states that are obtained in the LES. Instantaneous data is taken from Fig. 3.11a and data points within the two-phase region are colored by the vapor volume fraction from blue to red shades. We also plot the adiabatic mixing temperature calculated with the single-phase assumption (T_F) and with the two-phase model (T_{EQ}), see Sec. 2.3.5 for details. Similar to the assumed single-phase simulations, LES data follow closely the equilibrium mixing temperature T_{EQ}. Scatter away from the adiabatic mixing line can be attributed to mixing with the warm atmospheric nitrogen and transport phenomena, e.g., heat and mass diffusion. Also note that not all points with $T < 118$ K are located within the two-phase region. With the vapor volume fraction $\alpha_v = 0$ at the bubble-point line and $\alpha_v = 1$ at the dew-point line, a smooth transition throughout the two-phase region is facilitated between a liquid-rich two-phase mixture on the nitrogen side and a vapor-rich two-phase mixture on the hydrogen side.

With partial densities being provided by the experimental campaign of Oschwald et al. (1999), the following paragraph focuses on analyzing them within the two-phase region. Figure 3.12a and 3.12b show contour plots of the overall hydrogen and nitrogen partial density

$$\rho_i = Y_i \rho = Y_i[\alpha_v \rho_v + (1 - \alpha_v)\rho_l], \tag{3.1}$$

where Y_i, ρ_v and ρ_l denote the overall mass fraction of component i, the vapor phase density and the liquid phase density, respectively. In the following, all cells

with $\alpha_v = 0$ and $\alpha_v = 1$ are blanked out to allow for an isolated view on regions with two-phase flow. The background contour shows the temperature field. Partial densities of component i in the liquid phase

$$\rho_{i,l} = Y_{i,l}\rho_l \quad \text{with} \quad Y_{i,l} = x_i \frac{M_i}{M_l} \quad \text{and} \quad M_l = \sum_{i=1}^{N_c} x_i M_i \tag{3.2}$$

are shown in Fig. 3.12c and Fig. 3.12d. Partial vapor phase densities

$$\rho_{i,v} = Y_{i,v}\rho_v \quad \text{with} \quad Y_{i,v} = y_i \frac{M_i}{M_v} \quad \text{and} \quad M_v = \sum_{i=1}^{N_c} y_i M_i \tag{3.3}$$

of each component are given in in Fig. 3.12e and Fig. 3.12f. $Y_{i,l}$ and $Y_{i,v}$ denote the mass fraction of component i in the liquid and vapor phase, respectively. M_v and M_l denote the molar mass of liquid and vapor phases, respectively. Corresponding scatter plots which include all aforementioned partial densities are depicted in Fig. 3.12g. The black line labeled $\rho_{H_2}(T_{EQ})$ and $\rho_{N_2}(T_{EQ})$ corresponds to the partial overall density of each component calculated along the equilibrium adiabatic mixing temperature line T_{EQ} (see Fig. 3.11b). The solid red and blue lines represent corresponding vapor $\rho_{i,v}$ and liquid $\rho_{i,l}$ phase densities of component i calculated from the analytical model. The partial density $\rho_i(T_F)$ calculated along the adiabatic mixing line with single-phase assumption is shown as reference with dashed lines.

There are a number of noteworthy aspects associated with Fig. 3.12: **1.** Liquid and vapor phase scatter follow closely the curves calculated from the analytical model. **2.** The overall partial density ρ_i of each component is bounded by its liquid and vapor phase partial densities, i.e. $\rho_{H2,l} \leq \rho_{H2} \leq \rho_{H2,v}$ and $\rho_{N2,v} \leq \rho_{N2} \leq \rho_{N2,l}$. **3.** As expected, the hydrogen partial density in the vapor phase $\rho_{H2,v}$ is higher than in the liquid phase $\rho_{H2,l}$. However, it is interesting to see that liquid and vapor phase partial densities are not too different from each other and that a noticeable amount of hydrogen is solved in the liquid phase. Note that hydrogen is injected in a gaseous state. **4.** In contrast, the nitrogen partial density in the liquid phase $\rho_{N2,l}$ is much higher compared to its density in the vapor phase $\rho_{N2,v}$, see Fig. 3.12d and 3.12f. This raises an interesting question: which partial density is actually being measured by Raman spectroscopy in case of phase separation within the turbulent shear layer and the existence of liquid and vapor phases with different partial densities? In view of a finite spatial resolution in the experiment (given by the measurement volume created by the laser and the camera system) we expect that the Raman signal recorded is spatially integrated, and depending on

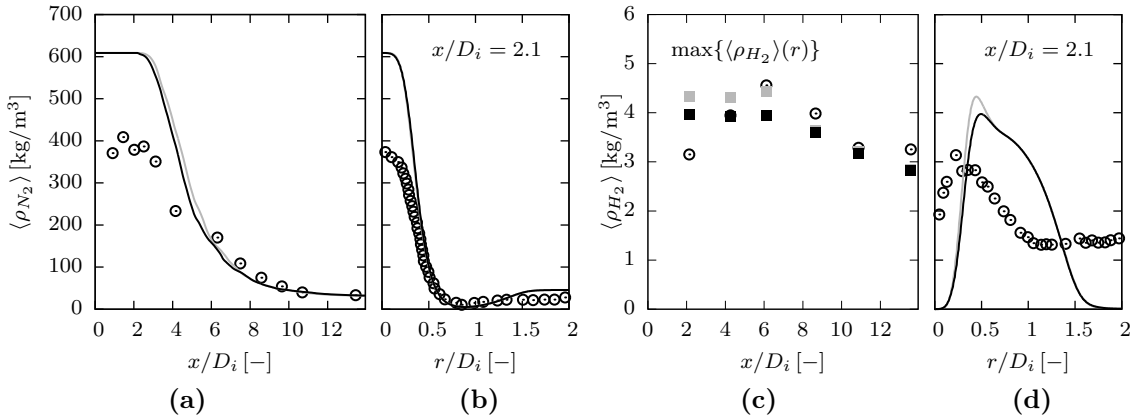

Figure 3.13: Axial (centerline) and radial nitrogen $\langle \rho_{N_2} \rangle$ and hydrogen $\langle \rho_{H_2} \rangle$ partial density profiles for test case E4-T118 with the two-phase model. (——) LES results; (⊙) experimental data of Oschwald et al. (1999). Radial profiles are extracted at 4 mm. Note that Fig. 3.7c displays the maximum values of the mean radial hydrogen density distribution $\max\{\langle \rho_{H_2} \rangle(r)\}$ as a function of the distance from the injector that have been recorded experimentally. (■) LES data at the corresponding streamwise locations. For reference, case E4-T118 with the single-phase model is shown with gray lines and symbols, see also Fig. 3.5.

the temporal resolution (e.g., pulsed laser as in Decker et al. (1998) or continuous-wave laser as in Oschwald et al. (1999)) integrated in time. Assuming a constant Raman cross section and the same Raman shift in both liquid and vapor phases for each component, the measured signal will represent an 'over all phases averaged' partial density. Whether or not the measured signal in the two-phase region can be compared with the overall partial density $\rho_i = Y_i \rho = Y_i[\alpha_v \rho_v + (1 - \alpha_v)\rho_l]$ of component i in the homogeneous mixture approach, compare Fig. 3.12a and Fig. 3.12b, is an interesting objective for future studies. Raman spectroscopy in two-phase flows, however, is not a straightforward task. Woodward and Talley (1996), Decker et al. (1998) and Oschwald and Schik (1999) name many challenges that complicate the Raman signal quantification: the laser beam/sheet can scatter strongly in an elastic way at sharp phase interfaces (which will lead to a loss of the Raman signal on the laser exit side); local focusing at interfaces can cause laser-induced optical breakdown (plasma formation) or stimulated Raman scattering, which does no longer scale linearly with the species number density. In view of these difficulties we believe that complementary high-fidelity numerical simulations

with the presented two-phase model will prove useful for the interpretation of experimental findings, e.g., to identify regions where in the flow field the mixture becomes locally subcritical and only two phases can coexist.

In the following, we compare our numerical results with the experimental data of Oschwald et al. (1999) and with the single-phase LES results. Statistical properties have been obtained in the same manner as for the single-phase simulations. Figure 3.13a and 3.13b depict the axial (centerline) and radial nitrogen density profiles for test case E4-T118. For reference, data with the single-phase model is shown with gray lines and symbols. Similar to the data previously discussed we observe large differences between experimental and numerical data in the injector near field. This result was to be expected since the two-phase model does of course not alter the PVT behavior of the pure components. The differences in the (overall) density prediction between the two models have a notable but small effect on the jet break-up position, in fact less than we expected beforehand. At lower LN2 (and GH2) injection temperatures, however, the situation will change with larger parts in mixture space being located within the two-phase region. Figure 3.13c and 3.13d show the corresponding hydrogen partial density profiles. Again, Figure 3.5c displays the observed maximal values of the mean radial hydrogen density distribution $\max\{\langle\rho_{H_2}\rangle(r)\}$ at several stations. Similar to the single-phase results (gray symbols), we can reproduce qualitatively the exceeding hydrogen partial density. In the near field of the injector ($x < D_i < 7$), the observed values are lower compared with the assumed single-phase results. Quantitatively, a good agreement is observed only for $x/D_i > 6$ (similar to the assumed single-phase result). In the immediate vicinity of the injector, however, the agreement between experiment and LES does not improve when using the more sophisticated two-phase model. Here, thermodynamic non-equilibrium effects, which we do not account for in the LES, may become important. On the other hand, the spatial extent of regions with increased hydrogen densities is very narrow close to the injector. The detection of these regions may therefore be more difficult in an experiment.

3.4.2 Accuracy of the Two-Phase Model

We have seen that the increasing hydrogen partial density in streamwise direction is a very characteristic property of the experiment. With the help of the adiabatic mixing model we also showed that this increase is caused by real-gas mixing effects and that two-phase phenomena can occur within the turbulent shear layer. So far, we have not addressed the accuracy of the two-phase model with respect to VLE calculations and whether or not the true PVT behavior of the binary mixture

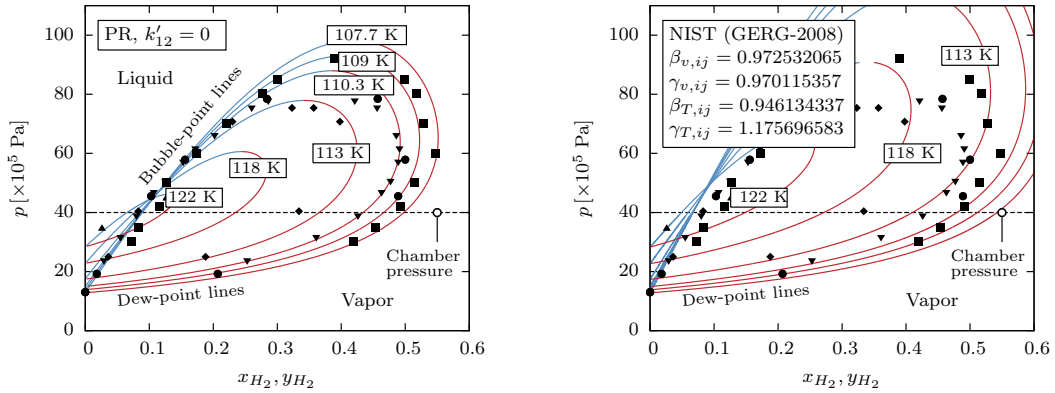

(a) Peng-Robinson equation of state.

(b) NIST REFPROP 9.1 (GERG-2008 equation of state).

Figure 3.14: Pressure-composition phase diagram for a binary hydrogen-nitrogen mixture. Experimental data was provided by DDBST GmbH (2015): (■) $T = 107.7$ K (Shtekkel and Tsinn, 1939); (●) $T = 109.0$ K (Gonikberg et al., 1939a,b); (▼) $T = 110.3$ K (Streett and Calado, 1978); (♦) $T = 113.0$ K (Shtekkel and Tsinn, 1939); (▲) $T = 122.04$ K (Eubanks, 1957). Bubble-point and dew-point lines are calculated with the PR EOS. Mixing and combining rules as introduced in Sec. 2.2 with no adjustment of the pseudocritical properties ($k'_{12} = 0$) are used.

is represented. A comparison with experimental VLE data and an analysis of hydrogen partial densities along the adiabatic mixing line will help to estimate uncertainties associated with our thermodynamic model.

Figure 3.14a shows the pressure-composition phase diagram calculated with the PR EOS. The binary interaction parameter k'_{12} was set to zero as in the LES. For pressures relevant to the present application (4 MPa, dashed horizontal line in Fig. 3.14a), we observe a reasonably good agreement of the VLE predicted with the PR EOS and available experimental data (for references see the caption in Fig. 3.14). It should be noted, however, that without adjustment of the binary interaction parameter the accuracy deteriorates rapidly for higher pressures ($p > 6$ MPa). Typically, binary interaction parameters for cubic EOS are regressed using available experimental VLE or PVT data or, alternatively, more sophisticated reference EOS. Figure 3.14b shows the pressure-composition phase diagram calculated with NIST REFPROP 9.1, which uses for binary nitrogen-hydrogen

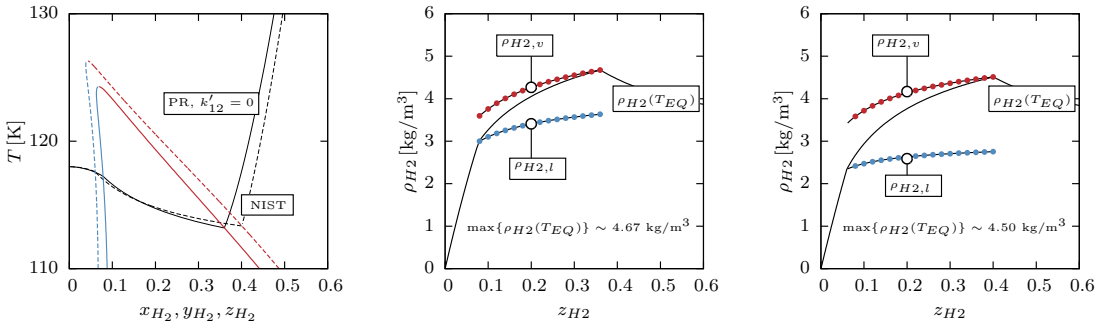

(a) Temperature composition diagram.

(b) PR EOS.

(c) GERG-2008 EOS

Figure 3.15: (a) Temperature-composition phase diagram for a binary hydrogen-nitrogen mixture calculated with the PR EOS and with NIST REFPROP 9.1 (GERG-2008 EOS). (b) & (c) Hydrogen partial density as function of the hydrogen mole fraction. The black line labeled $\rho_{H2}(T_{EQ})$ corresponds to the partial overall density of hydrogen calculated along T_{EQ}, compare Fig. 3.15a. Solid red and blue lines represent vapor $\rho_{H2,v}$ and liquid $\rho_{H2,l}$ partial densities.

mixtures as default setting the GERG-2008 EOS (Kunz and Wagner, 2012). The default binary mixture parameters (see Fig. 3.14b) have been used in the GERG-2008 EOS and it is interesting to see that the more sophisticated EOS does not accurately predict the VLE[1]. Mixtures with large amounts of hydrogen at cryogenic temperatures were not the main focus in the development of the GERG-2008 EOS. The present application is therefore beyond the range of validity when using the default mixture parameters. This serves as a very good example that the thermodynamic model employed for LES of cryogenic flows needs to be checked carefully against available experimental data. Figure 3.15a shows the corresponding temperature composition diagram at 4 MPa together with the adiabatic mixing line calculated with both the PR EOS and the GERG-2008 EOS[2]. The two-phase region at 4 MPa calculated with the GERG-2008 EOS is only slightly larger compared to the PR EOS (which can also be seen in Fig. 3.14) and also the two adiabatic mixing lines differ not too much (note the zoomed view). Figure 3.15b and 3.15c show hydrogen partial densities calculated along their corresponding mixing line.

[1]REFPROP 9.1 issues a warning that the default mixing parameters should not be used at cryogenic temperatures for binary nitrogen-hydrogen mixtures.

[2]A FORTRAN script which calls REFPROP core routines (PHFLSH, TPFLSH, TPFL2, ENTHAL) calculates the adiabatic mixing line with the GERG-2008 EOS.

For reasons of clarity, the lines are not shown in a single figure. Compared to the PR EOS, the GERG-2008 EOS predicts smaller molar compositions of hydrogen in the liquid phase, see Fig. 3.15a, which seems to translate into a smaller liquid phase hydrogen partial density $\rho_{H2,l}$. The overall hydrogen density distribution, however, and especially the maximum value of ρ_{H2}, do not differ a lot between both EOS. Given the fact that we obtain very similar hydrogen partial density distributions for very different EOS (and one of which compares reasonably good to experimental VLE data) gives confidence that the PVT behavior of nitrogen-hydrogen mixtures is well represented by our thermodynamic model based on the PR EOS used for LES of case E4.

3.5 Summary

In this chapter we studied the shear coaxial injection of liquid nitrogen and gaseous hydrogen with a particular emphasis on two-phase phenomena under high-pressure conditions. We selected an operating point from the series of experiments of Oschwald et al. (1999) for which quantitative density measurements are available. LES results with the (assumed) single-phase model showed interesting thermodynamic phenomena such as endothermic mixing and partial hydrogen densities exceeding the inflow value within the turbulent shear layer. The latter was recorded also experimentally for the nominal operating conditions. The adiabatic mixing model showed that both the temperature decrease and exceeding hydrogen partial densities in the mixing layer can be attributed to real-gas mixing effects, i.e., non-linear interaction between molecules introduced via mixing rules, and not, as one could also assume, to heat transfer and diffusion mechanisms or compressibility effects. We further identified the inflow temperature of the main nitrogen injection as crucial for the reproduction of the experimental results. Based on the observation that the nominal inflow conditions for temperature and pressure must yield a nitrogen density in the jet core much higher than what was measured experimentally, we defined a new test case for which we assumed a correct density and mass flow rate measurement and an uncertain error of the temperature. For this fitted boundary condition, we observed quantitatively a very good agreement between experimental and numerical data with respect to the nitrogen density. However, experimental findings of exceeding hydrogen partial densities were not reproduced anymore because of real-gas mixing effects being less pronounced at higher nitrogen injection temperatures.

By analyzing VLE data, we found that some states obtained in the LES lie well

within the two-phase region. We therefore performed LES also with the more sophisticated two-phase model. While we observed hydrogen partial densities in the liquid and vapor phase not too different from each other, the partial density of nitrogen showed considerable differences in the two phases. This raised the interesting question which density was actually measured by Raman spectroscopy in case of potential two-phase flow. Given the fact that the quantitative agreement between LES and experimental density measurements did not improve when using the two-phase model, we addressed the question how precise the employed thermodynamic model actually is. A validation against experimental data showed that the PR EOS without adjustment of the binary interaction parameter gives reliable VLE predictions at pressures relevant to this application. A comparison of partial densities to another EOS model gave confidence that the PVT behavior of the nitrogen-hydrogen mixtures is well represented by the employed thermodynamic model.

In addition, we addressed the effect of numerical diffusion by means of a grid convergence study and the application of a more dissipative numerical scheme for baseline case E4-T118. Grid resolution had a significant effect on integral properties such as the jet break-up position. Even for the highest grid resolution we were note able to demonstrate grid convergence for centerline density profiles. However, characteristic thermodynamic phenomena, such as exceeding hydrogen partial densities, were very similar on all grid levels.

Chapter 4

ECN Spray A

In this chapter, we will discuss LES results for the Spray A benchmark case and three additional operating points of the Engine Combustion Network (ECN, `http://www.sandia.gov/ecn/`). In contrast to the LN2-GH2 coaxial injection case we previously studied, we were not able to simulate Spray A with the single-phase thermodynamic closure together with the conservative set of governing equations for which we observed unphysical states in the flow field causing numerical instability. A direct comparison between single-phase model (F) and two-phase model (EQ) is therefore not possible for LES of Spray A. Instead, we will address well-known numerical challenges of trans- and supercritical fluid mixing and compare a fully conservative (FC) formulation to a quasi-conservative (QC) formulation of the governing equations. Our results will prove physical and numerical consistency of both methods on fine grids and demonstrate the effects of energy conservation errors associated with the quasi-conservative formulation on typical LES grids.

> Major parts of this chapter are based on the author's article Matheis and Hickel (2018). [Multi-component vapor-liquid equilibrium model for LES of high-pressure fuel injection and application to ECN Spray A. *International Journal of Multiphase Flow*, **99**, 294–311].

4.1 Problem Description

The ECN is an international group of institutions – both from academia and industry – whose aim is to study reacting and non-reacting sprays to improve our understanding of mixing and combustion at engine-relevant conditions. A key activity of the ECN is to investigate sprays under high-temperature, high-pressure conditions typical of diesel combustion. In this context, the so-called *Spray A* target condition have received considerable attention in the community. Liquid n-dodecane ($C_{12}H_{26}$) at nominal 363 K is injected from a common rail injector through a single-orifice nozzle with a diameter of 0.09 mm into an atmosphere with nominal 900 K and 22.8 kg/m^3 ambient gas temperature and density, respectively. Extensive data sets are available for Spray A, including parametric variations for ambient temperature, density, oxygen concentration, and injection pressures, see, for instance, Pickett et al. (2011b), Meijer et al. (2012), Payri et al. (2012), Manin et al. (2012) and Manin et al. (2016). Depending on the laboratory, either constant-pressure flow chambers or constant-volume preburn (CVP) chambers are used to provide high-temperature, high-pressure gases that match the Spray A target conditions. The former chamber is capable to simulate the thermodynamic conditions obtained in a diesel engine under steady conditions with its key components being compressors, heaters and a control system. In the latter concept, ambient pressure and temperature at the time of injection are provided by igniting a premixed gas mixture that burns to completion. See, e.g., Meijer et al. (2012), for a more detailed description of both approaches. In this work, LES data are compared to experimental data from Sandia National Laboratories (`http://www.sandia.gov/`) where a CVP chamber was used. Because of the working-principle of CVP chambers, the atmosphere in the experiment for non-reacting spray studies is composed of 89.71% nitrogen, 6.52% carbon-dioxide and 3.77% water (percentage on a molar basis)[1]. To keep computational costs at

[1] See under the following link for further details on the composition of the atmosphere: `https://ecn.sandia.gov/diesel-spray-combustion/sandia-cv/ambient-conditions/`

a minimum and to simplify the multi-component system, we assume that the atmosphere in the LES is composed only of nitrogen. Furthermore, idealized initial conditions are chosen meaning that gradients or fluctuations in temperature or velocity are not considered.

The remainder of this chapter proceeds as follows: First, a validation of the PR EOS in comparison to experimental VLE data together with an analytical evaluation of the thermodynamic models is presented in Section 4.2. Consistency and convergence of the FC and QC discretization of the governing equations is proved in Section 4.3 for a 1-D test case at thermodynamic conditions similar to Spray A. Results for LES of Spray A and the parametric variation of test conditions will be discussed in Section 4.4 and Section 4.5, respectively. The chapter will end in Section 4.6 with a discussion and outlook.

4.2 Thermodynamic Analysis

Let us first address briefly the accuracy of vapor-liquid equilibria calculated with the PR EOS and the mixing and combining rules introduced in Sec. 2.2.1 for conditions relevant to Spray A. Figure 4.1(a) shows the pressure-composition phase diagram. The calculation of bubble-point and dew-point lines is described in Sec. 2.3.1. The nominal Spray A operating pressure of 6 MPa is shown by the dashed horizontal line and six bubble-point and dew-point lines are plotted for $344.4\text{K} \leq T \leq 593.5\text{K}$. At such high pressures and relevant temperatures a significant amount of the ambient gas, i.e., nitrogen, is dissolved in the fuel-rich liquid phase. While we observe a good prediction of the nitrogen mole fraction in the vapor phase (red curves), its liquid phase composition (blue curves) is overestimated in comparison to available experimental data. It is possible to improve the prediction for the nitrogen absorption into the liquid phase by re-calibrating the binary interaction parameter for the PR EOS, see, e.g., Balaji et al. (2011) and Qiu and Reitz (2015).

In the previous Chapter we have seen that LES data follow closely the frozen (T_F, single-phase model) and equilibrium (T_{EQ}, two-phase model) adiabatic mixing temperature. The same observation holds for LES of Spray A, as it will be discussed in detail in Section 4.4.3. An analysis of the adiabatic mixing model can hence give an impression of the PVT relation seen by the CFD solver. Figure 4.1(b) shows the temperature-composition phase diagram for the nominal operating pressure of 6 MPa. Bubble-point and dew-point line enclose the two-phase

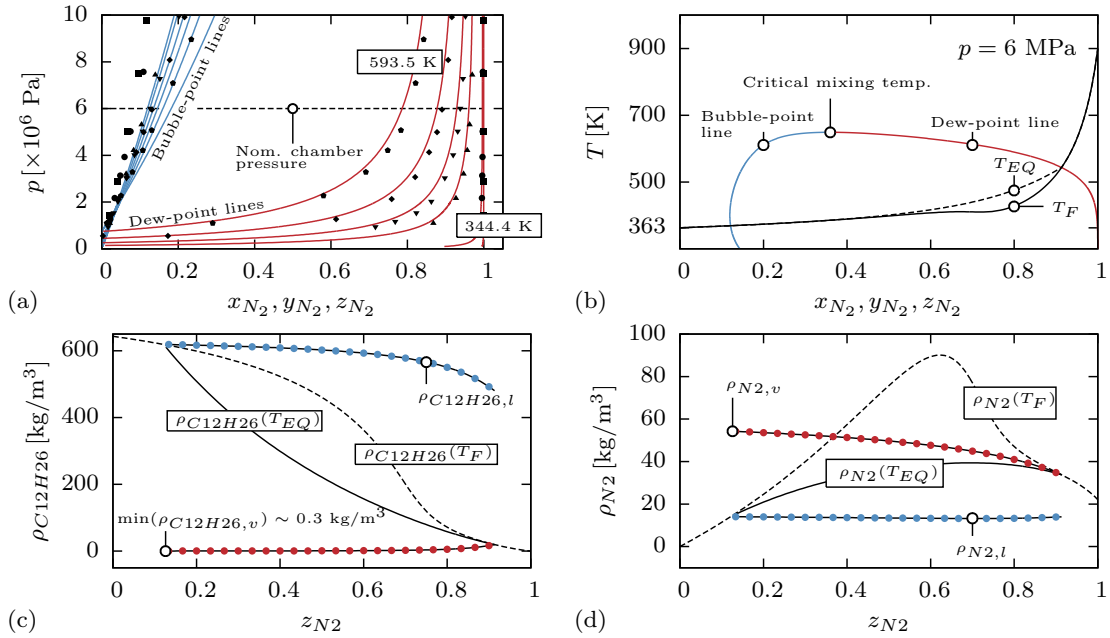

Figure 4.1: (a) Pressure-composition phase diagram. Experimental data was provided by DDBST GmbH (2015). (b) Temperature-composition phase diagram at 6 MPa together with frozen (T_F) and equilibrium (T_{EQ}) mixing temperature. Dodecane (c) and nitrogen (d) partial overall densities (ρ_i) and partial liquid ($\rho_{i,l}$) and vapor ($\rho_{i,v}$) densities along frozen (T_F) and equilibrium (T_{EQ}) mixing temperature. A MATLAB source code (`main_N2_C12H26.m`) which produces the figures (b)-(d) is provided as supplementary material, see Appendix B.

region. The solid and dashed line correspond to the frozen (labeled T_F) and equilibrium (labeled T_{EQ}) adiabatic mixing temperature, respectively. For details on the calculation see Sec. 2.3.1. Single-phase and two-phase model do of course collapse outside of the two-phase region. For mixture states located within the two-region, we see differences in temperature of about $\sim$ 48 K at a molar composition $z_{N2} \sim 0.8$ (which is about 11% with reference to T_F) between the two models.

Figures 4.1(c,d) depict the partial overall densities (ρ_i) of component i along the frozen and equilibrium mixing temperatures T_F and T_{EQ}. We also show partial densities in the liquid ($\rho_{i,l}$ - blue points) and vapor ($\rho_{i,v}$ - red points) phase. Taking phase separation into account significantly alters the overall PVT relation within the two-phase region ($z_{N2} \sim 0.12 - 0.91$). For example, for an overall nitrogen mole fraction $z_{N2} \sim 0.49$ the overall n-dodecane density $\rho_{C12H26}(T_{EQ})$ is about

240 kg/m^3 below the density as predicted by the PR EOS in the single-phase approach (which is about 50% with reference to ρ_F). Note that the temperature difference between frozen and equilibrium approach is here ($z_{N2} \sim 0.49$) negligible. It appears that differences in the density prediction are much more severe compared to the temperature difference between the two thermodynamic closures. The liquid phase nitrogen density $\rho_{N2,l}$ in Fig. 4.1(d) gives an impression on the solubility of nitrogen in the liquid phase, where we see a more or less constant value of about 14 kg/m^3. It is also interesting to note that the nitrogen partial density in the vapor phase (and overall nitrogen partial density for $z_{N2} > 0.20$) exceeds its pure component/atmospheric value ($\sim$ 22 kg/m^3) up to a factor of $\sim$ 2.45 due to the endothermic process of evaporation and mixing with the fuel vapor (nitrogen is essentially cooled down).

4.3 Consistency of FC & QC Methods

In Chapter 2 a QC set of the governing equations based on a pressure-evolution equation was introduced. This was motivated by the fact that FC formulations together with a nonlinear real-gas EOS can lead to spurious, unphysical pressure oscillations in the flow field (Terashima and Koshi, 2012, 2015). Before comparing LES results for Spray A obtained with the FC and QC set of governing equations, it is important to demonstrate that both methods are consistently implemented in the CFD solver. Furthermore, Eqs. (2.1)-(2.4) (FC) and Eqs. (2.1)-(2.3),(2.5) (QC) are expected to converge to the same solution with increasing grid resolution. To prove this important hypothesis, we show results for a 1-D advection-diffusion test case of a contact discontinuity in Fig. 4.2. The number of uniform cells in the region of interest ($-l_{ref}/2 < x < l_{ref}/2$) with $l_{ref} = 2 \times 10^{-5}$ m varies from 32 to 2048. Two very large blocks with stretched cells are attached on both sides, such that reflections from the boundary conditions cannot affect the results.

The chosen thermodynamic conditions are similar to Spray A ($p = 6$ MPa, $T_{N2} =$ 900 K, $T_{C12H26} = 363$ K) and the advection velocity is $u = 5$ m/s. Species mass fractions are initialized with an error function profile in physical space

$$Y_{C12H26} = 0.5 - 0.5 \, \mathrm{erf}[(x_i + 0.25 l_{ref})/(0.01 l_{ref})], \tag{4.1}$$

with x_i being the cell-center coordinates. Both FC and QC equations are closed by the single-phase model (the abbreviation F is used to indicated the use of the single-phase model), see Sec. 2.2 for details on the thermodynamic closure. The temperature across the initial interface is computed from a linear enthalpy

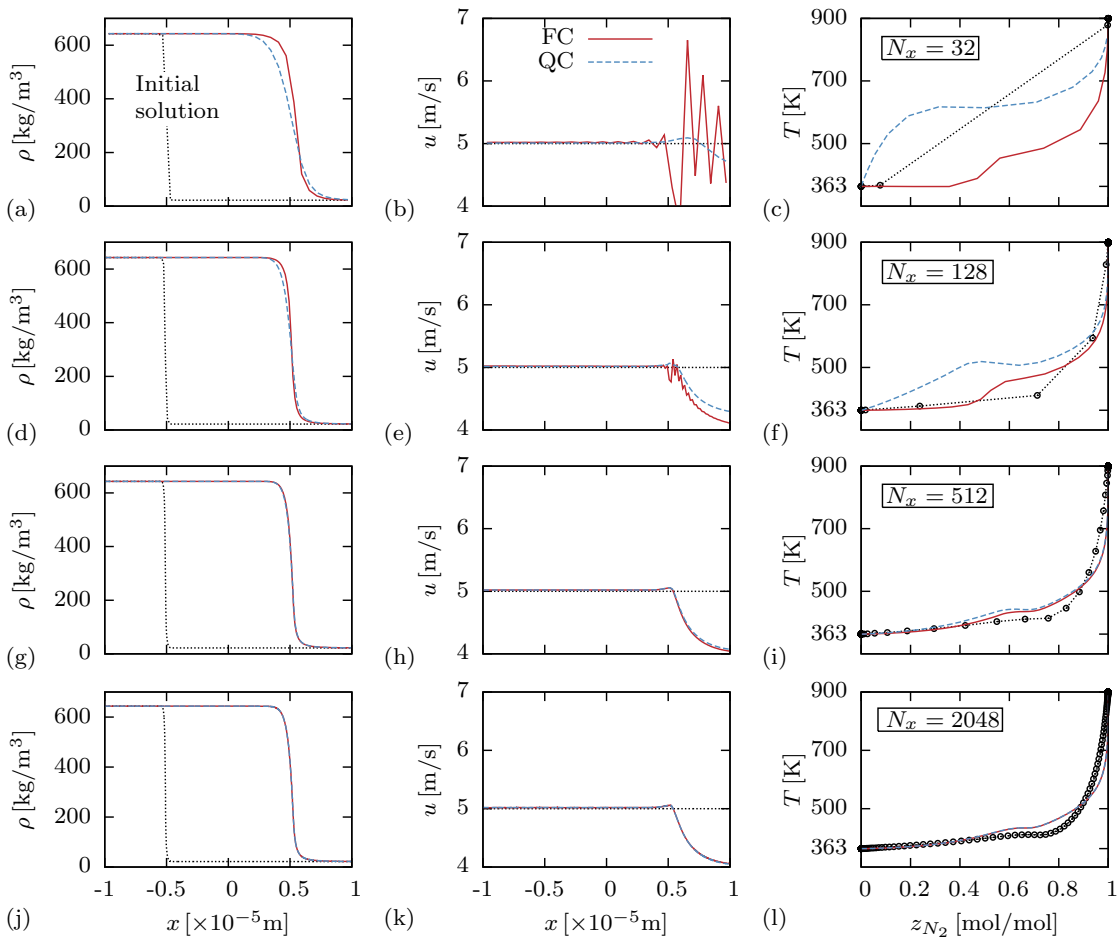

Figure 4.2: FC-F and QC-F results for a 1-D advection-diffusion test case with $u = 5$ m/s for different grid resolutions. Solution time is $t = 2 \times 10^{-6}$ s. Left column: density profiles in physical space; center column: velocity profiles in physical space; right column: temperature profiles in mixture space; dotted lines are the initial profiles.

profile in mixture space, i.e., the adiabatic mixing temperature. The first and second columns in Fig. 4.2 depict the density and velocity at a time instance $t = 2 \times 10^{-6}$ s, and the dotted lines represent the initial solution at $t = 0$. The third column shows temperature profiles in mixture space and point symbols along the dotted line visualize the number of grid points across the initial interface. We observe large differences between FC-F and QC-F formulations on the coarsest grid, Fig. 4.2(a-c). The FC-F method shows unphysical velocity oscillations, whereas the QC-F method yields smooth profiles. Note that physical diffusion causes a change in velocity on the right-hand side of the advected contact discon-

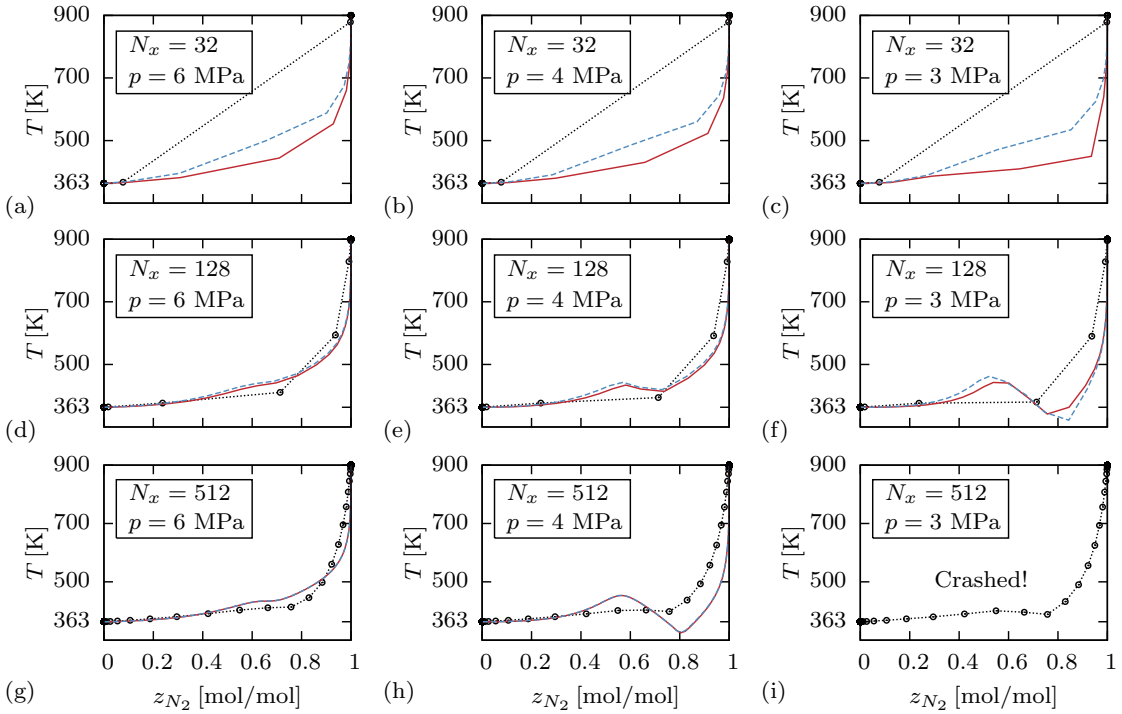

Figure 4.3: Effect of pressure on 1-D diffusion test case ($u = 0$ m/s) at thermodynamic conditions similar to Spray A ($T_{N_2} = 900$ K, $T_{C_{12}H_{26}} = 363$ K) for FC-F (solid red) and QC-F (dashed blue) formulations. Solution time is $t = 2 \times 10^{-6}$ s. Temperature profiles are shown in mixture space; Dashed-dotted line illustrates the initial temperature profile (T_F) and initial number of points across the interface. Increasing grid resolution from top to bottom. Decreasing pressure from left to right.

tinuity. The QC-F method shows much higher temperatures on the n-dodecane side (left) compared to the FC-F method. With increasing grid resolution, spurious oscillations of the FC-F method become less severe and eventually disappear, and the temperature profile of the QC-F method converges towards the FC-F solution. We conclude from these results that energy-conservation errors – necessary to maintain velocity and pressure equilibria at interfaces without the generation of spurious oscillations – translate into errors in temperature on coarse grids and both methods converge to the same solution on sufficiently fine grids.

In Fig. 4.3 we demonstrate the effect of pressure in our 1-D example. The advection velocity u was set to zero in order to reduce the energy-conservation error for the QC-F method. As a consequence, convergence among the two methods is

obtained on coarser grids. The initial temperatures of the pure components are the same as in Fig. 4.2, i.e., $T_{N2} = 900$ K and $T_{C12H26} = 363$ K. The pressure is decreasing from left to right from 6 MPa to 4 MPa to 3 MPa, the number of cells in the region of interest is increasing from top to bottom row from 32 to 128 to 512. The dashed-dotted line illustrates the initial temperature profile T_F and initial number of points across the interface. The solid red and dashed blue lines correspond the solution of the FC-F and QC-F method, respectively, at a time instance $t = 2 \times 10^{-6}$ s. Results for the 6 MPa case are very similar to Fig. 4.2 (right column), except that convergence of the temperature profiles in mixture space is obtained with less grid points between the two approaches. Under a pressure of 4 MPa the interplay between diffusional transport and EOS leads to a temperature profile in mixture space with local maxima and minima. Under a pressure of 3 MPa these local extrema become more severe and unphysical states appear in the computational domain causing numerical instability for both QC-F and FC-F methods on the finest grid. Apparently, under "low pressure" conditions the use the assumed single-phase thermodynamic closure leads to an unphysical solution for this relatively simple diffusion-dominated flow problem. Unphysical solution means in this context that e.g. a negative pressure is obtained as solution to equation Eq. (2.59) (FC) or Eq. (2.60) (QC) when using the single-phase thermodynamic closure. With regard to LES of Spray A, one may expect that low-pressure regions, e.g., in well resolved vortex cores, may lead to numerical problems.

4.4 LES of ECN Spray A

4.4.1 Grid and Boundary Conditions

The computational domain is shown in Fig. 4.4. All simulations have been performed in a rectangular domain with the overall dimensions $L_x = 56$ mm ($\sim 622 D_i$) in the streamwise and $L_y = L_z = 28$ mm ($\sim 311 D_i$) in the lateral directions, where $D_i = 0.09$ mm is the injector diameter. We use an adaptive Cartesian blocking strategy with a static local refinement and a varying grid resolution along the spray break-up trajectory to keep computational costs tractable. The grid consists of 2766 blocks with 7 grid-refinement levels and a total number of about 15.1 million cells. Note that the spatial extend of turbulent structures in the near-nozzle region differs significantly from those further downstream. For example, at a streamwise location of $x = 35$ mm, the diameter of the spray cone is roughly 12 mm, which is

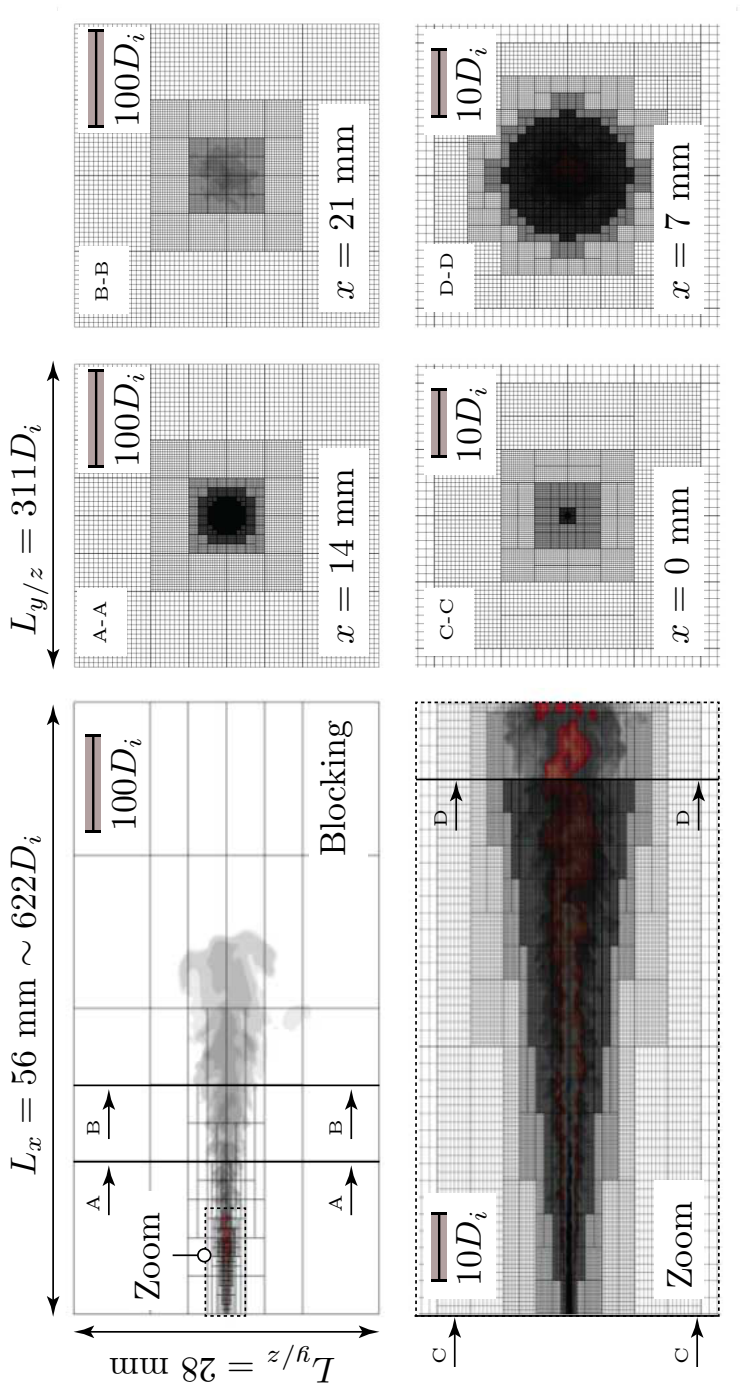

Figure 4.4: Blocking and grid resolution ($\mathcal{G}^2$) of the computational domain for LES of Spray A. Note the different scaling factors between top and bottom row.

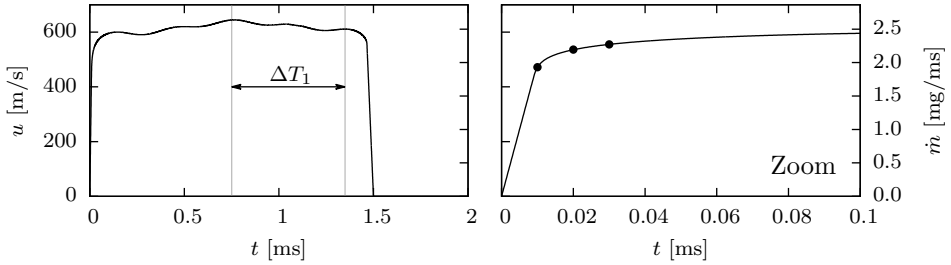

Figure 4.5: Injection profile used for LES of Spray A. Left y-axis: Prescribed velocity calculated from mass flow rate with $\rho_{PR}(T = 363\ \text{K}, p = 6\ \text{MPa}) = 643.25\ \text{kg/m}^3$. Right y-axis: prescribed mass flow rate. Points mark time instances shown in Fig. 4.13.

about 133 times the injection hole diameter. Here, much coarser cells compared to the near-nozzle region are reasonable and necessary given limited computational resources. The smallest cells with $\Delta y_{min} = \Delta z_{min} \sim 6.84\ \mu\text{m}$ and $\Delta x_{min} = 2\Delta y_{min}$ are located in the near-nozzle region ($x < 7$ mm), see the zoomed view in Fig. 4.4. The injector diameter D_i is discretized with about 13 cells. The coarsest cells with $\Delta y_{max} = \Delta z_{max} = \Delta y_{min} \times 2^6 \sim 0.44$ mm and $\Delta x_{max} = 2\Delta y_{max}$ are located in regions that are not of interest, e.g., the outer most cells in cut A-A in Fig. 4.4. The suitability of the grid has been verified by a grid convergence study, see Sec. 4.4.2.

Figure 4.5 depicts the time-dependent velocity and mass flow rate profile that is prescribed for Spray A ($T_A = 900\ \text{K}, p_A = 6\ \text{MPa}$) simulations. The mass flow rate profile is taken from the CMT website (`http://www.cmt.upv.es/ECN03.aspx`) with the following input parameters: injection pressure: 150 MPa; outlet diameter: 0.09 mm; fuel density: 703.82 kg/m^3; back pressure: 6 MPa; discharge coefficient: 0.89; injection time: 1.5 ms. The prescribed velocity block profile is calculated from the mass-flow rate with $\rho_{PR}(T = 363\ \text{K}, p = 6\ \text{MPa}) = 643.25\ \text{kg/m}^3$. The nozzle internal flow is therefore not simulated. We do not introduce any artificial turbulent fluctuations at the inflow patch, since we expect the jet break-up process to be controlled by massive shear forces and high hydrodynamic pressure fluctuations induced by the high-speed jet. At the outlet we prescribe the static pressure of 6 MPa together with a linear extrapolation procedure of all conservative flow variables. All walls are modeled as adiabatic.

Figure 4.6 shows the density, specific heat capacity at constant pressure, speed of sound and dynamic viscosity prediction as function of temperature for pure n-dodecane at a pressure of 6 MPa for different cubic EOS models. Reference

data is taken from the NIST (Lemmon et al., 2013). The gray line indicates the n-dodecane injection temperature of 363 K. It is worth noting that popular EOS such as the PR EOS and SRK EOS are not able to accurately reproduce the density of the NIST reference data at temperatures that are typical for injection systems, see Fig. 4.6(a). The same is true for other hydrocarbons, see, e.g., Kim et al. (2012). For the operating conditions of Spray A, the error in density prediction of the PR EOS compared to the the NIST reference data is about 8.6%. To match the mass-flow measurement, it is necessary to increase the injection velocity. Thus, the error in density prediction leads to an error in velocity of about 50 m/s. We checked the sensitivity of vapor penetration trajectories (i.e., vapor penetration over time) to uncertainties resulting from the EOS model, i.e., fuel density ρ_{fuel}, ambient gas density ρ_{amb} and inflow velocity, with the *uniform-profile model* of Naber and Siebers (1996). As a result we must expect a slight but systematic overestimation of the vapor penetration by about 3% at Spray A conditions in the LES. The same holds for the liquid length L_l where we may face – according to the *liquid length scaling law* of Siebers (1999) (Eq. 18b, $L_l \propto \sqrt{\rho_{fuel}/\rho_{amb}}$) – a systematic underestimation of about 2% for the cases #1-3 and 4% for case #4 (see Tab. 4.1 for the operating point description).

The accuracy of the PR EOS could be improved by volume translation methods; however, we refrain from applying such methods in the VLE framework because of additional computational costs and possible thermodynamic inconsistencies (Matheis et al., 2016). As indicated in Fig. 4.6(a), a new and promising candidate to improve liquid densities of hydrocarbons while maintaining the simplicity of the framework associated with cubic EOS is the generalized Redlich-Kwong-Peng-Robinson (RKPR) EOS (Cismondi and Mollerup (2005), see also the comprehensive paper of Kim et al. (2012)).

4.4.2 Grid Convergence Study

To assess the quality of the LES results, we present a grid convergence study for which we uniformly refined ($\mathcal{G}^3$) and coarsened ($\mathcal{G}^1$) the base grid ($\mathcal{G}^2$) by a factor of 2. For the highest ($\mathcal{G}^3$) and lowest ($\mathcal{G}^1$) grid resolution we obtain a total number of about 1.89×10^6 and about 120.9×10^6 computational cells, respectively. For reasons discussed in Section 4.4.3, the grid convergence study is conducted only for the FC set of governing equations together with the two-phase thermodynamic closure as introduced in Sec. 2.3. Figure 4.7 shows a temporal sequence of the injection event at different grid refinement levels $\mathcal{G}^1$ (left), $\mathcal{G}^2$ (center), and $\mathcal{G}^3$ (right). Instantaneous snapshots of the temperature field (contour levels

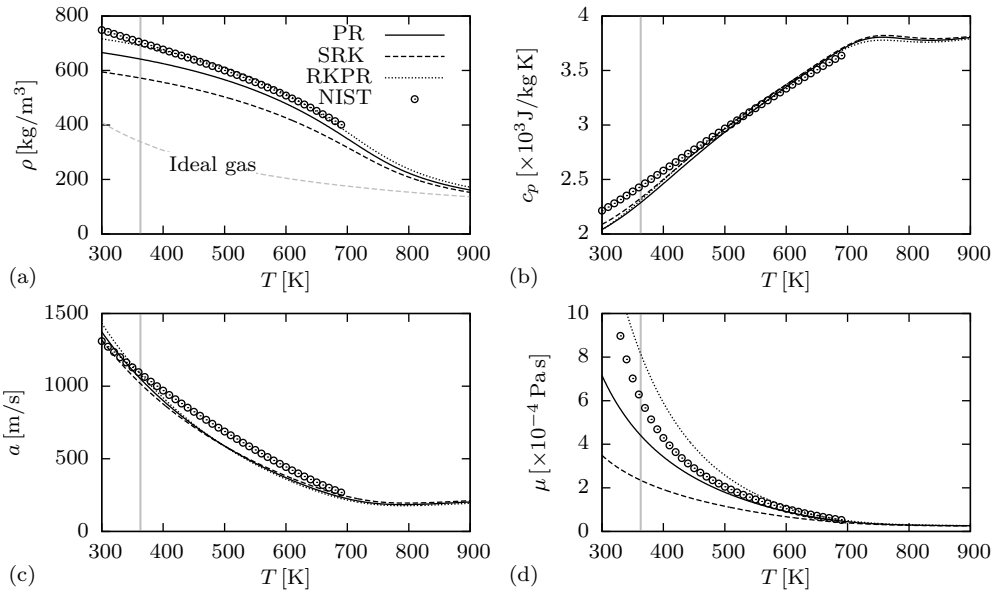

Figure 4.6: Density (a), specific heat capacity at constant pressure (b), speed of sound (c) and dynamic viscosity (d) prediction for pure n-dodecane at a pressure of 6 MPa for different cubic EOS models, see panel (a) for the line legend. Reference data is taken from the NIST (Lemmon et al., 2013). The gray line indicates the n-dodecane injection temperature of 363 K.

are shown for 363 K $< T <$ 900 K, from dark to light shades), superimposed by the vapor volume fraction distribution (contour levels are shown for $0 < \alpha_v < 1$, from blue to red shades) are shown. While $\mathcal{G}^2$ and $\mathcal{G}^3$ yield qualitatively a very similar jet break-up phenomenology and subsequent vapor penetration trajectory, we observe on the coarsest grid $\mathcal{G}^1$ a different and unphysical transient. Shear layer instabilities, which lead to a spreading and turbulent mixing in radial direction, start to develop at a later point in time after start of injection. As a consequence, we see a pocket of dense fluid traveling ahead of the spray tip, see Fig. 4.7(g). Knudsen et al. (2016) observed the same phenomenon on their coarsest grid. They concluded precisely that an *'insufficient transfer of momentum to the radial direction leaves an oversupply of axial momentum that convects the fuel vapor downstream too rapidly'*. Figure 4.8 shows a comparison of liquid and vapor penetration trajectories. Again, grid level $\mathcal{G}^2$ and $\mathcal{G}^3$ yield very similar liquid and vapor penetration trajectories. Slight differences can be observed when the liquid phase transitions to its quasi-steady mean, compare also Figs. 4.7(h) and (i). The coarsest grid $\mathcal{G}^1$ shows initially a significant overestimation of the initial

Figure 4.7: Temporal sequence of the injection event at different grid refinement levels $\mathcal{G}^1$ (left), $\mathcal{G}^2$ (center), and $\mathcal{G}^3$ (right). Instantaneous snapshots of the temperature field (contour levels are shown for 363 K $< T <$ 900 K, from dark to light shades) superimposed by the vapor volume fraction distribution (contour levels are shown for $0 < \alpha_v < 1$, from blue to red shades) are shown.

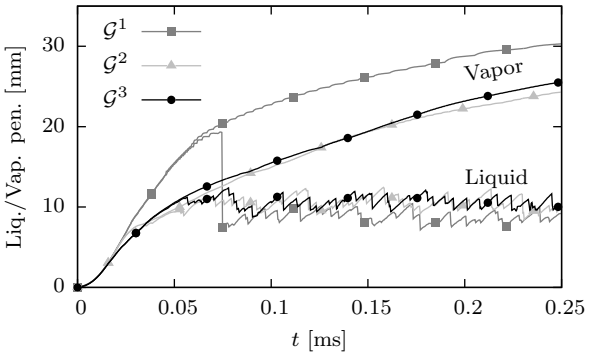

Figure 4.8: Numerical liquid and vapor penetration trajectories for different grid refinement levels $\mathcal{G}^1$, $\mathcal{G}^2$ and $\mathcal{G}^3$. The liquid core length L_l is defined as $\max\{x(LVF = 0.15\%)\}$, vapor penetration L_v is defined as $\max\{x(Y_{C12H26} = 1\%)\}$.

liquid phase penetration which then abruptly drops to its quasi-steady mean once all the liquid that was convected downstream too rapidly is vaporized. The offset in the vapor penetration persists for the time interval under consideration. For the time-averaged liquid length (0.10 ms $\leq t \leq$ 0.25 ms) we obtain 8.81 mm ($\mathcal{G}^1$), 10.51 mm ($\mathcal{G}^2$) and 10.65 mm ($\mathcal{G}^3$) along the different grid refinement levels. Given the negligible differences between base grid $\mathcal{G}^2$ and refined grid $\mathcal{G}^3$ (but significant differences with respect to computational time and resources) we used only the base grid $\mathcal{G}^2$ in all subsequent simulations.

4.4.3 Comparison to Experimental Data

In the following we use experimental reference data to evaluate our numerical results obtained with the quasi-conservative single-phase model (QC-F) and with the fully conservative equilibrium two-phase model (FC-EQ). The fully conservative single-phase method (FC-F) encountered numerical instabilities during the start-up phase when the jet accelerates from 0 to 600 m/s in just 10 μs. A total time interval of 1.5 ms has been simulated. Figure 4.9 depicts a temporal sequence of the early jet evolution (24μs-104μs). The left column shows experimental data (diffused back illumination, DBI). The center and right columns show snapshots of the temperature distribution for LES with FC-EQ and QC-F methods, respectively. In the case of FC-EQ, the liquid penetration length is illustrated by the cyan iso-contour of the liquid volume fraction $LVF = 0.15\%$. We observe a very good qualitative agreement between experimental data and LES with the FC-EQ

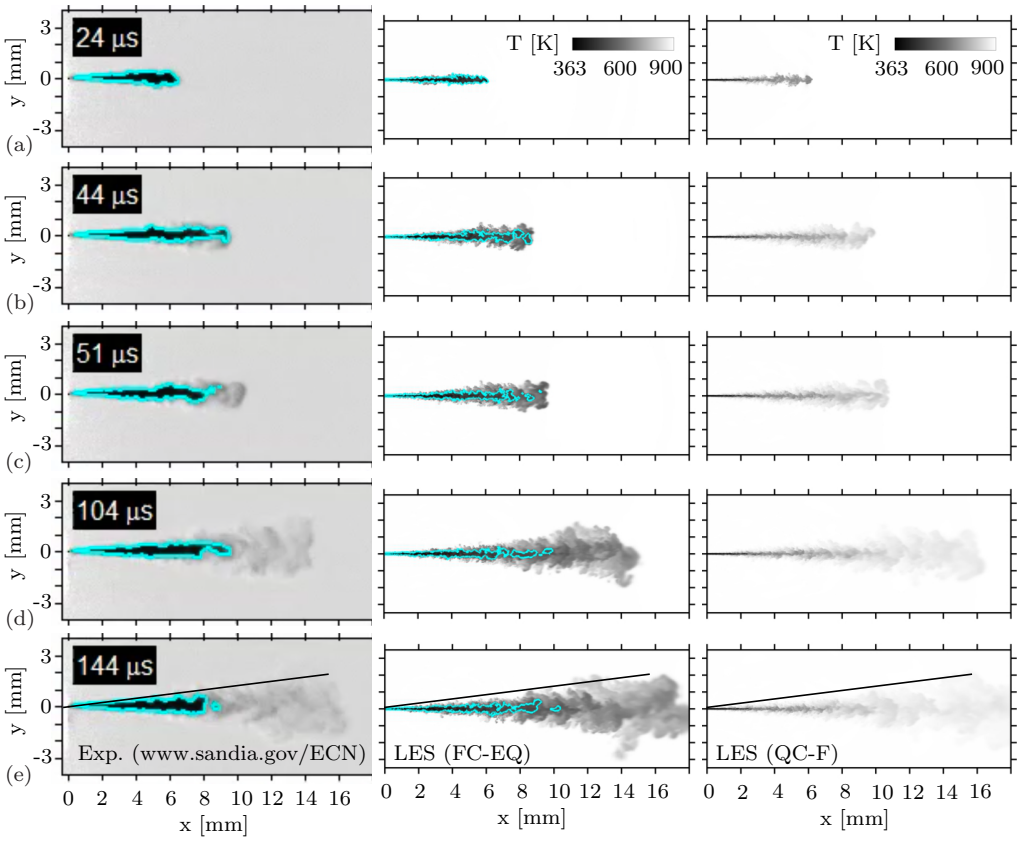

Figure 4.9: Temporal sequence of the injection event. Left column: experimental data of Pickett et al. (2011a); center column: LES with FC-EQ; right column: LES with QC-F. Instantaneous snapshots of the temperature distribution are shown for LES data. Liquid penetration length is illustrated by a $LVF = 0.15\%$ iso-contour.

method. At 24 μs the liquid n-dodecane jet extends about 6 mm into the nitrogen atmosphere; at about 44 μs the liquid length has reached its quasi-steady mean. Later points in time illustrate the vapor evolution. QC-F and FC-EQ simulations predict a very similar vapor penetration trajectory; however, significant differences are observed for the temperature field. The dense n-dodecane jet heats up more quickly and mixing takes place at much higher temperatures with the QC-F model. This effect is not caused by the thermodynamic modeling approach (assumed single-phase vs. two-phase), but rather by energy-conservation errors of the QC method.

Figure 4.10 shows the temperature-composition phase diagram for the nitrogen-

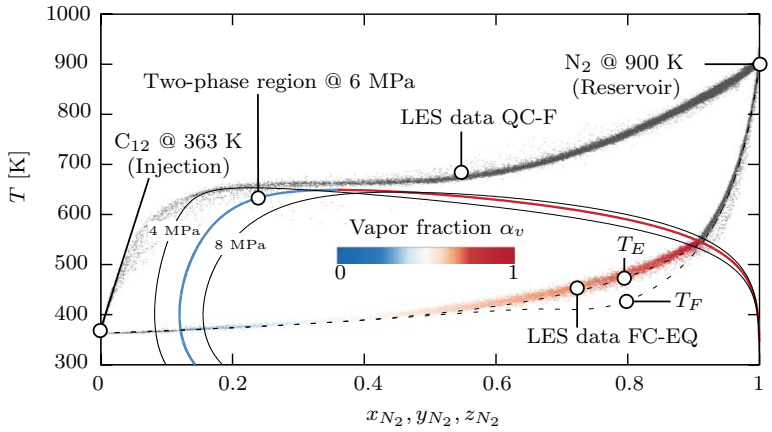

Figure 4.10: Temperature-composition diagram for a $N_2 - C_{12}H_{26}$ mixture with frozen (T_F) and equilibrium (T_{EQ}) mixing temperature. Scattered data depict the thermodynamic states that are obtained in the QC-F and FC-EQ LES at 144 μs. For FC-EQ, points within the two-phase region are colored by vapor volume fraction.

dodecane mixture together with frozen (T_F) and equilibrium (T_{EQ}) mixing temperature. The two-phase region is indicated at a pressure of 6 MPa (nominal operating pressure), 4 MPa and 8 MPa. Scattered data depict the thermodynamic states that are obtained in the LES with the methods FC-EQ and QC-F, instantaneous data is taken from Fig. 4.9(d). In the case of FC-EQ, data points within the two-phase region are colored by the vapor volume fraction from blue to red shades. While the FC-EQ LES follows closely the equilibrium mixing temperature, we observe a completely different mixing for the QC-F LES. Above, we demonstrated that the QC solution converges towards the FC solution on fine grids. This means for the LES of Spray A that the QC-F temperature prediction will eventually converge towards the FC solution within the single-phase region when increasing the number of cells and hence reducing the energy conservation error. We therefore conclude that the energy conservation error of the QC method, which translates into an error in temperature, is not controllable for the present application and typical LES grid resolutions. The use of a QC formulation is certainly problematic for flows where a precise temperature prediction is mandatory, such as auto-ignition.

Fedkiw et al. (2002) suggested to use the pressure obtained from the pressure-evolution equation only in regions where the interface is numerically problematic. Based on a flow sensor, a non-conservative energy can be calculated from the QC pressure prediction, which locally replaces the energy computed with the FC method. Such an algorithm could improve the energy-conservation properties but

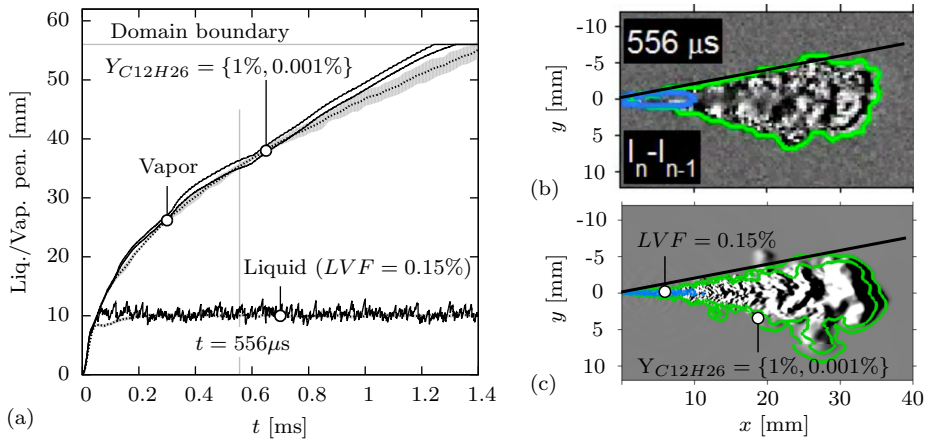

Figure 4.11: (a) Numerical (——) and experimental (·····) liquid and vapor penetration trajectories. For LES the liquid core length L_l is defined as $\max\{x(LVF = 0.15\%)\}$, vapor penetration L_v is defined as $\max\{x(Y_{C12H26} = 1\%)\}$ and $\max\{x(Y_{C12H26} = 0.001\%)\}$. (b) Experimental schlieren image. (c) Numerical schlieren image for FC-EQ LES. See Refs. Pickett et al. (2011a,b) and `http://www.sandia.gov/ecn/` for details on experimental data (Sandia; Injector SN 210677; 0% O_2; Injection duration 1.5 ms).

is beyond the scope of this work. In the following we will restrict ourselves to the presentation of LES results that have been obtained with the FC formulation.

A quantitative comparison between experiment and the FC-EQ LES is given in Fig. 4.11(a) for the liquid and vapor penetration trajectories. In the LES the liquid core length is defined as $L_l = \max\{x(LVF = 0.15\%)\}$, vapor penetration L_v is shown for the definitions $\max\{x(Y_{C12H26} = 1\%)\}$ and $\max\{x(Y_{C12H26} = 0.001\%)\}$. We observe an excellent agreement of L_l with the experimental time-resolved signal. It is important to note that the measured L_l depends on the chosen threshold value. Based on a thorough analysis based on Mie-scatter theory together with assumptions on droplet diameters, Pickett et al. (2011a, 2015) conclude that the LVF threshold representing their liquid length is expected to be less than 0.15% at Spray A conditions. The experimental length fluctuates by approximately ±1mm about the quasi-steady mean of 10.4mm; this value is in excellent agreement with our LES data for the threshold value of 0.15%. In order to evaluate the sensitivity on the threshold value, we computed L_l for $LVF = \{3\%, 1\%, 0.15\%, 0.05\%\}$ and obtained $L_l = \{8.83, 9.91, 10.40, 10.49\}$mm, respectively.

We also observe a good agreement of the vapor penetration trajectory up to ap-

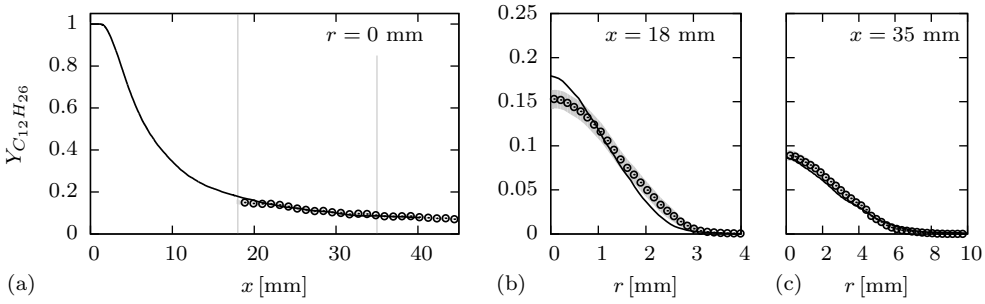

Figure 4.12: Axial (a) and radial (b,c) mixture fraction profiles. LES with FC-EQ (——); (⊙) experimental data of Pickett et al. (2011b), see also `http://www.sandia.gov/ecn/cvdata/assets/Rayleigh/bkldaAL4mixing.php`. Radial profiles are extracted at 18 mm and 35 mm.

proximately 0.6 ms. At later times the penetration depth is slightly overestimated. We expect a systematic over estimation of the vapor penetration due to shortcomings of the PR EOS with respect to the pure n-dodecane density prediction, see Sec. 4.4.1 for a more detailed discussion. In the experiment, the vapor penetration length is derived from high-speed schlieren images. Figure 4.11(b-c) give an impression on how a mixture-fraction threshold compares to a schlieren image. The numerical schlieren image shows the axial density gradient $\partial\rho/\partial x$ spatially averaged along the z-direction. Liquid and vapor boundaries are defined in the same manner as in Fig. 4.11(a). Numerical and experimental image are strikingly similar. Quantitatively, the vapor penetration depth defined by a 1% mixture fraction threshold seems to slightly underestimate the vapor penetration derived from a schlieren image in the long term evolution.

In Fig. 4.12 we compare axial (a) and radial (b,c) mixture fraction profiles. Statistical properties have been obtained by averaging LES data in circumferential direction and over a certain time interval (ΔT_1 in Fig. 4.5). Following the argument of Knudsen et al. (2016), care must be taken when interpreting these results due to differences in the averaging methods (ensemble averaging vs. time- and circumferential averaging). LES results agree reasonably well with the experimental data. At the $x = 18$ mm station we see an overestimation of the n-dodecane mass fraction on the jet axis. At $x = 35$ mm LES and experimental data collapse.

Figure 4.13 shows a temporal sequence of the spray structure in the near-nozzle field at a very early state, 10 μs, 20 μs and 30 μs after start of injection. In the left column we show instantaneous snapshots of the temperature field (contour levels are shown for 363 K $< T <$ 900 K, dark to light gray shades). Superimposed

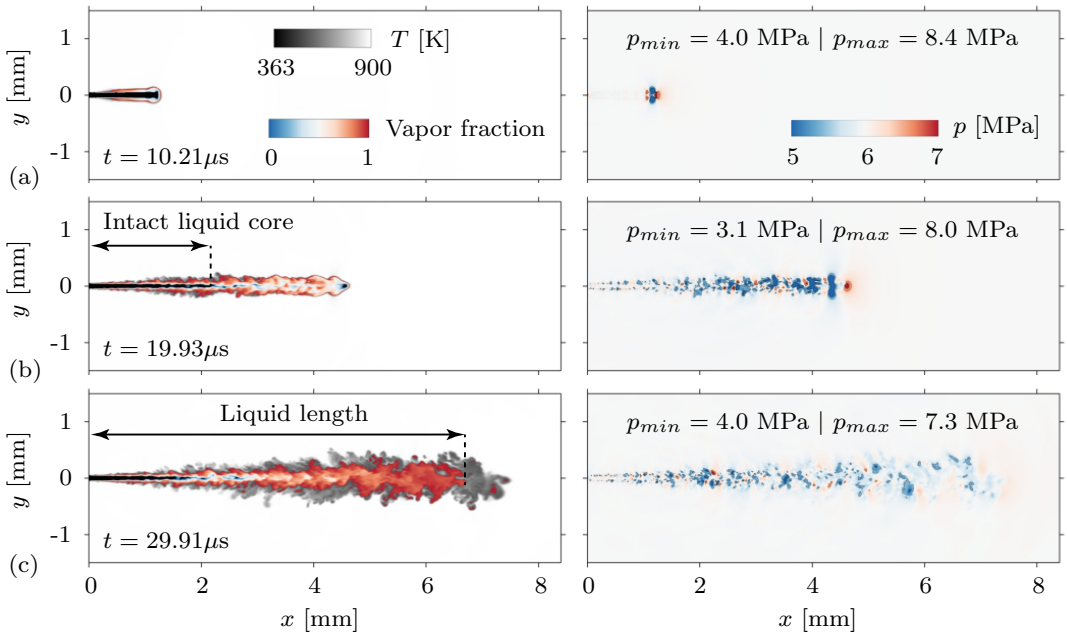

Figure 4.13: Temporal sequence of temperature (left) and pressure (right) for FC-EQ LES. Left column: Instantaneous snapshots of the temperature field (contour levels are shown for 363 K $< T <$ 900 K, from dark to light shades), superimposed by the vapor volume fraction distribution (contour levels are shown for $0 < \alpha_v < 1$, from blue to red shades). Right column: Instantaneous snapshots of the pressure field (contour levels are shown for 5 MPa $< p <$ 7 MPa, from blue to red shades) together with the maximum and minimum pressure at the corresponding time instance.

is the vapor volume fraction distribution (blue to red shades) for the two-phase region within which the isochoric-isoenergetic flash problem was solved (same coloring as FC-EQ data in Fig 4.10). Contours of the corresponding pressure fields (5 MPa $< p <$ 7 MPa, from blue to red shades) are shown in the right column. We see that the n-dodecane-nitrogen mixture locally experiences pressures much different from the average ambient pressure. A region of very low pressure, p is about 3 MPa, can be observed at the tip of the jet due to a start-up vortex ring, see Fig. 4.13(a,b). Just in front of the vortex ring, in the stagnation point of the jet, the pressure exceeds 8 MPa. Due to this high pressure, the mixture is here locally in a single-phase state.

Even in the fully developed steady state, we see pressure fluctuations in the shear layer in the order of ±1 MPa. We note that the QC-F method yields a pressure

field during ramp-up extremely similar to the FC-EQ results. This supports the conclusion that the reported pressure fluctuations are of physical origin and not caused by the interplay of numerics and nonlinear EOS. We mentioned above that we were not able to simulate Spray A with a conservative single-phase model (FC-F). The instabilities encountered are caused by our single-phase thermodynamics model, which yields ill-defined states at low pressures that occur in well-resolved vortex cores. Compare also our results for the 1-D diffusion test case presented in Sec. 4.3. Our fully conservative two-phase LES model (FC-EQ) did not face any stability problems because the more sophisticated model can resolve multi-component subcritical two-phase states, thus avoiding unphysical states. The QC-F LES did not encounter any instabilities since mixing takes place at much higher temperatures avoiding unphysical states within the two-phase region.

4.5 Parameter Variation

In addition to the baseline case Spray A, we evaluate the two-phase model for three other operating conditions, which are given in Tab. 2. Case #1 and case #3 have nominal the same ambient density as Spray A (case #2, $\rho_{amb} = 22.8$ kg/m^3) but differ in ambient pressure and temperature. Case #4 has a much lower nominal ambient density of $\rho_{amb} = 7.6$ kg/m^3 and the same nominal ambient temperature as Spray A ($T_{amb} = 900$ K). We compare LES data with diffused back illumination (DBI) data (see `https://ecn.sandia.gov/dbi675/`) and quasi-steady liquid-length measurements (Manin et al., 2012). All simulations in the following section are conducted with the fully conservative two-phase LES model. The computational domain for the cases #1 and #2 is the same as described in Section 4.4.1. To ensure the same grid resolution in regions with two-phase flow, $x < L_l$, we adjusted the grid coarsening levels for the cases #3 and #4. The $\times$ symbols on the y-axis in Fig. 4.15 mark the axial position at which the grid is coarsened by a factor of 2. As it can be seen, the two-phase region does not exceed the 3rd grid-coarsening level for all cases under consideration. The mass flow rate profile is taken from the CMT website (`http://www.cmt.upv.es/ECN03.aspx`). Back pressure p_{amb}, n-dodecane density ρ_{fuel} (NIST) and the density of the nitrogen atmosphere for the different operating points are summarized Table 4.1. Inflow boundary conditions are then defined in the same manner as for the LES of Spray A, see Section 4.4.1. A total time interval of 0.5 ms has been simulated, which is sufficient to obtain the quasi-steady liquid length.

Figure 4.14 depicts a qualitative comparison between experimental DBI images

Table 4.1: Test case definition. [a] Nominal experimental operating conditions according to Manin et al. (2012). [b] Calculated using the PR EOS with p_{amb}; pure nitrogen atmosphere in the LES. [c] From the NIST (Lemmon et al., 2013) at p_{amb} and $T_{fuel} = 363$ K. [d] Calculated using the PR EOS at p_{amb} and $T_{fuel} = 363$ K.

Case	T_{amb} [K]	p_{amb} [MPa]	ρ_{amb} [kg/m^3]	ρ_{fuel} [kg/m^3]
#1	1200[a]	8.00	22.8[a]/22.04[b]	705.79[c]/645.14[d]
#2 (Spray A)	900[a]	6.00	22.8[a]/22.06[b]	703.82[c]/643.25[d]
#3	700[a]	4.60	22.8[a]/21.80[b]	702.40[c]/641.86[d]
#4	900[a]	2.04	7.6[a]/7.59[b]	699.74[c]/639.16[d]

(`https://ecn.sandia.gov/dbi675/`) and instantaneous LES snapshots of the temperature field (contour levels are shown for 363 K $< T < T_{amb}$, from dark to light shades), superimposed by the vapor volume fraction distribution (contour levels are shown for $0 < \alpha_v < 1$, from blue to red shades). Solid lines indicate roughly the liquid and vapor penetration lengths as well as spreading angle of the spray obtained from the experimental DBI snapshot. Figures 4.14(a)-(c) illustrate the effect of decreasing the ambient temperature from $T_{amb} = 1200$ K to $T_{amb} = 900$ K and $T_{amb} = 700$ K at nominal constant ambient density $\rho_{amb} = 22.8$ kg/m^3. Qualitatively, the trend of an increasing liquid penetration length, caused by a decreased evaporation rate at lower temperature, is well reproduced in the LES. We also see that the dark region, which represents roughly the liquid phase in the experiment, spreads in radial direction with decreasing temperature. A similar observation can be made for the colored two-phase region. The penetration depth of the more diffusive region that represents vaporized fuel does not differ much between the three cases due to the same nominal ambient density. As discussed in Sec. 4.4.1, we see a minor systematic overestimation of the tip penetration in the LES for all cases under consideration. Figure 4.14(d) compares the DBI and LES snapshot at a much lower ambient density of $\rho_{amb} = 7.6$ kg/m^3. We observe a longer liquid core, an increased penetration depth of vaporized fuel and a smaller spray spreading angle compared to the baseline case. Qualitatively, LES and DBI image share these characteristics, however, the liquid penetration length appears to be slightly underestimated in the LES.

In Fig. 4.15, we compare quantitatively experimental (for references see the caption of Fig. 4.15) and numerical liquid-penetration trajectories. Again, in the LES the liquid-core length is defined as $L_l = \max\{x(LVF = 0.15\%)\}$. In the experiment the liquid penetration length is derived from DBI images based on a

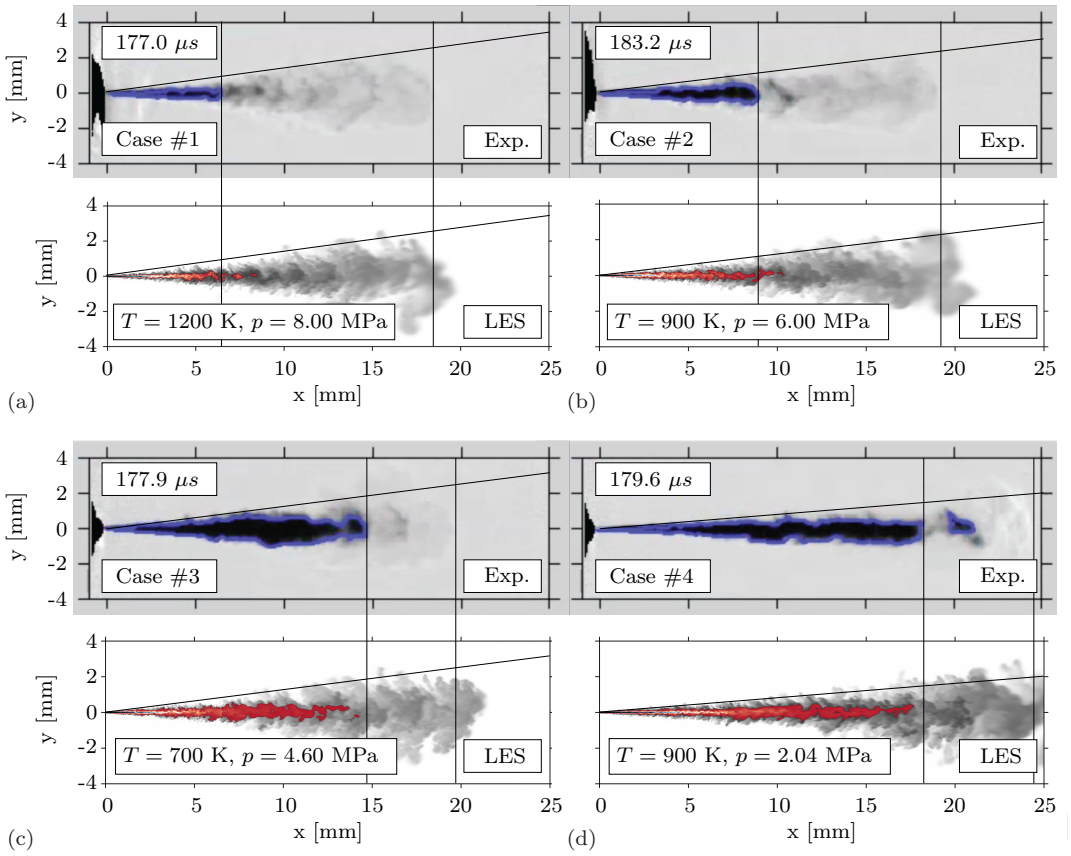

Figure 4.14: Comparison between experimental diffused back illumination (DBI) images (`https://ecn.sandia.gov/dbi675/`, see also Manin et al. (2012)) and instantaneous LES snapshots of the temperature field (contour levels are shown for 363 K $< T < T_{amb}$, from dark to light shades), superimposed by the vapor volume fraction distribution (contour levels are shown for $0 < \alpha_v < 1$, from blue to red shades).

threshold criterion quantifying the loss of light through the spray. For a thorough discussion we refer to Manin et al. (2012) and Pickett et al. (2011a, 2015). In panel (b) of Fig. 4.15, baseline case Spray A (case #2), we included also liquid penetration data from another injector. Nominally all injectors share the same specification, however, each individual injector is slightly different due to manufacturing accuracies. The differences between the two data sets may thus serve as an estimate for the experimental uncertainties. We see a very good prediction of the time-resolved signal for the 1200 K (case #1) and 900 K (case #2) atmosphere and a good prediction for the 700 K (case #3) atmosphere and the low-density atmosphere (case #4). Interestingly, all experimental data show a longer initial

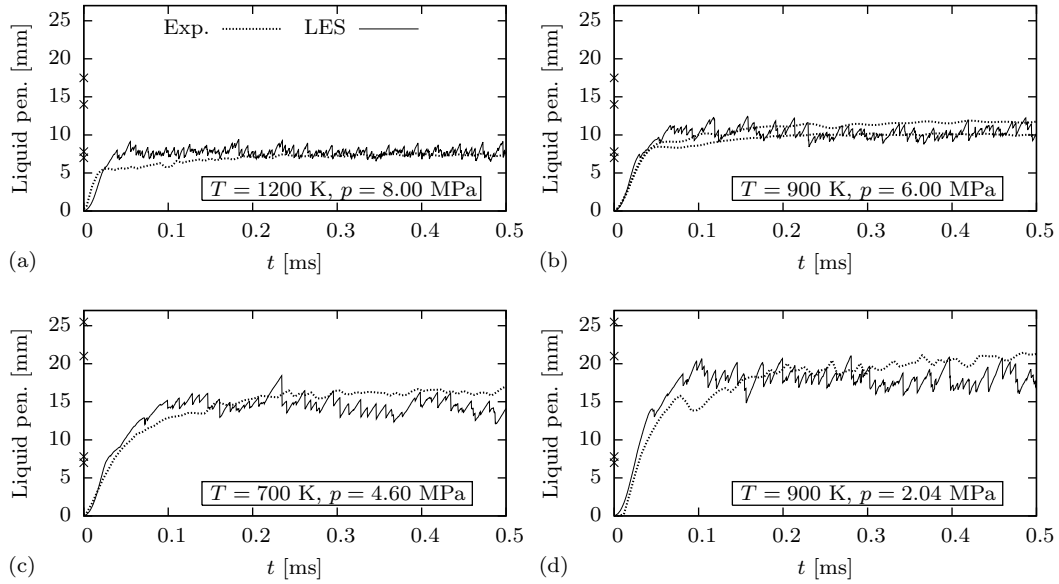

Figure 4.15: Numerical (——) and experimental (·····) liquid penetration trajectories for cases #1–#4. For LES the liquid core length L_l is defined as $\max\{x(LVF = 0.15\%)\}$. See Manin et al. (2012) and `https://ecn.sandia.gov/dbi675/` for details on experimental data (Sandia; Injector SN 210675; 0% O_2; Injection duration 1.5 ms). In panel (b), baseline Spray A (case #2), we show also liquid penetration data from Injector SN 210677, cf. Fig. 4.11(a).

transient until a quasi-steady liquid length is established in comparison to our LES results, most prominent for case #4 where the quasi-steady liquid penetration is reached only for $t > 0.5$ ms. LES data show an initial transient of $t < 0.1$ ms. These differences are expected to stem from uncertainties in the individual inflow boundary conditions used in the LES, which do not include wave dynamics within the injector.

In conclusion, we found an overall good qualitative and quantitative agreement between experiment and LES for all four operating points, demonstrating the excellent predictive performance of the present methodology for LES of high-pressure high-temperature fuel injection processes.

4.6 Summary

The two-phase model for the Eulerian LES of turbulent mixing under high-pressure conditions has been applied to liquid hydrocarbon injection at operating conditions relevant to diesel engines. Computational results for baseline case ECN Spray A and three additional test cases demonstrated the excellent predictive performance of the present approach. The availability of the liquid volume fraction through the homogeneous mixture approach provided a non-arbitrary definition of the liquid penetration length that can be linked to experimental measurements. Grid convergence of integral properties, i.e., liquid and vapor penetration trajectories, has been proven for the baseline case ECN Spray A.

We saw that the Spray A n-dodecane-nitrogen mixture locally experiences pressures significantly below the nominal operating pressure of 6 MPa when the jet accelerates from 0 to 600 m/s in just 10 μs. For these harsh conditions, LES with a conservative dense-gas single-phase approach exhibit large spurious pressure oscillations that may cause numerical instability even with low-order upwind numerics. It has been suggested previously that stable time integration of single-phase thermodynamic models can be obtained by "energy-correction methods" that sacrifice energy conservation in some way. We therefore compared a fully conservative formulation of the governing equations with a quasi-conservative formulation based on a pressure-evolution equation. A one-dimensional multi-component advection-diffusion test case proved physical and numerical consistency of both methods and convergence towards the same solution for sufficiently fine grids. On coarser grids, however, energy conservation errors associated with the quasi-conservative formulation caused a significant overestimation of the temperature. LES with the fully conservative multi-component two-phase equilibrium model did not show any stability problems for all test conditions and yielded numerical predictions that are in very good agreement with available experimental data. We therefore concluded that VLE calculations are necessary for a stable and physically meaningful Eulerian LES based on a homogeneous mixture approach with real-fluid EOS for the cases under consideration.

Chapter 5

Concluding Remarks

5.1 Summary

The objective of the present work was to develop numerical tools for Large-Eddy Simulations (LES) of fuel injection and turbulent mixing under high-pressure conditions. Such conditions are found in liquid rocket engines (LRE), modern diesel engines and gas turbines. The operating pressure and temperature in these devices is often well above the critical pressure and temperature of the pure injectants. Prior to injection, however, the propellants/fuels are in a compressed liquid state at low subcritical temperatures to allow for high densities and compact storage. The injection of such compressed liquids into high-pressure (and possibly high-temperature) atmospheres is typically described in one of two ways: Jet-disintegration either resembles a classical spray with primary and secondary breakup and potentially evaporation of droplets or turbulent dense fluid mixing with no visual evidence of surface tension. Under which operating conditions which type of jet-disintegration occurs is not well understood. One reason for this is that multi-component systems do not have a single critical point. Instead, critical loci

that are a complex function of temperature, pressure, and composition define the thermodynamic state. Hence, local conditions downstream of injection become extremely important. For example, the critical pressure of a mixture often exceeds many times the critical pressure of the pure components. Therefore, subcritical regions in the flow may exist even through the operating pressure is well above the critical pressure of the injectants. Another reason is that experimental investigation of fuel and mixture supercriticality is difficult to attempt because of the harsh conditions found in LREs or diesel engines. A clear characterization of the type of jet disintegration under high-pressure and high-temperature conditions is hence not always straightforward. Limiting factors are, for instance, spatial and temporal resolution and the integrative nature of measurement-techniques such as shadowgraphy.

Numerical simulations, on the other hand, can provide detailed insights into the flow physics. The main objective of this work was hence to develop a numerical framework capable to represent the physics of high-pressure mixing such as phase transition phenomena, i.e., evaporation or condensation, and supercritical mixing in multi-component environments. State-of-the-art for LES of high-pressure flows is the use of thermodynamic closures based on cubic equations of state (EOS). If no special measures are taken, this approach – commonly referred to as dense-gas approach – implicitly assumes fuel- and mixture supercriticality in the entire flow field. To improve on this limitation, a thermodynamic model based on cubic EOS, thermodynamic stability analysis and vapor-liquid equilibrium (VLE) calculations was presented in this thesis. This model accurately represent supercritical states as well as coexisting multi-component subcritical two-phase states by means of a homogeneous mixture approach. Primary atomization is represented in an Eulerian framework. The model accounts for fuel compressibility and effects associated with real-fluid thermodynamics, such as the solubility of ambient gas into the liquid phase or variable thermo-physical properties. Hence, the present approach yields a thermodynamically consistent and tuning-parameter-free framework without any semi-empirical break-up and evaporation models. The only input parameters required are the NASA polynomials, the critical properties, and the acentric factor of each species, and, if available, the binary interaction parameter.

First, the shear coaxial injection of liquid nitrogen and gaseous hydrogen at supercritical pressures (with respect to the pure components) was studied. An operating point from the series of experiments of Oschwald et al. (1999) was selected for which quantitative density measurements are available. LES results with the single-phase model (dense-gas approach) showed interesting thermodynamic phenomena such as endothermic mixing and partial hydrogen densities exceeding the inflow value within the turbulent shear layer. The latter was recorded also experimentally,

however, the overall quantitative agreement between LES and experiment was not satisfactory. The inflow temperature of the main nitrogen injection was found crucial for the reproduction of the experimental results. By analyzing VLE data, it was also found that some states obtained in the LES lie well within the two-phase region. To characterize the effect of phase-separation, LES with the more sophisticated two-phase model were performed. Detailed information on partial densities in both liquid and vapor phases raised the interesting question which density was actually measured by Raman spectroscopy in case of potential two-phase flow. The quantitative agreement between LES and experimental density measurements did not improve when using the two-phase model. In addition, the effect of numerical diffusion was addressed by means of a grid convergence study and the use of a more dissipative numerical scheme. Grid resolution had a significant effect on integral properties such as the jet break-up position and it was further not possible to demonstrate grid convergence due to the high Reynolds number of the flow. Characteristic thermodynamic phenomena, on the other hand, were very similar on all grid levels for this test case.

Next, the injection of a liquid hydrocarbon into a high-pressure, high-temperature atmosphere was studied. The test case is known as ECN Spray A and the operating conditions resemble that of a modern diesel engine. Computational results for baseline case Spray A and three additional operating points using the two-phase thermodynamic closure demonstrated the excellent predictive performance of this approach. Furthermore, the availability of the liquid volume fraction through the VLE-based approach provided a non-arbitrary definition of the liquid penetration length that can be linked to experimental measurements. In contrast to the coaxial injection case, it was not possible to use the single-phase thermodynamic model (dense-gas approach) in a fully-conservative formulation of the governing equations. Unphysical states in the flow field were observed causing numerical instability. It is known that LES under such harsh conditions can be very challenging with respect to numerical stability. The use of energy non-conserving methods can help to stabilize the simulation. Therefore, a comparison was presented between a fully conservative formulation of the governing equations with a quasi-conservative formulation based on a pressure-evolution equation. A one-dimensional multi-component advection-diffusion test case proved physical and numerical consistency of both methods and convergence towards the same solution for sufficiently fine grids. On coarser grids, however, energy conservation errors associated with the quasi-conservative formulation caused a significant overestimation of the temperature. Therefore, the main conclusion was that the two-phase thermodynamic closure is absolutely necessary for a stable and physically meaningful Eulerian LES of Spray A.

5.2 Outlook

There are a number of aspects that require further investigation: The two-phase thermodynamic closure must be evaluated for non-vaporizing conditions, which will be considered as part of future research. In a dilute flow regime, i.e., very small liquid volume fraction, particle-particle interactions are rare, the continuum assumption, which goes hand in hand with the pure Eulerian framework, is essentially invalid. If the spatial extend of dilute flow regions is large compared to moderately dense and very dense regions, as it is the case for non-vaporizing conditions, we expect to see limitations of the homogeneous-mixture approach. In this situation, a coupling between the Eulerian VLE-based two-phase model and a Lagrangian spray solver, see, e.g., Gaillard et al. (2016b), may help to improve the predictive performance of the simulation. Future work should also characterize the sensitivity of integral flow properties, such as liquid and vapor penetration trajectories with respect to the EOS, the binary interaction parameter and inflow boundary conditions (e.g., nozzle internal flow, velocity profile, synthetic turbulence). The coupling between internal nozzle flow and the main injection event is also an interesting task for future research. Because cavitation can be handled in a cubic EOS based framework, see, e.g., Star et al. (2006), the full simulation of a diesel injection cycle including needle movement – as it was done by Örley et al. (2017) – is feasible. A further issue is the calculation of thermo-physical properties, e.g., specific heat, viscosity or thermal conductivity, in a multi-species two-phase system. In the homogeneous-mixture framework single-valued thermo-physical properties must be provided and the influence of the modeling of which should be quantified. It would also be very interesting to formulate the VLE-based thermodynamic model for the generalized Redlich-Kwong-Peng-Robinson (RKPR) EOS (Cismondi and Mollerup (2005), see also the comprehensive paper of Kim et al. (2012)) to improve the prediction of liquid densities of hydrocarbons while maintaining the simplicity of the framework associated with cubic EOS. In this work, only binary systems were studied. The application of the VLE-based closure to multi-component two-phase systems is without any further modification possible. However, at some point computational performance can become an issue. There exist more efficient solution strategies for both the equilibrium calculations at specified internal energy, volume and composition, see, e.g., Castier (2009), and the Tangent Plane Distance analysis, see, e.g., Hoteit and Firoozabadi (2006). Furthermore, improvements in the code architecture such as a partitioning that accounts for load imbalance caused by the VLE-based closure may help. Last but not least it would be of great practical interest to consider chemical reactions in these simulations. In case of LREs, the flame can be anchored at the coaxial

injector element, thus, separating oxygen and hydrogen. Whether or not local subcritical states can exist under such conditions is an interesting objective for future studies, see also the very recent work of Gaillard et al. (2016a). In the context of diesel engines – or more specifically Spray A and other operating conditions – the Eulerian VLE-based two-phase thermodynamic closure can help to improve the prediction of the transient mixing field prior to autoignition.

Appendix A

LES of the ITLR Case

In a joint effort between the University of Stuttgart, Bundeswehr University Munich, Delft University of Technology and Technical University Munich, experiments and numerical simulations were carried out to provide a better understanding of fuel injection under high-pressure conditions. The basic idea can be summarized as follows: N-hexane is injected through a single-hole injector into a quiescent nitrogen atmosphere at nominal 5 MPa chamber pressure and 293 K chamber temperature. The pressure in the chamber is therefore supercritical with respect to the critical pressure of n-hexane ($p_c = 3.0340$ MPa) and nitrogen ($p_c = 3.3958$ MPa). The total temperature of n-hexane within the injector is carefully controlled by two heater cartridges, see Baab et al. (2016) for details. The temperature range is selected such that jet disintegration is expected to undergo a transition from gaseous jet like mixing to a classical two-phase spray. Figure A.1 depicts the Txy-diagram for a binary n-hexane-nitrogen system together with the equilibrium mixing temperature T_{EQ} (see Sec. 2.3.5 for details on the calculation) for n-hexane injection total temperatures $T_{t,inj} = \{480\ \text{K}, 560\ \text{K}, 600\ \text{K}\}$. Based on the assumption that the adiabatic mixing model and vapor-liquid equilibria relations hold,

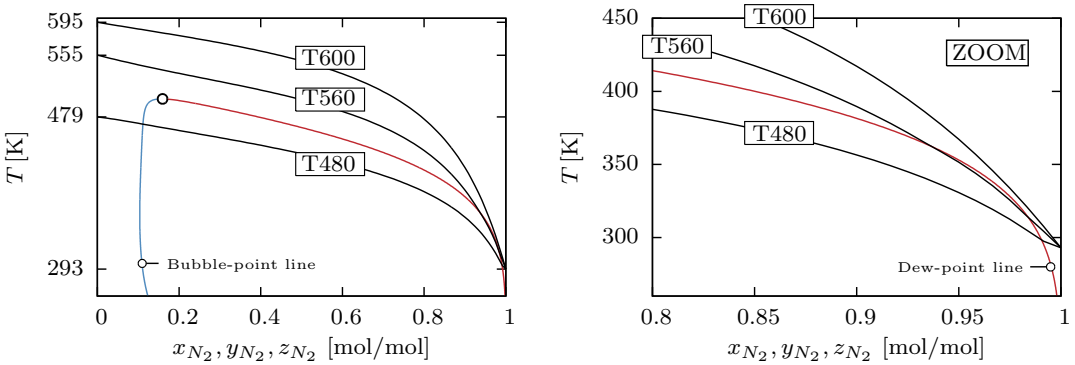

Figure A.1: Temperature-composition phase diagram for a binary n-hexane-nitrogen system at a pressure $p = 5$ MPa with equilibrium mixing temperature T_{EQ} for the cases T480, T560 and T600. The diagram was calculated with the PR EOS and $k'_{12} = 0$, see Chapter 2 for details. A MATLAB source code (`main_N2_C6H14.m`) which produces a similar figure is provided as supplementary material, see Appendix B.

we must expect two-phase phenomena for the cases T480 and T560, while case T600 should be of type dense-fluid mixing because the adiabatic mixing line does not intersect bubble- or dew-point lines. In the experiment, simultaneous shadowgraphy and elastic light scattering (ELS) measurements allow for a qualitative statement whether or not phase formation takes place.

Here, only a very brief discussion of our results will be given. For a more thorough analysis the interested reader is referred to Traxinger et al. (2017). LES results documented in this paper were generated with the numerical framework for two-phase flows developed in Chapter 2. The overall spatial extent of the computational domain is the same as for LES of ECN Spray A, see Sec. 4.4.1. Blocking and grid refinement were adjusted such that the injector diameter $D_i = 0.236$ mm is resolved with about 9 cells. The domain consists of 736 blocks with 3.76×10^6 cells. An overview of experimental and numerical boundary conditions can be found in Tab. A.1. A comparison between single-shot measurements (left) and numerical snapshots (right) is shown in Fig. A.2. Experimental images are courtesy of Steffen Baab, ITLR, University Stuttgart. Each top frame shows the experimental shadowgram together with the temperature field in the LES. Each bottom frame depicts the scaled ELS signal superimposed on the shadowgram together with the vapor volume fraction field superimposed on the temperature field. The n-hexane injection temperature is decreasing from (a) to (i). Note that the prescribed inflow temperature in the LES – which has a first-order effect on

the type of jet disintegration – is calculated on basis of an isentropic nozzle flow (see Lamanna et al. (2012) for details). Resulting static inflow temperatures at the nozzle exit $T_{e,inj}$ that are imposed as boundary condition are listed in Tab. A.1. Furthermore, the total temperature in the injector element is measured with an uncertainty of ± 2 K. Therefore, focus is put on a qualitative comparison between experiment and simulation. Consider Fig. A.2 (left column): For case T600 only minor ELS intensities are measured, which indicates that no stable phase formation took place. This conclusion can be drawn based on the very high sensitivity of the scattered light towards the thermodynamic state, i.e., single- or two-phase flow (private communication with Steffen Baab). With decreasing inflow temperature the ELS signal intensity increases in the outer shear layer of the jet. For the cases T580 - T540 we observe the highest ELS intensity several inflow-diameters downstream of injection and in the outer shear layer (meaning not on the jet centerline). For case T520 and T480 the ELS characteristics change, see Fig. A.2 (h) & (i). The highest intensity is found very close to the injector exit and closer to the jet centerline. In the LES we observe a very similar pattern. While no two-phase flow is detected for case T600, we get a first 'vapor-volume-fraction signal' for case T574 in the very outer periphery of the jet. With decreasing inflow temperature, the spatial extent of two-phase flow increases and the axial position where the outer shear layer of two-phase flow merges on the jet centerline moves upstream. Note that the vapor volume fraction is in the range 0.97 - 1, because mixture states enter and exit the two-phase region only through the dew-point line, cf. also Fig A.1. The picture changes for the cases T520 and T480. The vapor volume fraction is in the range 0 - 1 and the whole jet is in a two-phase state (the adiabatic mixing line goes through bubble- and dew-point line). For $x/D < 20$, a liquid-like core surrounded by two-phase flow can be identified. From a qualitative perspective, experimental observations can be explained in a consistent manner with the help of the LES and the adiabatic mixing model. Figure A.3 shows a comparison between averaged experimental and numerical data. In the experiment, the average was calculated on basis of 10-15 single-shots. In the LES, statistical properties have been obtained by averaging in time for about 2.5 ms (after an initial transient of 4 ms). We further present a liquid volume fraction normalized with its minimum and maximum value such that it ranges from 0 - 1 for all cases under consideration. Similar as for the instantaneous data, we observe – from a qualitative perspective – a very good agreement between measured ELS pattern and regions of two-phase flow in the LES.

Further experiments and numerical simulations are planned in the course of the *SFB TRR40 summer program 2017*, which will be held in Munich.

Table A.1: Test case definition with $T_{t,inj}$ being the nominal total temperature of n-hexane. p_{inj}, T_{ch} and p_{ch} denote the measured injection pressure, and the temperature and pressure in the chamber, respectively. Static injection temperature T_{inj} and injection velocity u are used as LES inflow boundary condition and have been calculated with the assumption of an isentropic nozzle flow.

Case	LES	Exp.	$T_{t,inj}$ [K]	p_{inj} [bar]	T_{ch} [K]	p_{ch} [bar]	$T_{e,inj}$ [K]	u [m/s]
T600	x	x	600	55.70	294.6	49.93	595.03	90.34
T580		x	580	56.50	294.6	49.98	574.64	82.53
T574	x	x	574	56.07	294.9	50.07	568.57	79.68
T570	x		570	-	-	-	564.56	77.63
T560	x	x	560	56.07	294.8	49.94	554.84	72.06
T550	x		550	-	-	-	545.73	66.49
T540	x	x	540	55.95	294.9	50.02	536.88	61.91
T520	x	x	520	55.82	294.3	49.99	518.41	56.23
T480	x	x	480	56.56	291.9	50.10	479.32	50.98

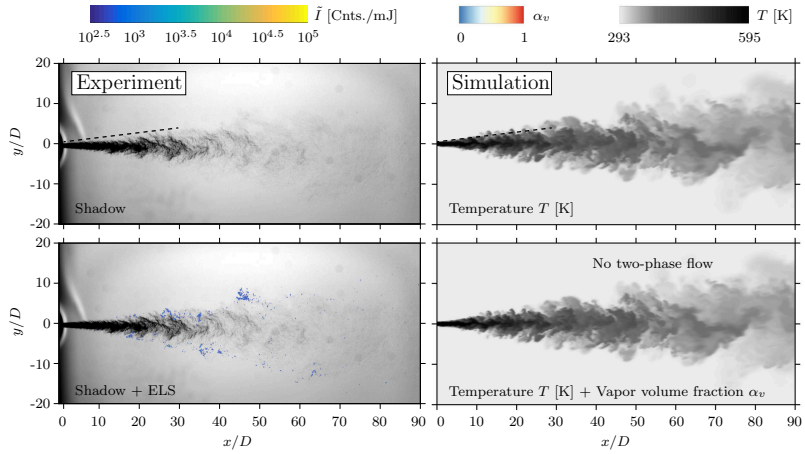

(a) Case T600.

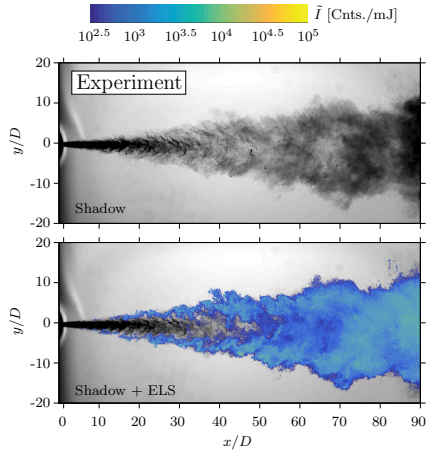

(b) Case T580.

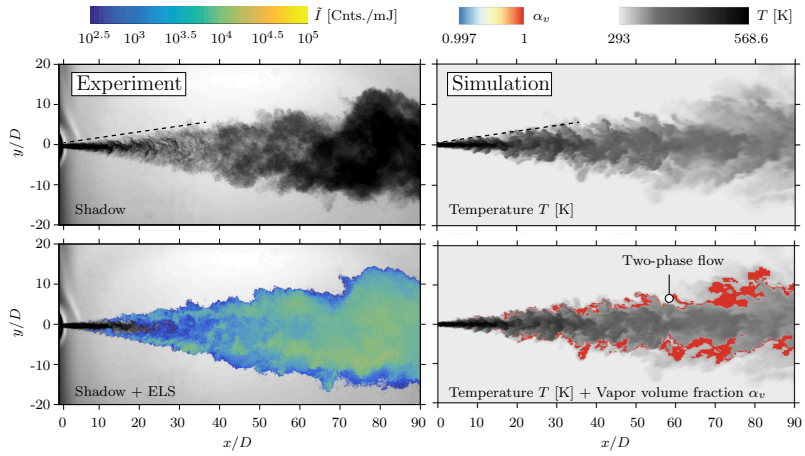

(c) Case T574.

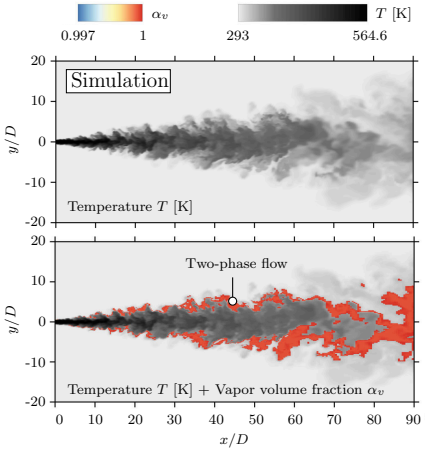

(d) Case T570.

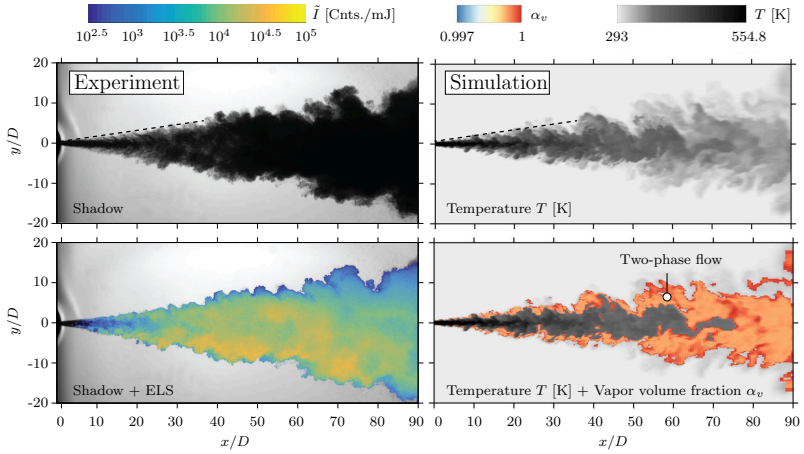

(e) Case T560.

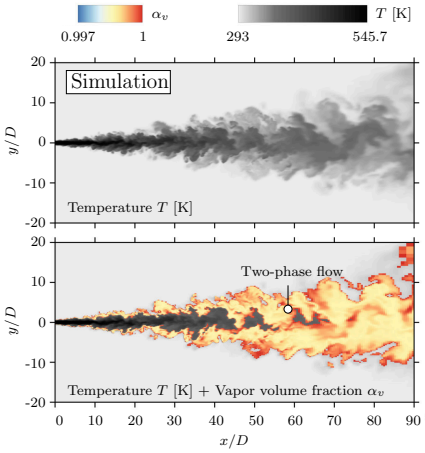

(f) Case T550.

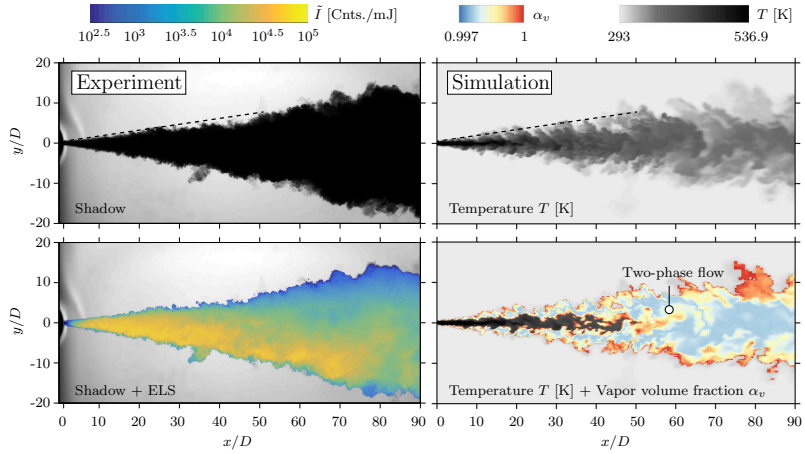

(g) Case T540.

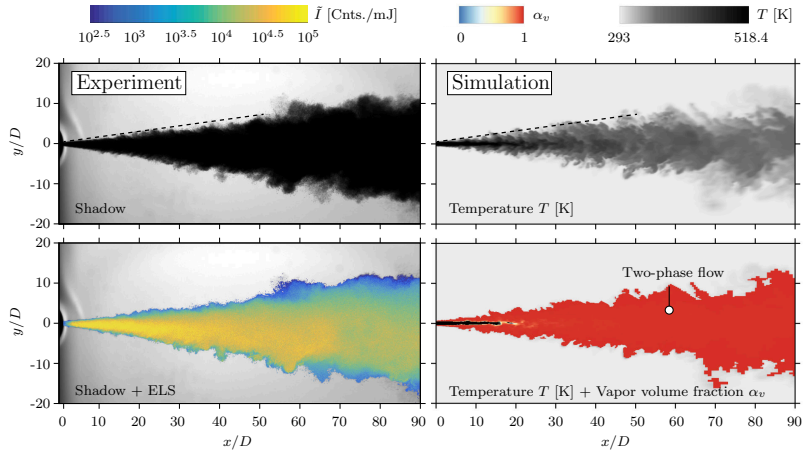

(h) Case T520.

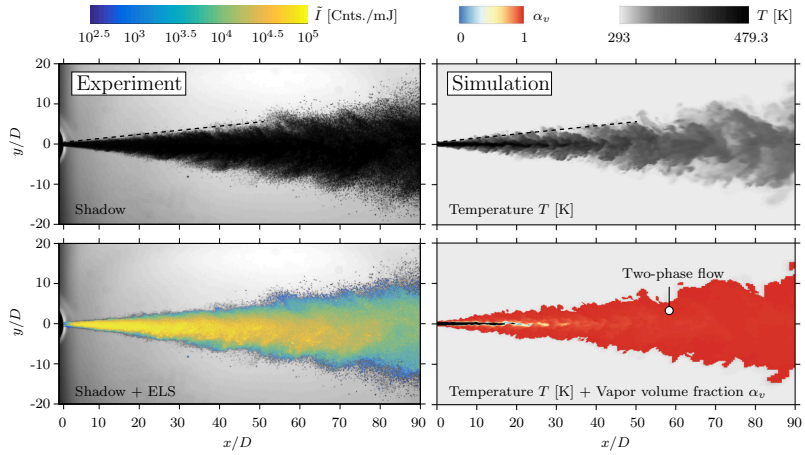

(i) Case T480.

Figure A.2: Comparison of experimental and numerical snaphots. Experimental images are courtesy of Steffen Baab, ITLR, University Stuttgart.

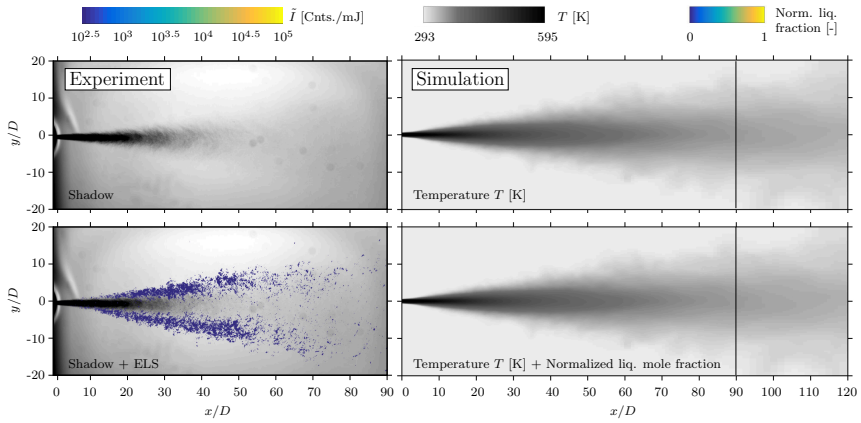

(a) Case T600.

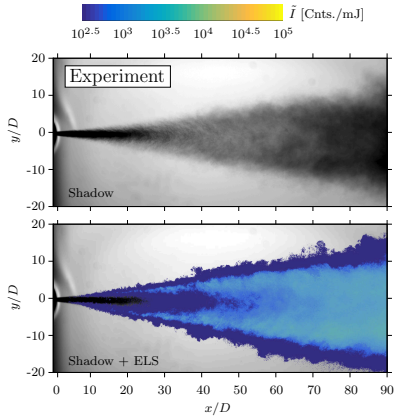

(b) Case T580.

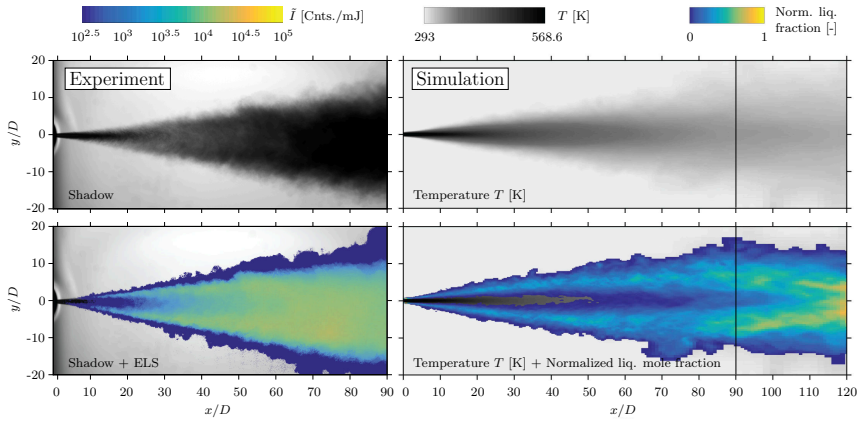

(c) Case T574.

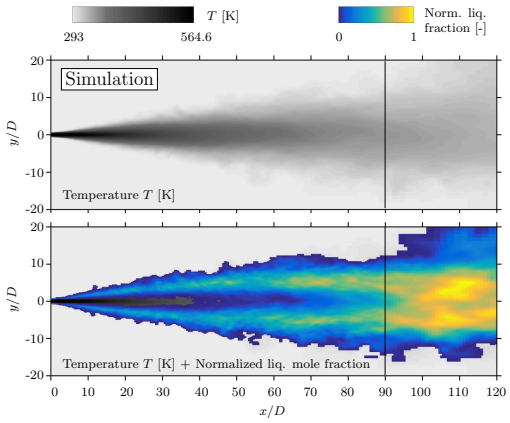

(d) Case T570.

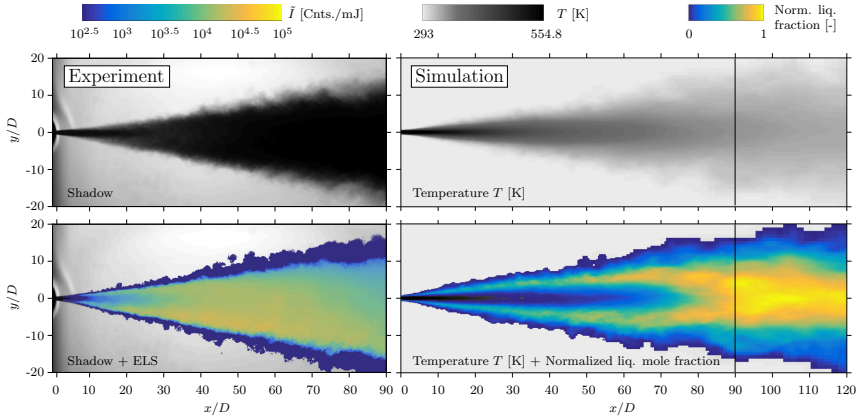

(e) Case T560.

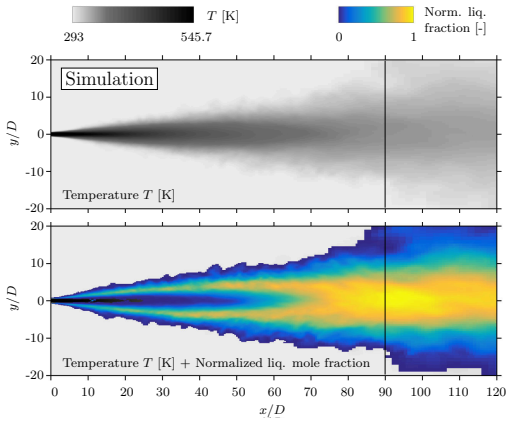

(f) Case T550.

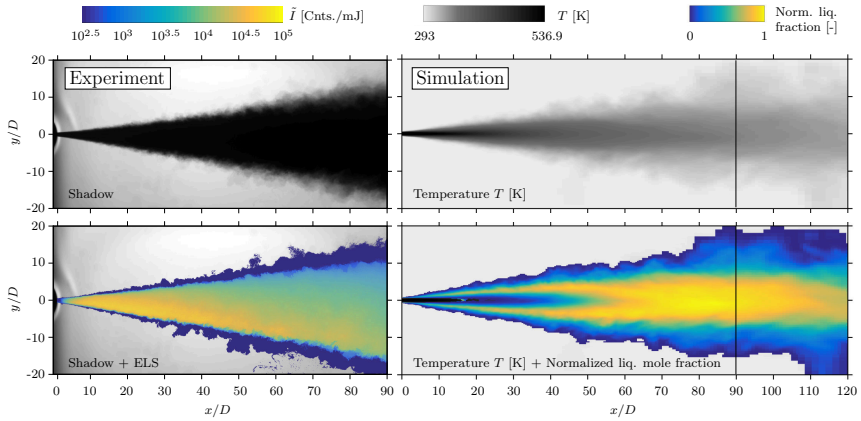

(g) Case T540.

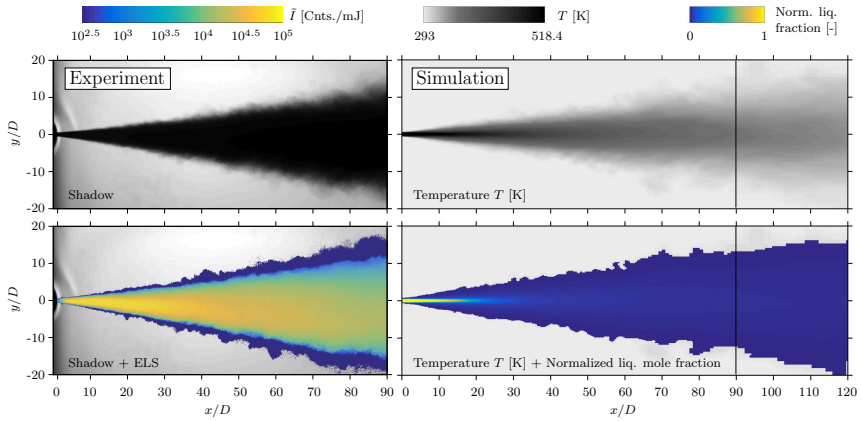

(h) Case T520.

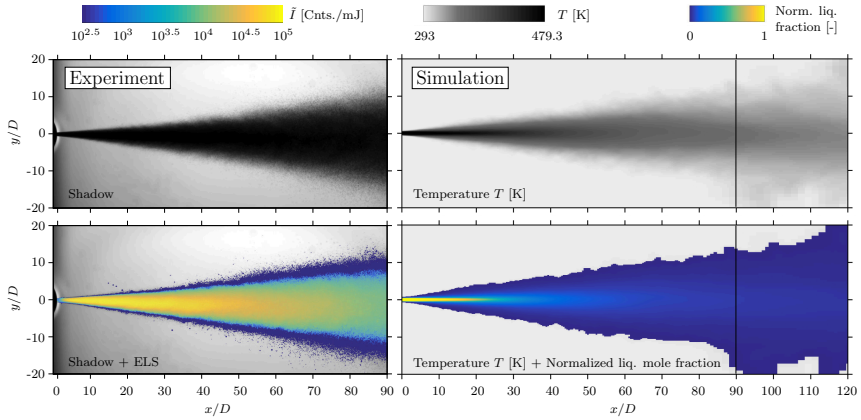

(i) Case T480.

Figure A.3: Comparison of averaged experimental and numerical data. Experimental images are courtesy of Steffen Baab, ITLR, University Stuttgart.

Appendix B

MATLAB Source Code

A collection of MATLAB scripts as supplementary material is available under `https://www.gitlab.com/jmatheis/LibThermo`. The repository contains a number of scripts that can be used to compute and plot some of the figures presented in this thesis. These scripts use elementary functions such as the *TPD* stability analysis or the isothermal two-phase flash. Thermodynamic routines in the Fortran written CFD code INCA (`http://www.inca-cfd.com/`) are based upon these MATLAB scripts. Here, only a brief description of the most important scripts and functions is given. Detailed comments and relevant literature are provided within each individual file.

Main scripts

`main_N2_H2.m` This script calculates for Oschwald's case (nitrogen and hydrogen, see Chapter 2 & 3) the frozen and equilibrium mixing temperatures T_F and T_{EQ}, cf. Fig. 2.2a. Gibbs energy of mixing, the *tpd* function, and hydrogen and nitrogen partial densities are visualized similar to Fig. 2.2c-2.2d

and Fig 3.12g.

main_N2_C12H26.m This script calculates for Spray A (nitrogen and n-dodecane, see Chapter 4) the frozen and equilibrium mixing temperatures T_F and T_{EQ}, and corresponding partial densities, cf. Fig.4.1.

main_N2_C6H14.m This script calculates for the ITLR case (nitrogen and n-hexane, see Appendix A) the frozen and equilibrium mixing temperatures T_F and T_{EQ}.

Thermodynamic functions

solveTPN.m Equilibrium calculation at specified temperature, pressure and overall composition using the successive substitution method, cf. Algorithm 4, and optionally a Newton method. Further information on the Newton method with analytical Jacobian matrix can be found in Michelsen and Mollerup (2007), Chapter 10. Flash calculations involving alternative specifications, e.g., the isenthalpic flash (Sec. 2.3.5) or isoenergetic-isochoric flash (Sec. 2.3.4), embed this function in the innermost loop.

objectiveHPN.m Objective function (not the solution) for equilibrium calculation at specified enthalpy, pressure and overall composition, cf. Sec. 2.3.5. This routine is called with MATLAB's fsolve in all main scripts to calculate the equilibrium mixing temperature T_{EQ}.

solveTPD_SSI.m / solveTPD_BFGS.m Thermodynamic stability analysis using the *TPD* analysis, see Sec. 2.3.2. Source code for the successive substitution and the BFGS-quasi-Newton algorithm are provided. The implementation follows closely the recommendations given by Hoteit and Firoozabadi (2006).

solveVol.m Volume root calculation using the generalized cubic EOS as presented in Algorithm 1.

Bibliography

R. Abgrall and S. Karni. Computations of compressible multifluids. *J. Comput. Phys.*, 169(2):594–623, 2001. doi:10.1006/jcph.2000.6685.

N. A. Adams, S. Hickel, and S. Franz. Implicit subgrid-scale modeling by adaptive deconvolution. *J. Comput. Phys.*, 200(2):412–431, 2004. doi:10.1016/j.jcp.2004.04.010.

S. Baab, F. J. Förster, G. Lamanna, and B. Weigand. Speed of sound measurements and mixing characterization of underexpanded fuel jets with supercritical reservoir condition using laser-induced thermal acoustics. *Exp. Fluids*, 57(11): 172, 2016. doi:10.1007/s00348-016-2252-3.

B. Balaji, V. Raghavan, K. Ramamurthi, and G. Gogos. A numerical study of evaporation characteristics of spherical n-dodecane droplets in high pressure nitrogen environment. *Phys. Fluids*, 23(6):063601, 2011. doi:10.1063/1.3599700.

D. T. Banuti and K. Hannemann. The absence of a dense potential core in supercritical injection: A thermal break-up mechanism. *Phys. Fluids*, 28(3):035103, 2016. doi:10.1063/1.4943038.

J. Bellan. Supercritical (and subcritical) fluid behavior and modeling: drops, streams, shear and mixing layers, jets and sprays. *Prog. Energy Combust. Sci.*, 26:329–366, 2000. doi:10.1016/S0360-1285(00)00008-3.

J. Bellan. Theory, modeling and analysis of turbulent supercritical mixing. *Combust. Sci. Technol.*, 178(1-3):253–281, 2006. doi:10.1080/00102200500292241.

R. Branam and W. Mayer. Characterization of cryogenic injection at supercritical pressure. *J. Propul. Power*, 19(3):342–355, 2003. doi:10.2514/2.6138.

M. Castier. Solution of the isochoric–isoenergetic flash problem by direct entropy maximization. *Fluid Phase Equilibr.*, 276(1):7–17, 2009. doi:10.1016/j.fluid.2008.10.005.

B. Chehroudi. Recent experimental efforts on high-pressure supercritical injection for liquid rockets and their implications. *International Journal of Aerospace Engineering*, 2012:1–31, 2012. doi:10.1155/2012/121802.

B. Chehroudi, R. Cohn, D. Talley, and A. Badakhshan. Raman scattering measurements in the initial region of sub-and supercritical jets. In *36th AIAA/ASME/SAE/ASEE Joint Propulsion Conference and Exhibit*, 2000. doi:10.2514/6.2000-3392.

B. Chehroudi, D. Talley, and E. Coy. Visual characteristics and initial growth rates of round cryogenic jets at subcritical and supercritical pressures. *Phys. Fluids*, 14(2):850–861, 2002. doi:10.1063/1.1430735.

T. H. Chung, M. Ajlan, L. L. Lee, and K. E. Starling. Generalized multiparameter correlation for nonpolar and polar fluid transport properties. *Ind. Eng. Chem. Res.*, 27(4):671–679, 1988. doi:10.1021/ie00076a024.

M. Cismondi and J. Mollerup. Development and application of a three-parameter RK–PR equation of state. *Fluid Phase Equilibr.*, 232(1):74–89, 2005. doi:10.1016/j.fluid.2005.03.020.

C. Crua, J. Manin, and L. M. Pickett. Transition from droplet evaporation to miscible mixing at diesel engine conditions. In *ICLASS 2015, 13th Triennial International Conference on Liquid Atomization and Spray Systems, Tainan, Taiwan*, 2015.

R. N. Dahms and J. C. Oefelein. On the transition between two-phase and single-phase interface dynamics in multicomponent fluids at supercritical pressures. *Phys. Fluids*, 25(9):092103, 2013. doi:10.1063/1.4820346.

R. N. Dahms, J. Manin, L. M. Pickett, and J. C. Oefelein. Understanding high-pressure gas-liquid interface phenomena in diesel engines. *P. Combust. Inst.*, 34 (1):1667–1675, 2013. doi:10.1016/j.proci.2012.06.169.

D. W. Davis and B. Chehroudi. Measurements in an acoustically driven coaxial jet under sub-, near-, and supercritical conditions. *J. Propul. Power*, 23(2): 364–374, 2007. doi:10.2514/1.19340.

M. Decker, A. Schik, U. E. Meier, and W. Stricker. Quantitative raman imaging investigations of mixing phenomena in high-pressure cryogenic jets. *Appl. Opt.*, 37(24):5620–5627, 1998. doi:10.1364/AO.37.005620.

J. R. Elliott and C. T. Lira. *Introductory Chemical Engineering Thermodynamics*. Prentice Hall, 2012.

L. S. Eubanks. *Vapor-liquid equilibria in the system hydrogen-nitrogen-carbon monoxide*. PhD thesis, 1957. URL `http://hdl.handle.net/1911/18254`.

Z. Falgout, M. Rahm, D. Sedarsky, and M. Linne. Gas/fuel jet interfaces under high pressures and temperatures. *Fuel*, 168:14–21, 2016. doi:10.1016/j.fuel.2015.11.061.

R. P. Fedkiw, X.-D. Liu, and S. Osher. A general technique for eliminating spurious oscillations in conservative schemes for multiphase and multispecies euler equations. *Int. J. Nonlin. Sci. Num.*, 3(2):99–105, 2002. doi:10.1515/IJNSNS.2002.3.2.99.

A. Firoozabadi. *Thermodynamics of Hydrocarbon Reservoirs*. McGraw-Hill, 1999.

P. Gaillard, V. Giovangigli, and L. Matuszewski. A diffuse interface Lox/hydrogen transcritical flame model. *Combust. Theor. Model*, 20(3):486–520, 2016a. doi:10.1080/13647830.2016.1150518.

P. Gaillard, C. Le Touze, and L. Matuszewski. Numerical simulation of cryogenic injection in rocket engine combustion chambers. *Journal AerospaceLab*, 16(11): 1–11, 2016b. URL `https://hal.archives-ouvertes.fr/hal-01369627/`.

E. Garnier, N. A. Adams, and P. Sagaut. *Large Eddy Simulation for Compressible Flows*. Springer-Verlag Berlin Heidelberg New York, 2009.

A. Gnanaskandan and J. Bellan. Numerical simulation of jet injection and species mixing under high-pressure conditions. *J. Phys.: Conf. Ser.*, 821:012020, 2017. doi:10.1088/1742-6596/821/1/012020.

M. G. Gonikberg, W. G. Fastovskii, and J. G. Gurvich. *Acta Physicochim. U.R.S.S.*, 11:865–882, 1939a.

M. G. Gonikberg, W. G. Fastovskii, and J. G. Gurvich. *Zh. Fiz. Khim*, 13(11): 1669–1679, 1939b.

E. Goos, A. Burcat, and B. Ruscic. Third Millennium Ideal Gas and Condensed Phase Thermochemical Database for Combustion, 2009. URL `http://burcat.technion.ac.il/dir/`.

F. Gorelli, M. Santoro, T. Scopigno, M. Krisch, and G. Ruocco. Liquid-like behavior of supercritical fluids . *Phys. Rev. Lett.*, 97(24):245702, 2006. doi:10.1103/PhysRevLett.97.245702.

S. Gottlieb and C. Shu. Total variation diminishing Runge-Kutta schemes. *Math. Comput.*, 67(221):73–85, 1998. doi:10.1090/S0025-5718-98-00913-2.

L. Hakim, G. Lacaze, and J. C. Oefelein. Large eddy simulation of autoignition transients in a model diesel injector configuration. *SAE Int. J. Fuels Lubr.*, 9 (1):165–176, 2016. doi:10.4271/2016-01-0872.

S. Hickel, N. A. Adams, and J. A. Domaradzki. An adaptive local deconvolution method for implicit LES. *J. Comput. Phys.*, 213(1):413–436, 2006. doi:10.1016/j.jcp.2005.08.017.

S. Hickel, C. P. Egerer, and J. Larsson. Subgrid-scale modeling for implicit large eddy simulation of compressible flows and shock-turbulence interaction. *Phys. Fluids*, 26(10):106101, 2014. doi:10.1063/1.4898641.

J. P. Hickey and M. Ihme. Large eddy simulation of supercritical mixing and combustion for rocket applications. In *52nd AIAA Aerospace Science Meeting*, 2014. doi:10.2514/6.2014-0138.

J. P. Hickey, P. Ma, M. Ihme, and S. Thakur. Large eddy simulation of shear coaxial rocket injector: real fluid effects. In *49th AIAA/ASME/SAE/ASEE Joint Propulsion Conference*, 2013. doi:10.2514/6.2013-4071.

H. Hoteit and A. Firoozabadi. Simple phase stability-testing algorithm in the reduction method. *AIChE J.*, 52(8):2909–2920, 2006. doi:10.1002/aic.10908.

M. Jangi, R. Solsjo, B. Johansson, and X.-S. Bai. On large eddy simulation of diesel spray for internal combustion engines. *Int. J. Heat Fluid Flow*, 53:68–80, 2015. doi:10.1016/j.ijheatfluidflow.2015.02.002.

S. Kawai, H. Terashima, and H. Negishi. A robust and accurate numerical method for transcritical turbulent flows at supercritical pressure with an arbitrary equation of state. *J. Comput. Phys.*, 300:116–135, 2015. doi:10.1016/j.jcp.2015.07.047.

S.-K. Kim, H.-S. Choi, and Y. Kim. Thermodynamic modeling based on a generalized cubic equation of state for kerosene/LOx rocket combustion. *Combust. Flame*, 159(3):1351–1365, 2012. doi:10.1016/j.combustflame.2011.10.008.

E. Knudsen, E. M. Doran, V. Mittal, J. Meng, and W. Spurlock. Compressible Eulerian needle-to-target large eddy simulations of a diesel fuel injector. *P. Combust. Inst.*, 32(2):2459–2466, 2016. doi:10.1016/j.proci.2016.08.016.

P. H. V. Konynenburg and R. L. Scott. Critical lines and phase equilibria in binary van der waals mixtures. *Philos. Trans. R. Soc. London, Ser. A*, 298 (1442):495–540, 1980. doi:10.1098/rsta.1980.0266.

O. Kunz and W. Wagner. The GERG-2008 wide-range equation of state for natural gases and other mixtures: an expansion of GERG-2004. *J. Chem. Eng. Data*, 57(11):3032–3091, 2012. doi:10.1021/je300655b.

G. Lacaze, A. Misdariis, A. Ruiz, and J. C. Oefelein. Analysis of high-pressure diesel fuel injection processes using LES with real-fluid thermodynamics and transport. *P. Combust. Inst.*, 35(2):1603–1611, 2015. doi:10.1016/j.proci.2014.06.072.

G. Lamanna, E. Oldenhof, S. Baab, I. Stotz, and B. Weigand. Disintegration regimes near the critical point. In *18th AIAA/3AF International Space Planes and Hypersonic Systems and Technologies Conference*. American Institute of Aeronautics and Astronautics, 2012. doi:10.2514/6.2012-5914.

E. W. Lemmon, M. L. Huber, and M. O. McLinden. NIST Standard Reference Database 23: Reference Fluid Thermodynamic and Transport Properties-REFPROP, Version 9.1. 2013.

A. Leonard. Energy cascade in large-eddy simulations of turbulent fluid flows. *Advances in geophysics*, 18:237–248, 1975. doi:10.1016/S0065-2687(08)60464-1.

S. P. Lin and R. D. Reitz. Drop and spray formation from a liquid jet. *Annu. Rev. Fluid Mech.*, 30(1):85–105, 1998. doi:10.1146/annurev.fluid.30.1.85.

P. C. Ma, Y. Lv, and M. Ihme. An entropy-stable hybrid scheme for simulations of transcritical real-fluid flows. *J. Comp. Phys*, 340:330–357, 2017. doi:10.1016/j.jcp.2017.03.022.

J. Manin, M. Bardi, and L. M. Pickett. Evaluation of the liquid length via diffused back-illumination imaging in vaporizing diesel sprays. In *The Eighth International Conference on Modeling and Diagnostics for Advanced Engine Systems (COMODIA)*, pages 665–673, 2012.

J. Manin, M. Bardi, L. M. Pickett, R. N. Dahms, and J. C. Oefelein. Microscopic investigation of the atomization and mixing processes of diesel sprays injected into high pressure and temperature environments. *Fuel*, 134:531–543, 2014. doi:10.1016/j.fuel.2014.05.060.

J. Manin, L. Pickett, and C. Crua. Microscopic observation of miscible mixing in sprays at elevated temperatures and pressures. *ILASS Americas 27th Annual Conference on Liquid Atomization and Spray Systems*, 2015. URL `http://www.ilass.org/2/conferencepapers/93_2015.pdf`.

J. Manin, M. Bardi, L. Pickett, and R. Payri. Boundary condition and fuel composition effects on injection processes of high-pressure sprays at the microscopic level. *Int. J. of Multiphas. Flow*, 83:267–278, 2016. doi:10.1016/j.ijmultiphaseflow.2015.12.001.

M. Masquelet. *Large-eddy simulations of high-pressure shear coaxial flows relevant for H2/O2 rocket engines*. PhD thesis, Georgia Institute of Technology, 2013. URL `http://hdl.handle.net/1853/47522`.

M. Masquelet, N. Guézennec, and S. Menon. Numerical studies of mixing and flame-turbulence interactions in shear coaxial injector flows under trans-critical conditions. In *50th AIAA Aerospace Sciences Meeting including the New Horizons Forum and Aerospace Exposition*, 2012. doi:10.2514/6.2012-1269.

J. Matheis and S. Hickel. On the transition between regular and irregular shock patterns of shock-wave/boundary-layer interactions. *J. Fluid Mech.*, 776:200–234, 2015. doi:10.1017/jfm.2015.319.

J. Matheis and S. Hickel. Multi-component vapor-liquid equilibrium model for LES and application to ECN Spray A. In *Proceedings of the 2016 Summer Program, Center for Turbulence Research, Stanford University*, 2016. URL `https://stanford.app.box.com/s/bvsyzo9chvekvtcbvabcxzvqcfg5otyt`.

J. Matheis and S. Hickel. Multi-component vapor-liquid equilibrium model for LES of high-pressure fuel injection and application to ECN Spray A. *Int. J. of Multiphas. Flow*, 99:294–311, 2018.

J. Matheis, H. Müller, M. Pfitzner, and S. Hickel. Large-eddy simulation of cryogenic coaxial LN2/GH2 injection under supercritical pressures. In *Ninth International Symposium on Turbulence and Shear Flow Phenomena (TSFP-9)*, Melbourne, 2015. URL `http://www.tsfp-conference.org/proceedings/2015/v3/8C-5.pdf`.

J. Matheis, H. Müller, C. Lenz, M. Pfitzner, and S. Hickel. Volume translation methods for real-gas computational fluid dynamics simulations. *J. Supercrit. Fluids*, 107:422–432, 2016. doi:10.1016/j.supflu.2015.10.004.

W. Mayer, A. Schik, C. Schweitzer, and M. Schaffler. Injection and mixing processes in high pressure LOX/GH2 rocket combustors. In *32nd Joint Propulsion Conference and Exhibit*, 1996. doi:10.2514/6.1996-2620.

W. Mayer, J. Telaar, R. Branam, G. Schneider, and J. Hussong. Raman measurements of cryogenic injection at supercritical pressure. *Heat Mass Transfer*, 39 (8):709–719, 2003. doi:10.1007/s00231-002-0315-x.

W. O. H. Mayer and R. Branam. Atomization characteristics on the surface of a round liquid jet. *Exp. Fluids*, 36:528–539, 2004. doi:10.1007/s00348-003-0675-0.

W. O. H. Mayer and J. J. Smith. Fundamentals of supercritical mixing and combustion of cryogenic propellants. In M. Popp, J. Hulka, V. Yang, and M. Habiballah, editors, *Progress In Astronautics and Aeronautics: Liquid Rocket Thrust Chambers*, pages 339–367. AIAA, 2004. doi:10.2514/5.9781600866760.0339.0367.

W. O. H. Mayer, A. H. Schik, B. Vielle, C. Chauveau, I. Gökalp, D. G. Talley, and R. D. Woodward. Atomization and breakup of cryogenic propellants under high-pressure subcritical and supercritical conditions. *J. Propul. Power*, 14(5): 835–842, 1998. doi:10.2514/2.5348.

M. Meijer, B. Somers, J. Johnson, J. Naber, S.-Y. Lee, L. M. Malbec, G. Bruneaux, L. M. Pickett, M. Bardi, R. Payri, and T. Bazyn. Engine Combustion Network (ECN): Characterization and comparison of boundary conditions for different combustion vessels. *Atomization Sprays*, 22(9):777–806, 2012. doi:10.1615/AtomizSpr.2012006083.

H. Meng and V. Yang. A unified treatment of general fluid thermodynamics and its application to a preconditioning scheme. *J. Comput. Phys.*, 189(1):277–304, 2003. doi:10.1016/S0021-9991(03)00211-0.

M. L. Michelsen. The isothermal flash problem. Part II. Phase-split calculation. *Fluid Phase Equilibr.*, 9(1):21–40, 1982a. doi:10.1016/0378-3812(82)85002-4.

M. L. Michelsen. The isothermal flash problem. Part I. Stability. *Fluid Phase Equilibr.*, 9(1):1–19, 1982b. doi:10.1016/0378-3812(82)85001-2.

M. L. Michelsen and J. M. Mollerup. *Thermodynamic Models: Fundamentals & Computational Aspects*. Tie-Line Publications, 2007.

R. S. Miller, K. G. Harstad, and J. Bellan. Direct numerical simulations of supercritical fluid mixing layers applied to heptane–nitrogen. *J. Fluid Mech.*, 436(6): 1–39, 2001. doi:10.1017/S0022112001003895.

H. Müller. *Simulation turbulenter nicht-vorgemischter Verbrennung bei überkritischen Drücken*. PhD thesis, Universität der Bundeswehr München, 2016. URL `https://athene-forschung.unibw.de/doc/115393/115393.pdf`.

H. Müller and M. Pfitzner. Large-eddy simulation of transcritical LOx/CH4 jet flames. In *6th EUCASS*, 2015.

H. Müller, M. Pfitzner, J. Matheis, and S. Hickel. Large-eddy simulation of coaxial LN2/GH2 injection at trans- and supercritical conditions. *J. Propul. Power*, 32 (1):46–56, 2015. doi:10.2514/1.B35827.

H. Müller, C. A. Niedermeier, J. Matheis, M. Pfitzner, and S. Hickel. Large-eddy simulation of nitrogen injection at trans- and supercritical conditions. *Phys. Fluids*, 28(1):015102, 2016. doi:10.1063/1.4937948.

C. K. Muthukumaran and A. Vaidyanathan. Experimental study of elliptical jet from sub to supercritical conditions. *Phys. Fluids*, 26(4):044104, 2014. doi:10.1063/1.4871483.

C. K. Muthukumaran and A. Vaidyanathan. Experimental study of elliptical jet from supercritical to subcritical conditions using planar laser induced fluorescence. *Phys. Fluids*, 27(3):034109, 2015. doi:10.1063/1.4916344.

J. Naber and D. L. Siebers. Effects of Gas Density and Vaporization on Penetration and Dispersion of Diesel Sprays. *SAE Technical Paper 960034*, 1996. doi:10.4271/960034.

J. Newman and T. Brzustowski. Behavior of a liquid jet near the thermodynamic critical region. *AIAA J.*, 9(8):1595–1602, 1971. doi:10.2514/3.49962.

J. C. Oefelein and V. Yang. Modeling high-pressure mixing and combustion processes in liquid rocket engines. *J. Propul. Power*, 14(5):843–857, 1998. doi:10.2514/2.5349.

N. A. Okong'o and J. Bellan. Direct numerical simulation of a transitional supercritical binary mixing layer: heptane and nitrogen. *J. Fluid Mech.*, 464(1):1–34, 2002a. doi:10.1017/S0022112002008480.

N. A. Okong'o and J. Bellan. Consistent boundary conditions for multicomponent real gas mixtures based on characteristic waves. *J. Comput. Phys.*, 176:330–344, 2002b. doi:10.1006/jcph.2002.6990.

N. A. Okong'o and J. Bellan. Real-gas effects on mean flow and temporal stability of binary-species mixing layers. *AIAA J.*, 41(12):2429–2443, 2003. doi:10.2514/2.6842.

N. A. Okong'o, K. G. Harstad, and J. Bellan. Direct numerical simulations of LOX/H2 temporal mixing layers under supercritical conditions. In *2nd International Workshop on Rocket Combustion Modeling: Atomization, Combustion and Heat Transfer*, Lampoldshausen, 2001. URL `http://www.dtic.mil/dtic/tr/fulltext/u2/p012368.pdf`.

F. Örley, S. Hickel, S. J. Schmidt, and N. A. Adams. Large-Eddy Simulation of turbulent, cavitating fuel flow inside a 9-hole Diesel injector including needle movement. *Int. J. Engine Res.*, 18(3):195–211, 2017. doi:10.1177/1468087416643901.

M. Oschwald and A. Schik. Supercritical nitrogen free jet investigated by spontaneous Raman scattering. *Exp. Fluids*, 27(6):497–506, 1999. doi:10.1007/s003480050374.

M. Oschwald, A. Schik, M. Klar, and W. Mayer. Investigation of coaxial LN2/GH2-injection at supercritical pressure by spontaneous Raman scattering . In *35th AIAA/ASME/SAE/ASEE Joint Propulsion Conference and Exhibit 20-24 June 1999 Los Angeles, California*, 1999. doi:10.2514/6.1999-2887.

M. Oschwald, J. J. Smith, R. Branam, J. Hussong, A. Schik, B. Chehroudi, and D. Talley. Injection of fluids into supercritical environments. *Combust. Sci. Technol.*, 178(1-3):49–100, 2006. doi:10.1080/00102200500292464.

R. Payri, J. Garcia-Oliver, M. Bardi, and J. Manin. Fuel temperature influence on diesel sprays in inert and reacting conditions. *Appl. Therm. Eng.*, 35:185–195, 2012. doi:10.1016/j.applthermaleng.2011.10.027.

Y. Pei, E. R. Hawkes, S. Kook, G. M. Goldin, and T. Lu. Modelling n-dodecane spray and combustion with the transported probability density function method. *Combust. Flame*, 162(5):2006–2019, 2015a. doi:10.1016/j.combustflame.2014.12.019.

Y. Pei, S. Som, E. Pomraning, P. K. Senecal, S. A. Skeen, J. Manin, and L. M. Pickett. Large eddy simulation of a reacting spray flame with multiple realizations under compression ignition engine conditions. *Combust. Flame*, 162(12): 4442–4455, 2015b. doi:10.1016/j.combustflame.2015.08.010.

D. Y. Peng and D. B. Robinson. A new two-constant equation of state. *Ind. Eng. Chem. Fund.*, 15:59–64, 1976. doi:10.1021/i160057a011.

X. Petit, G. Ribert, G. Lartigue, and P. Domingo. Large-eddy simulation of supercritical fluid injection. *J. Supercrit. Fluids*, 84:61–73, 2013. doi:10.1016/j.supflu.2013.09.011.

L. M. Pickett, C. L. Genzale, J. Manin, L. M. Malbec, and L. Hermant. Measurement uncertainty of liquid penetration in evaporating diesel sprays. In *Proceedings of the 23rd Annual Conference on Liquid Atomization and Spray Systems*, 2011a.

L. M. Pickett, J. Manin, C. L. Genzale, D. L. Siebers, M. P. B. Musculus, and C. A. Idicheria. Relationship between diesel fuel spray vapor penetration/dispersion and local fuel mixture fraction. *SAE Int. J. Engines*, 4(1):764–799, 2011b. doi:10.4271/2011-01-0686.

L. M. Pickett, C. L. Genzale, and J. Manin. Uncertainty quantification for liquid penetration of evaporating sprays at diesel-like conditions. *Atomization Sprays*, 25(5):425–452, 2015. doi:10.1615/AtomizSpr.2015010618.

B. Poling, J. Prausnitz, and J. O' Connell. *The Properties of Gases and Liquids*. McGraw-Hill, fifth edition, 2000.

S. B. Pope. *Turbulent Flows*. Cambridge University Press, 2000.

J. M. Prausnitz, R. N. Lichtenthaler, and E. G. de Azevedo. *Molecular Thermodynamics of Fluid-Phase Equilibria*. Pearson Education, 1998.

W. H. Press, S. A. Teukolsky, W. T. Vetterling, and B. P. Flannery. *Numerical Recipes in Fortran 77*. The Art of Scientific Computing. Cambridge University Press, second edition, 2002.

L. Qiu. *Development of a Phase Stability-Based Fuel Condensation Model for Advanced Low Temperature Combustion Engines*. PhD thesis, University of Wisconson-Madison, 2014.

L. Qiu and R. D. Reitz. Simulation of supercritical fuel injection with condensation. *Int. J. Heat Mass Tran.*, 79:1070–1086, 2014. doi:10.1016/j.ijheatmasstransfer.2014.08.081.

L. Qiu and R. D. Reitz. An investigation of thermodynamic states during high-pressure fuel injection using equilibrium thermodynamics. *Int. J. of Multiphas. Flow*, 72:24–38, 2015. doi:10.1016/j.ijmultiphaseflow.2015.01.011.

L. Qiu, Y. Wang, Q. Jiao, H. Wang, and R. D. Reitz. Development of a thermodynamically consistent, robust and efficient phase equilibrium solver and its validations. *Fuel*, 105:1–16, 2014a. doi:10.1016/j.fuel.2013.06.039.

L. Qiu, Y. Wang, and R. D. Reitz. Multiphase dynamic flash simulations using entropy maximization and application to compressible flow with phase change. *AIChE J.*, 60(8):3013–3024, 2014b. doi:10.1002/aic.14519.

R. C. Reid, J. M. Prausnitz, and B. E. Poling. *The Properties of Gases and Liquids*. McGraw-Hill, fourth edition, 1987.

J. S. Rowlinson and F. L. Swinton. *Liquids and Liquid Mixtures*. Butterworths Monographs in Chemistry. Butterworth-Heinemann, 2013.

A. Roy, C. Joly, and C. Segal. Disintegrating supercritical jets in a subcritical environment. *J. Fluid Mech.*, 717:193–202, 2013. doi:10.1017/jfm.2012.566.

A. Ruiz. *Unsteady numerical simulations of transcritical turbulent combustion in liquid rocket engines*. PhD thesis, Institut National Polytechnique de Toulouse, 2012. URL `http://oatao.univ-toulouse.fr/6978/`.

S. Saha and J. Carroll. The isoenergetic-isochoric flash. *Fluid Phase Equilibr.*, 138 (1-2):23–41, 1997. doi:10.1016/S0378-3812(97)00151-9.

R. Saurel, F. Petitpas, and R. Abgrall. Modelling phase transition in metastable liquids: application to cavitating and flashing flows. *J. Fluid Mech.*, 607:313–350, 2008. doi:10.1017/S0022112008002061.

T. Schmitt, L. Selle, A. Ruiz, and B. Cuenot. Large-eddy simulation of supercritical-pressure round jets . *AIAA J.*, 48(9):2133–2144, 2010. doi:10.2514/1.J050288.

T. Schmitt, Y. Méry, M. Boileau, and S. Candel. Large-eddy simulation of oxygen/methane flames under transcritical conditions. *P. Combust. Inst.*, 33(1): 1383–1390, 2011. doi:10.1016/j.proci.2010.07.036.

T. Schmitt, J. Rodriguez, I. A. Leyva, and S. Candel. Experiments and numerical simulation of mixing under supercritical conditions. *Phys. Fluids*, 24(5):055104, 2012. doi:10.1063/1.3701374.

C. Segal and S. A. Polikhov. Subcritical to supercritical mixing. *Phys. Fluids*, 20 (5):052101, 2008. doi:10.1063/1.2912055.

M. J. Seidl, M. Aigner, R. Keller, and P. Gerlinger. CFD simulations of turbulent nonreacting and reacting flows for rocket engine applications. *J. Supercrit. Fluids*, 121:63–77, 2017. doi:10.1016/j.supflu.2016.10.017.

L. Selle and T. Schmitt. Large-eddy simulation of single-species flows under supercritical thermodynamic conditions. *Combust. Sci. Technol.*, 182(4-6):392–404, 2010. doi:10.1080/00102200903462664.

L. Selle, N. A. Okong'o, J. Bellan, and K. G. Harstad. Modelling of subgrid-scale phenomena in supercritical transitional mixing layers: an a priori study. *J. Fluid Mech.*, 593:57–91, 2007. doi:10.1017/S0022112007008075.

P. Senecal and E. Pomraning. Large eddy simulation of vaporizing sprays considering multi-injection averaging and grid-convergent mesh resolution. *J. Eng. Gas Turbines Power*, 136(11):111504, 2014. doi:10.1115/1.4027449.

A. Shavit and C. Gutfinger. *Thermodynamics: From Concepts to Applications (Second Edition)*. CRC Press Taylor & Francis Group, 2008.

F. A. Shtekkel and N. M. Tsinn. Determination of the liquid-vapor composition diagram of the methane-nitrogen-hydrogen system (in Russian). *Zh.Khim.Prom.*, 16(8):24–28, 1939.

D. L. Siebers. Scaling liquid-phase fuel penetration in diesel sprays based on mixing-limited vaporization. *SAE technical paper 1999-01-0528*, 1999. doi:10.4271/1999-01-0528.

G. G. Simeoni, T. Bryk, F. A. Gorelli, M. Krisch, G. Ruocco, M. Santoro, and T. Scopigno. The Widom line as the crossover between liquid-like and gas-like behaviour in supercritical fluids. *Nat. Phys.*, 6(7):503–507, 2010. doi:10.1038/nphys1683.

G. Soave. Equilibrium constants from a modified Redlich-Kwong equation of state. *Chemical Engineering Science*, 27:1197–1203, 1972. doi:10.1016/0009-2509(72)80096-4.

A. M. Star, J. R. Edwards, K.-C. Lin, S. Cox-Stouffer, and T. A. Jackson. Numerical simulation of injection of supercritical ethylene into nitrogen. *J. Propul. Power*, 22(4):809–819, 2006. doi:10.2514/1.16621.

W. B. Streett and J. Calado. Liquid-vapour equilibrium for hydrogen + nitrogen at temperatures from 63 to 110 K and pressures to 57 MPa. *J. Chem. Thermodyn.*, 10(11):1089–1100, 1978. doi:10.1016/0021-9614(78)90083-6.

H. Tani, S. Teramoto, and K. Okamoto. High-speed observations of cryogenic single and coaxial jets under subcritical and transcritical conditions. *Exp. Fluids*, 56 (4):56–85, 2015. doi:10.1007/s00348-015-1956-0.

E. S. Taşkinoğlu and J. Bellan. A posteriori study using a DNS database describing fluid disintegration and binary-species mixing under supercritical pressure: heptane and nitrogen. *J. Fluid Mech.*, 645:211, 2010. doi:10.1017/S0022112009992606.

E. S. Taşkinoğlu and J. Bellan. Subgrid-scale models and large-eddy simulation of oxygen stream disintegration and mixing with a hydrogen or helium stream at supercritical pressure. *J. Fluid Mech.*, 679:156–193, 2011. doi:10.1017/jfm.2011.130.

J. Telaar, G. Schneider, and W. Mayer. Experimental investigation of breakup of turbulent liquid jets. In *ILASS*, pages VI.9.1–VI.9.6, Darmstadt, 2000.

H. Terashima and M. Koshi. Approach for simulating gas–liquid-like flows under supercritical pressures using a high-order central differencing scheme. *J. Comput. Phys.*, 231(20):6907–6923, 2012. doi:10.1016/j.jcp.2012.06.021.

H. Terashima and M. Koshi. Unique characteristics of cryogenic nitrogen jets under supercritical pressures. *J. Propul. Power*, 29(6):1328–1336, 2013. doi:10.2514/1.B34942.

H. Terashima and M. Koshi. Numerical study on mixing characteristics of coaxial cryogenic N2/H2 injection under supercritical pressure. In *52nd Aerospace Sciences Meeting*, 2014. doi:10.2514/6.2014-0307.

H. Terashima and M. Koshi. Corrigendum to "Approach for simulating gas–liquid-like flows under supercritical pressures using a high-order central differencing scheme" [J. Comput. Phys. 231 (20) (2012) 6907–6923]. *J. Comput. Phys.*, 283: 609–610, 2015. doi:10.1016/j.jcp.2014.11.013.

C. Traxinger, H. Müller, M. Pfitzner, S. Baab, G. Lamanna, B. Weigand, J. Matheis, C. Stemmer, N. A. Adams, and S. Hickel. Experimental and numerical investigation of phase separation due to multi-component mixing at high-pressure conditions. In *ILASS - Europe 2017, 28th Conference on Liquid Atomization and Spray Systems*, 2017. URL `http://dx.doi.org/10.4995/ILASS2017.2017.4756`.

A. Urbano, L. Selle, G. Staffelbach, B. Cuenot, T. Schmitt, S. Ducruix, and S. Candel. Exploration of combustion instability triggering using Large Eddy Simulation of a multiple injector liquid rocket engine. *Combust. Flame*, 169:129–140, 2016. doi:10.1016/j.combustflame.2016.03.020.

G. D. van Albada, B. van Leer, and W. W. Roberts Jr. A comparative study of computational methods in cosmic gas dynamics. *Astron. Astrophys.*, 108:76–84, 1982. doi:10.1007/978-3-642-60543-7_6.

S. B. Verma and M. Chidambaranathan. Transition control of Mach to regular reflection induced interaction using an array of micro ramp vane-type vortex generators. *Phys. Fluids*, 27(10):107102, 2015. doi:10.1063/1.4932405.

X. Wang and V. Yang. Supercritical mixing and combustion of liquid-oxygen/kerosene bi-swirl injectors. *Journal of Propulsion and Power (Article in Advance)*, 2016. doi:10.2514/1.B36262.

A. Wehrfritz, V. Vuorinen, O. Kaario, and M. Larmi. Large eddy simulation of high-velocity fuel sprays: studying mesh resolution and breakup model effects for Spray A. *Atomization Sprays*, 23(5):419–442, 2013. doi:10.1615/AtomizSpr.2013007342.

R. D. Woodward and D. G. Talley. Raman imaging of transcritical cryogenic propellants . In *AIAA 34th Aerospace Sciences Meeting and Exhibit, Reno, NV*, 1996. doi:10.2514/6.1996-468.

Q. Xue, S. Som, P. K. Senecal, and E. Pomraning. Large eddy simulation of fuel-spray under non-reacting IC engine conditions. *Atomization Sprays*, 23(10): 925–955, 2013. doi:10.1615/AtomizSpr.2013008320.

V. Yang. Modeling of supercritical vaporization, mixing, and combustion processes in liquid-fueled propulsion systems. *P. Combust. Inst.*, 28(1):925–942, 2000. doi:10.1016/S0082-0784(00)80299-4.

N. Zong and V. Yang. Near-field flow and flame dynamics of LOX/methane shear-coaxial injector under supercritical conditions. *P. Combust. Inst.*, 31(2):2309–2317, 2007. doi:10.1016/j.proci.2006.08.106.

N. Zong, H. Meng, S.-Y. Hsieh, and V. Yang. A numerical study of cryogenic fluid injection and mixing under supercritical conditions. *Phys. Fluids*, 16(12), 2004. doi:10.1063/1.1795011.